Benjamin Wolfgruber, BSc

INVESTIGATIONS ON EMBRITTLEMENT OF AUSTENITIC STEELS BY LIQUID ZINC

MASTER'S THESIS

to achieve the university degree of

Diplom-Ingenieurin

Master's degree programme: Mechanical Engineering and Business Economics

submitted to

Graz University of Technology

Supervisor

Univ.-Prof. Dipl.-Ing. Dr.techn. Christof Sommitsch

Institute of Materials Science and Welding

Dr. Master Coline Béal

Graz, December 2016

AFFIDAVIT

I declare that I have authored this thesis independently, that I have not used other than the declared sources/resources, and that I have explicitly indicated all material which has been quoted either literally or by content from the sources used. The text document uploaded to TUGRAZonline is identical to the present master‘s thesis dissertation.

Date

Signature

Abstract

Austenitic stainless steels among other fields of use are especially attractive for the automotive industry due to their good mechanical properties. High yield strength and excellent ductility combined with a high corrosion resistance are favourable for high safety of passengers and a long vehicle lifetime.
Though, under certain conditions they show a high sensitivity to liquid metal embrittlement by zinc. This occurs e. g. when welding austenitic stainless steel with galvanised steel.

In this framework, the cracking behaviour of one type of austenitic stainless steel in contact with liquid zinc was characterised. This was achieved by carrying out thermo-mechanical tests with a Gleeble® 3800 simulator.

The embrittlement occurs in a limited temperature range which is dependent on other experimental parameters. Additionally, the influence of different parameters such as strain rate, time of contact between steel and liquid zinc, and amount of liquid zinc was characterised with the aim of getting a better understanding of the LME mechanism.

Kurzzusammenfassung

Rostfreie austenitische Edelstähle erfreuen sich aufgrund ihrer guten mechanischen Eigenschaften unter anderem auch im Automobilsektor großer Beliebtheit. Zu diesen Eigenschaften zählen die hohe Streckgrenze, die gute Duktilität und die sehr gute Korrosionsbeständigkeit, welche zu einer hohen Insassensicherheit und zu einer langen Fahrzeuglebensdauer beitragen.
Unter bestimmten Bedingungen jedoch, wie zum Beispiel beim Widerstandpunktschweißen mit verzinkten Stählen, zeigen austenitische Edelstähle eine Anfälligkeit auf das Phänomen „Liquid Metal Embrittlement“.

In dieser Arbeit wurde das Rissverhalten von einem austenitischen Edelstahl im Kontakt mit flüssigem Zink bestimmt. Dies wurde durch thermo-mechanische Versuche mittels eines Gleeble® 3800 Simulators durchgeführt.

Die Versprödung trat in einem bestimmten Temperaturbereich auf, welcher von anderen Parametern beeinflusst wird. Zusätzlich wurde der Einfluss einiger dieser Parameter, wie z. B. der Verformungsgeschwindigkeit, der Zeit des Kontaktes zwischen flüssigem Zink und Stahl sowie der Menge von flüssigem Zink untersucht, mit dem Ziel den Mechanismus von „Liquid Metal Embrittlement“ besser zu verstehen.

Index

Abstract i

Kurzzusammenfassung i

Index ii

Abbreviations v

List of figures vi

List of tables xi

1. Introduction 1

2. Literature review 3

2.1 Liquid Metal Embrittlement 3

2.1.1 General description of the phenomenon 3

2.1.2 Parameters of influence 4

2.1.3 Fracture type 10

2.1.4 LME of steel by zinc 13

2.1.5 Methods to test LME susceptibility 20

2.1.6 Methods to characterise LME incidents 21

2.2 Stainless steels 22

2.2.1 Austenitic stainless steels 22

2.2.2 Austenitic steel grade 301M – X10CrNi18-8 27

2.3 Overview of zinc coatings 29

3. Experimental procedures 32

3.1 Specimen 32

3.2 Coating 32

3.2.1 Painting 33

3.2.2 Electro-galvanising 34

3.3 Thermo-mechanical tests 35

3.3.1 Principle 35

3.3.2 Specimen preparation 37

3.4 Thermo-mechanical cycles 40
3.4.1 Tensile test 40
3.4.2 Hot tensile test 40
3.4.3 Interrupted test 41
3.4.4 Hot tensile test with pre-exposure time 41
3.4.5 Towards resistance spot welding simulation 41
3.5 Quantification of embrittlement 42
3.6 Microscopy investigations 42
3.6.1 Metallography 42
3.6.2 Light Optical Microscopy (LOM) 43
3.6.3 Stereo Microscopy 43
3.6.4 Scanning Electron Microscopy (SEM) 43
3.6.5 Energy-dispersive X-ray spectroscopy (EDX) 44
3.6.6 Electron backscatter diffraction (EBSD) 44
4. Results and discussion 45
4.1 Tensile behaviour of 301M 45
4.1.1 Room temperature behaviour 45
4.1.2 High temperature behaviour 46
4.2 Sensitivity of 301M steel to embrittlement by liquid zinc 47
4.3 Results of thermo-mechanical tests 48
4.3.1 Influence of temperature 49
4.3.2 Influence of strain rate 52
4.3.3 Influence of time of contact between base material and liquid metal 53
4.3.4 Influence of coating method 55
4.3.5 Influence of available amount of liquid metal 56
4.3.6 Interrupted tests 57
4.3.7 Approximation of resistance spot welding 58
4.4 Towards an explanation for mechanical behaviour 59
4.4.1 SEM investigation of fracture surfaces 59

4.4.2 Investigation of longitudinal section / quantitative LOM data 62
4.4.3 LOM investigation of RSW simulation test samples 67
4.4.4 SEM investigation of zinc layer after testing 68
4.4.5 SEM investigation of cracks 72
4.4.6 Summary 78
5. Conclusions 79
Outlook 81
References 82

Abbreviations

Abbreviation	Term
AISI	American Iron and Steel Institute
bcc	Body-centred cubic
EBSD	Electron backscatter diffraction
EDX	Energy-dispersive X-ray spectroscopy
EG	Electro-galvanised
EPMA	Electron probe microanalyser
fcc	Face-centred cubic
FEG	Field emission gun
IG	Intergranular
IWS	Institut für Werkstoffkunde und Schweisstechnik
LME	Liquid metal embrittlement
PHS	Press-hardened steel
RSW	Resistance spot welding
SE	Secondary electron
SEM	Scanning electron microscope
TEM	Transmission electron microscope
TG	Transgranular
TWIP	Twinning induced plasticity
UTS	Ultimate tensile strength
Wt.	Weight
Zn	Zinc
ZP	Zinc painted

List of figures

Figure 1: Cross section of a resistance sport weld spot of different steel sheets with occurrence of LME-induced cracks b) higher magnification of highlighted area in a) [1] 1

Figure 2: Stress-elongation curves of S355 grade steel in different environments at 350°C, 5 mm/min – modified from [7] 4

Figure 3: Relative reduction of energy over temperature represents the “ductility trough” for Fe–22Mn–0.6C steel in liquid zinc with a strain rate of $1.3x10^{-1}s^{-1}$ [3] 6

Figure 4: Influence of different strain rates on “ductility trough” of Fe–22Mn–0.6C steel in liquid zinc [31] 8

Figure 5: a)Thermo-mechanical cycle for applying pre-exposure time during a hot tensile test [3] b) Engineering stress-strain curves of Zn-coated Fe–22Mn–0.6C steel deformed with $1.3x10^{-1}s^{-1}$ at 800°C after holding at the same temperature for 10 and 20 seconds [31]. 9

Figure 6: Engineering stress-strain curves of Zn-coated 22MnB5 steel deformed at 850°C with 0.5 s^{-1} after holding at the same temperature for 4, 6, 8 and 20 min [32]. 9

Figure 7:Ductile transgranular fracture surface of steel 91 tested in liquid lead at 260°C [28] 10

Figure 8: Brittle intergranular fracture surface of cadmium plated steel screws [15] 11

Figure 9: Transition zone of intergranular (IG) and transgranular (TG) fracture zone of T91 steel in lead-bismuth eutectic [14] 11

Figure 10: EPMA investigation of zinc distribution of a LME crack formed on Zn-coated TWIP steel during tensile testing/ adapted from [4] 12

Figure 11: Thermal cycle used to test for the sensitivity to LME of Zn-coated TWIP steel 13

Figure 12: a) Engineering stress-strain curves of uncoated TWIP steel and Zn-coated TWIP steel. b) Zn-coated TWIP steel after the tensile test at 850°C [6]. 14

Figure 13: Interrupted tensile test on zinc coated austenitic steel [3] 15

Figure 14: SEM micrographs of the different fracture surface zones [3] (a): Overview of the fracture surface of (b) dimpled surface after room temperature deformation, (c) surface in contact with liquid zinc and (d) interface between the two previous zones 16

Figure 15: Possible scenario of liquid zinc penetration and crack propagation [31] 16

Figure 16: Micrograph of a LME crack formed on Zn-coated 22MnB5 PHS [5]: a) SEM image b) FE-EPMA of Zn distribution c) EBSD phase map for the bcc phase 17

Figure 17: Schematic illustration, revealing the mechanism of Zn grain boundary diffusion-weakening phase transformation leading to crack formation on Zn-coated PHS during die quenching. γ: austenite, α': martensite. (a) High-temperature crack initiation at a α-Fe(Zn) grain boundary in the surface alloy layer. (b) Zn diffusion along the γ grain boundary and transformation of the Zn-diffused γ grain boundary region to α-Fe(Zn). (c) Crack propagation through the weak α-Fe(Zn) grain boundary layer. (d) Crack propagation by repetition of the diffusion-transformation stages (b) and (c). (e) After cooling, the high-temperature Zn_{liq} distribution is reflected in the room-temperature distribution of Γ-Fe_3Zn_{10}. The absence of transformation of Γ to α' lath martensite allows for the identification of the Zn diffusion layer in the vicinity of the crack tip. [5] 18

Figure 18: a) Iron – zinc binary phase diagram [42] b) zinc rich region of the iron – zinc binary phase diagram [12] 19

Figure 19: a) Microstructure of 316L steel after hot rolling, cold reducing 30% thickness and solution annealing and etching with Berasha´s BII reagent [49] b) Grain structure of 316L steel after solution annealing and etching with a waterless Kailing´s tint etch [50] 23

Figure 20: The chromium content trend close to the grain boundaries of a stainless steel [54] 26

Figure 21: Time-temperature-sensitization curves for type 304 stainless steel in a mixture of $CuSO_4$ and H_2SO_4 containing free copper [51]. 27

Figure 22: Microstructure of deformed austenite [55] 28

Figure 23: Work hardening point of 301M grade steel [55] 29

Figure 24: Microstructure of different zinc coatings [57] 30

Figure 25:Specifications of different zinc coatings [56] 31

Figure 26: Production procedure of 301M steel sheets of 1.2mm thickness [1] 32

Figure 27: Shape and dimensions of tensile specimen 32

Figure 28: Sample of 301M material with zinc-rich painting 33

Figure 29: SEM micrograph of a layer of zinc-enriched painting on 301M steel 33

Figure 30: Electro-galvanising: a) Principle of electro-galvanising / adapted from [59] b) Setup for electro-galvanising in the laboratory of the IWS 34

Figure 31 a) Linear growth of zinc coating on 301M by electro-galvanising b) SEM image of electro-galvanised coating on base material 35

Figure 32: Gleeble 3800 simulator: a) Scheme [3] b) Image of the Gleeble® simulator at TU Graz 36

Figure 33: Chamber of Gleeble® 3800 simulator: a) empty chamber b) detail of chamber loaded with specimen and prepared for testing 37

Figure 34: a) Tensile specimen with welded central thermocouple and marks for further thermocouples b) Thermocouple welder by DSI 38

Figure 35: Temperature profile of tensile specimen at: a) 600°C b) 1100°C 39

Figure 36: Illustration of 3 different temperatures zones within a ruptured samples 39

Figure 37: Thermo-mechanical cycle at 800°C 40

Figure 38: Thermo-mechanical cycle for hot tensile tests with pre exposure time 41

Figure 39: Light optical image of cracks induced by LME 43

Figure 40: Engineering stress-strain curves of 301M obtained at room temperature with a strain rate of 1 mm/s 45

Figure 41: True stress-strain curves of 301M obtained at room temperature with a strain rate of 1 mm/s 46

Figure 42: Force-Stroke diagram of 301 steel at different temperatures: a) with 1 mm/s strain rate b) with 100 mm/s strain rate 47

Figure 43 a) Force-Stroke diagram of bare and zinc-painted 301M steel tensile tested at 800°C with 1 mm/s train rate b) macroscopic image of bare and zinc painted samples 48

Figure 44: Hot tensile test of ZP and bare samples tested at 800°C and 1 mm/s strain rate illustrating the moderate reproducibility 49

Figure 45: Force-Stroke curves of 301M steel samples coated with zinc-rich paint with 1 mm/s strain rate at: a) 600°C b) 700°C c) 800°C d) 900°C e) 1000°C f) 1100°C 50

Figure 46: Fracture energy reduction in respect to testing temperature for 301M coated with zinc-rich paint for 1 mm/s strain rate 51

Figure 47: a) Reminder of different temperature zones within the sample b) Zones of fracture for zinc-painted 301M steel samples tested at different temperatures with 1 mm/s strain rate 52

Figure 48: Force-Stroke curves of 301M steel coated with zinc-rich paint at 800°C: a) with 1 mm/s strain rate b) with 100 mm/s strain rate 52

Figure 49: Fracture energy reduction in respect to testing temperature for 301M coated with zinc-rich paint for 1, 16 and 100 mm/s strain rate. Data for 16 mm/s strain rate from literature [1] 53

Figure 50: Force-Stroke curves of 301M steel coated with zinc-rich paint at 800°C for different holding times: a) with 1 mm/s strain rate b) with 100 mm/s strain rate 54

Figure 51: Fracture energy reduction of 301M coated with zinc-rich paint at 800°C for 1 mm/s and 100 mm/s strain rate.....55

Figure 52: Influence of coating method on LME: a) Force-Stroke curves of samples tested with different coatings at 800°C with 100 mm/s strain rate b) Reduction of fracture energy of samples shown in a).....55

Figure 53: Force-Stroke curves obtained at 800°C with 100 mm/s strain rate and different holding times: a) of samples electro-galvanised with 2.5 µm of pure zinc b) of samples electro-galvanised with 10 µm of pure zinc 56

Figure 54: Fracture energy reduction of 301M at 800°C for 100 mm/s strain rate for samples coated with different coating thickness.....57

Figure 55: a) Interrupted tests with ZP samples at 800°C and 100 mm/s strain rate b) room temperature tensile test with pre-strained samples.....58

Figure 56: a) Force, stroke, temperature as a function of time displayed for a bare sample with a target temperature of 700°C b) Force-Stroke curves of RSW tests with 3 kN pre-tension and 80°C/s heating rate.....59

Figure 57: Fracture surface of 301M steel tensile tested at 800°C with 1 mm/s strain rate: a) Overview of fracture surface with rectangle showing the magnified area of b): higher magnification of fracture surface revealing dimples all over the area 60

Figure 58: Fracture surface of 301M steel coated with zinc-rich paint and tensile tested at 800°C with 1 mm/s strain rate: Overview of fracture surface with rectangle showing the magnified area of b): borderline of two different fracture zones with rectangle 1 showing the brittle fracture mode displayed in c) and rectangle 2 showing dimples of the ductile fracture mode displayed in d) 61

Figure 59: Fracture surface of ZP sample tensile tested at 800°C with 100 mm/s strain rate: a) whole fracture surface b) magnified area with visible borderline between ductile and brittle part 62

Figure 60: SEM image of longitudinal section of ZP sample tested at 800°C with 1 mm/s strain rate: a) without holding time b) after 40 s holding time.....63

Figure 61: Summary of light microscopy data of hot tensile test of zinc-coated 301M steel at different temperatures with 1 mm/s strain rate: a) Number of cracks b) Total length of cracks c) Average depth of cracks d) Maximum depth of cracks 64

Figure 62: Histogram of crack lengths at tested at: a) 600°C b) 700°C c) 800°C d) 900°C e) 1000°C f) 1100°C 65

Figure 63: Summary of light microscopy data of hot tensile test of zinc-coated 301M steel at 800°C with 1 mm/s strain rate: a) Number of cracks b) Total depth of cracks c) Average depth of cracks d) Maximum depth of cracks 66

Figure 64: Stereo microscopy images of samples after RSW simulation test procedure at: a) 700°C b) 800°C c) 900°C 68

Figure 65: a) Coating layer of zinc painted sample tensile tested at 800°C with 1 mm/s strain rate b) Coating layer of zinc painted sample tensile tested at 800°C after 40 s pre-exposure time with 1mm/s strain rate 69

Figure 66: SEM image of zinc contaminated boarder area after tensile testing a zinc-painted sample at 800°C after 40 s holding time with 1 mm/s strain rate: a) overview b) higher magnification of area framed in a) showing the location of EDX point measurements 70

Figure 67: Coating layer of 10 µm electro-galvanised sample tensile tested at 800°C after 20 s holding time 71

Figure 68: SEM image and EDX mapping of crack on zinc painted sample tested at 800°C: a) SEM image b) Fe-Zn distribution c) Zn distribution d) Ni distribution 73

Figure 69: a) Image of deep crack in zinc painted sample showing the location of EDX line scans b) EDX line scan in 30 µm depth c) EDX line scan in 380 µm depth d) EDX line scan in 700 µm depth 74

Figure 70: EDX mapping of 2.5 µm electro-galvanised sample tested at 800°C 75

Figure 71: EDX line scan through crack within zinc-painted sample tested at 800°C 75

Figure 72: Filled crack of zinc-painted sample tested at 800°C showing the location of spot scans 76

Figure 73: Deep crack of an electro-galvanised sample tensile tested at 800°C with a strain rate of 100 mm/s: a) SEM image highlighting the area picked for EBSD measurement b) higher magnification SEM image with arrows pointing at different grains along the cracking path ... 76

Figure 74: EBSD image of LME induced deep crack: a) inverse pole figure (IPF) coloured map showing all detected grains b) IPF coloured map showing only ferritic grains 77

List of tables

Table 1: Intermetallic phases of iron and zinc [42] 19

Table 2: Chemical composition of 300 series steels [48] 24

Table 3: Mechanical properties of 300 series steels [52] 24

Table 4: Chemical composition of 301M [55] 27

Table 5: Mechanical properties of 301M [55] 29

Table 6: Results of EDX point measurements of zinc painted sample after tensile testing at 800°C 70

Table 7: Results of spot scans of electro-galvanised sample tested at 800°C after 20 s holding time 71

Table 8 Chemical composition of spot scans of zinc painted sample tested at 800°C 76

1. Introduction

Due to increasing environmental requirements, the fuel consumption and the emissions of cars have to be further reduced. One way of doing so is to decrease the weight of the vehicle without disadvantaging the safety for the passengers.

A key role in this development process is based on the use of new materials with higher strength and ductility, especially for the structural parts of the chassis. Austenitic stainless steels are promising for this purpose showing high mechanical properties while additionally bringing very high corrosions resistance, good weldability and formability.

With the aim of keeping the production costs of a car possibly low, high strength austenitic steels are used together with other galvanised steels and among other techniques joined by resistance spot welding. A typical car chassis consists thousands of spot welds. During this welding process of galvanised steel sheets with austenitic steel, liquid zinc from the coating gets in contact with austenitic steel, leading to the phenomenon of Liquid Metal Embrittlement (LME).

Such case is reported by Alvarez [1] when investigating a resistance spot weld of 301M austenitic stainless steel, welded with two galvanised steel sheets. Thereby appearance of cracks in the austenitic steel inside the weld nugget was found which is displayed in Figure 1. Figure 1b) shows a higher magnification of the highlighted area of the weld cross section in a), revealing small cracks, highlighted with arrows.

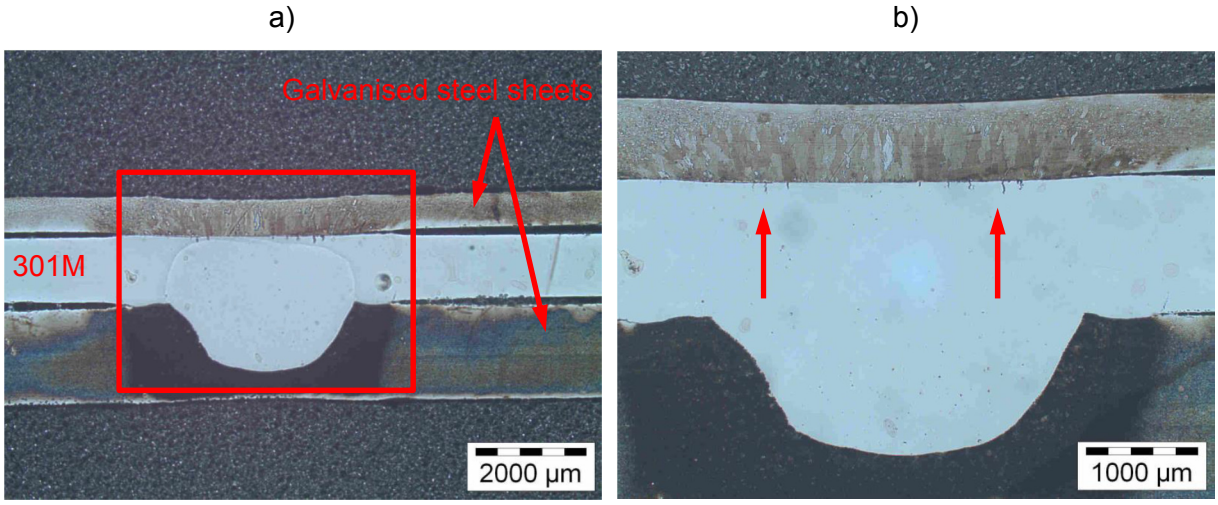

Figure 1: Cross section of a resistance sport weld spot of different steel sheets with occurrence of LME-induced cracks b) higher magnification of highlighted area in a) [1]

LME results from the simultaneous presence of liquid metal and internal or external stresses. In a limited temperature range (designated the temperature ductility trough) it leads to a deterioration of mechanical properties of the steel.

Here, the focus of this work is set. The aim was to determine the conditions where LME occurs

and study the influence of different parameters on the embrittlement process of 301M austenitic stainless steel by liquid zinc.
Another aim was to deepen the understanding of the mechanisms involved in this phenomenon.

At first, a review of current literature is given, followed by an explanation of the experimental procedure that was carried out during this work. Afterwards the results are presented and discussed and finally some conclusions are drawn.

2. Literature review

This section gives an overview of literature found during this work, starting with a description of LME, continuing with a review of the austenitic steels and closing with information about different zinc coating techniques.

2.1 Liquid Metal Embrittlement

Liquid Metal Embrittlement is a failure mechanism that is of practical importance due to its common occurrence and fatal consequences.

It describes the loss of ductility of a usually ductile solid material (embrittled metal) when exposed to a specific liquid metal (embrittling metal), which can appear during high temperature processes such as e.g. welding processes. In many cases, there is also a necessity of an external load or the presence of internal residual stresses reported [2]. In case of occurrence, the embrittled metal experiences a rapid crack formation which often leads to a total failure of the particular component [2], [3].

In case of a tensile test it results in a heavy reduction of strain to rupture and a brittle fracture mode of the embrittled solid metal.

Since its first mentioning in 1974 [4] many experiments have focused on LME, though there is not yet a complete understanding of the mechanisms behind it. Recent works are still focusing on a general model of predicting the LME occurrence and understanding the mechanisms behind it [5], [6].

2.1.1 General description of the phenomenon

LME occurs, when stresses and liquid embrittling metal appears at the same time. It drastically deteriorates the ductility while other mechanical properties such as young modulus and yield strength seem to be unaffected. When performing tensile tests in embrittling environment, a significant reduction of elongation and maximum stress are typical consequences of LME when compared to inert environment [2], [3].

Figure 2 reveals such behaviour as S355 steel experiences heavy embrittlement in contact with liquid Cd-5%Zn.

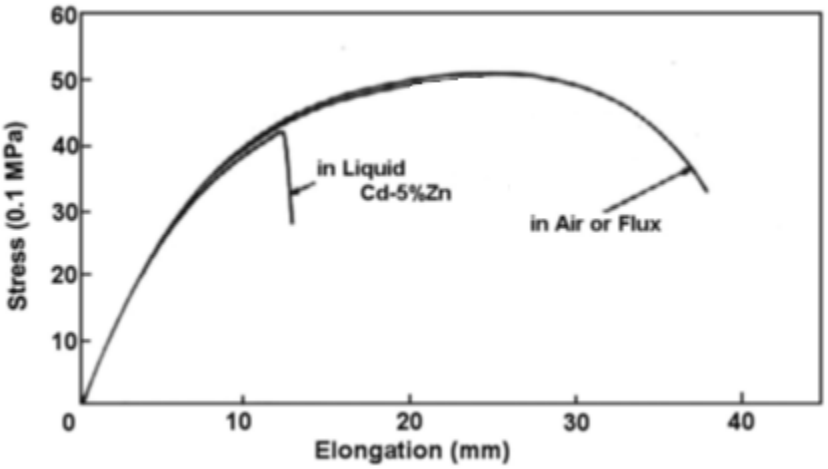

Figure 2: Stress-elongation curves of S355 grade steel in different environments at 350°C, 5 mm/min – modified from [7]

2.1.2 Parameters of influence

Parameters of influence have been observed in various studies. Below, some of the factors reported in the literature are listed and described.

It can be seen as general statement that the occurrence and the impact of LME strongly depend on testing conditions and procedures employed [8], [9].

Metals combination

Molten embrittling metal is often reported as a basic requirement for LME occurrence. It is noted to be the driving force behind this mechanism and it dictates how far the embrittlement process continues [8], [10], [11].

The material combination sets the general conditions for the embrittlement. Exchanging one of the involved materials will most likely lead to very different results and possibly change every parameter involved such as mutual solubility, wettability, formation of intermetallic compounds and others. Low mutual solubility between solid and liquid metal was considered as a basic condition for embrittlement to take place [1]. Contradictorily, in the present case of the Fe and Zn system, a large mutual solubility in comparison to many other systems is found but still strong effects of LME [12].

Also an intimate contact and a good wettability between both metals is commonly mentioned as requirement [2], [13]–[15]. If the contact is hindered by the means of an oxide layer or removal of the liquid metal after preliminary contact, the LME process does not take place [2].

LME was found in many material combinations, such as:

- Al_{solid} – Ga_{liquid} System [16]–[18]
- Al_{solid} – Hg_{liquid} System [13], [19]
- Ni_{solid} – Bi_{liquid} System [20], [21]
- Cu_{solid} – Bi_{liquid} System [22]
- Steel $_{solid}$ – Zn $_{liquid}$ [3], [6], [8], [12]

Rouholah Ashiri et al [8] found that the susceptibility of TWIP steels to embrittlement by liquid zinc is influenced by the chemical composition of the coating material and by the coating process itself. In their experiments they carried out resistant spot welding on TWIP steels, which were prepared with different coatings. Their results revealed that the lower melting point of the coating of galvanised samples supplies the liquid embrittling metal earlier and makes it more susceptible to LME than galvannealed samples.

Temperature

The temperature requirement that comes with LME is described by many authors.
Joseph [2] reports about a ductility trough, discovered by Rozhanskii et al. [23], which determines the temperature zone where the strength und ductility of the material is reduced by the presence of liquid metal; the lower end of it usually being close to the melting point of the embrittling metal.

However, Glasbrenner et al [24] experienced a different LME starting point for their investigated MANET II steel in eutectic Pb-Bi environment. With 125°C as melting point of the embrittling material, the embrittlement starts only at 250°C. Also Beal [25] found that the embrittlement of TWIP steel by liquid zinc starts at temperatures higher than 600°C while melting point of zinc being at 419°C.
After reaching the lower limit of the temperature range the severity of embrittlement increases until its maximum is reached and then starts a recovery until reaching an upper limit where LME does not occur anymore.

Beal [3] stated an explanation where the upper end of the ductility trough is reached due to vaporization of the embrittling metal. In the Fe – Zn system, Beal found the upper end being at roughly 1000°C with a zinc boiling point of 907°C.
This explanation has been confirmed with the results of Frappier [12] when measuring the remaining zinc content on different steels by EDX after high temperature exposure. The result was a decreasing amount of zinc on the surface of the steels with increasing temperature.

Figure 3 illustrates the reduction of fracture energy as an indicator for the severity of LME in respect to the testing temperature of a Fe–22Mn–0.6C steel coated with zinc. This shape of

curve is known in literature as the ductility trough of LME incidents. In between the lower and the upper temperature limits, the ductility is progressively reduced until it reaches its minimum and afterwards starts a recovery until no more embrittlement occurs at the upper end of the trough [3].

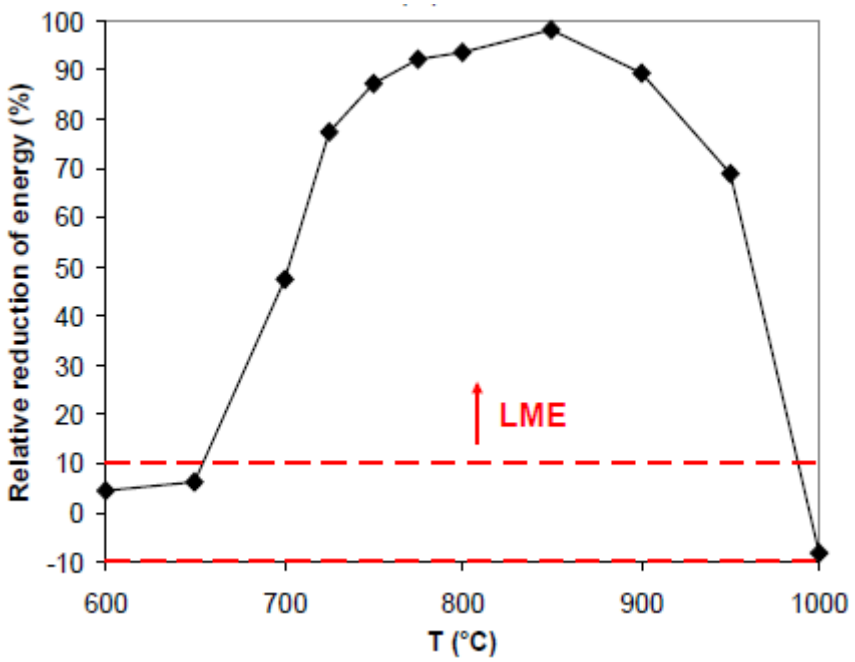

Figure 3: Relative reduction of energy over temperature represents the "ductility trough" for Fe–22Mn–0.6C steel in liquid zinc with a strain rate of 1.3x10^{-1}s^{-1} [3]

Microstructure of solid metal

Fernandes et al found [26], when testing two brass alloys with different microstructures in molten gallium, that CZ106 α-brass is unsusceptible of LME while CZ109 β-brass exhibits embrittlement. This behaviour is explained by the dependence of stresses generated at the dislocation pile-ups on the type of slip behaviour.

It is reported that harder materials usually experience stronger embrittlement, due to very high yield strength leading to local stress concentrations which favour the LME occurrence [2], [27], [28].

Also the grain size follows a trend towards higher grain size increasing the embrittlement [3] [26]. This influence is shown in two different effects. Firstly, the elongation to rupture and the fracture stress are drastically reduced and secondly, the ductility recovery temperature is considerably increased [26], [29]. No explanation is stated for the causes of these effects.

As a result of those trends, the embrittling process seems to be affected by heat treatments, welding and other processes that change the microstructure of the solid metal. It can be concluded that even materials that are not sensitive to LME can become sensitive after such treatment.
The 8-9% Cr martensitic steels investigated by Sample and Kolbe [30] proved to be unsusceptible to LME by liquid Pb-17Li in tempered fully martensitic state, but became sensitive after a welding process was simulated.

In general it can be said that the more a structure favours stress concentration, the more it is sensitive to LME. Therefore bcc structures tend to be more sensitive than fcc structures [3].

Stress

By definition, applied tensile or residual stresses are a basic requirement for LME to occur [2]. Since this threshold stress can be very low, there are also LME incidents known without any measured stresses. Though, even a notch in the specimen can be sufficient to reach the minimum threshold stress and it is often questionable if this stress can even be measured [3].

One of the most known exceptions to this theory is the embrittlement of aluminium by gallium or copper by bismuth [2], which takes place without any measurable stresses.

Recently, Beal [31] introduced a criteria of predicting LME on austenitic steel which states that a critical stress needs to be reached to initiate LME.

Strain rate

The strain rate plays an important role in the results of LME tests. Figure 4 shows that the width of the above mentioned ductility trough, meaning the temperature range where embrittlement occurs, increases with higher strain rate [26].

Furthermore Beal [3] experienced when carrying out tensile tests of high manganese TWIP steel with liquid zinc, that LME only occurs when a minimum strain rate is reached (see black curve in Figure 4). It may be related to the comparably long time of contact between liquid metal and the steel before reaching the high stress level required for LME. This time plays an important role as further described by the influence of pre-exposure time. Beal also found that especially the lower end of the ductility trough strongly depends on the strain rate of the tensile tests. In Figure 4 one can see this lower end at approx. 775°C with a low strain rate of 1.3 x 10^{-2} s^{-1}, 700°C for 1.3 x 10^{-1} s^{-1} and 600°C for 1.3 s^{-1}. This shows a behaviour of increasing strain rate leading to lower embrittlement start temperatures.

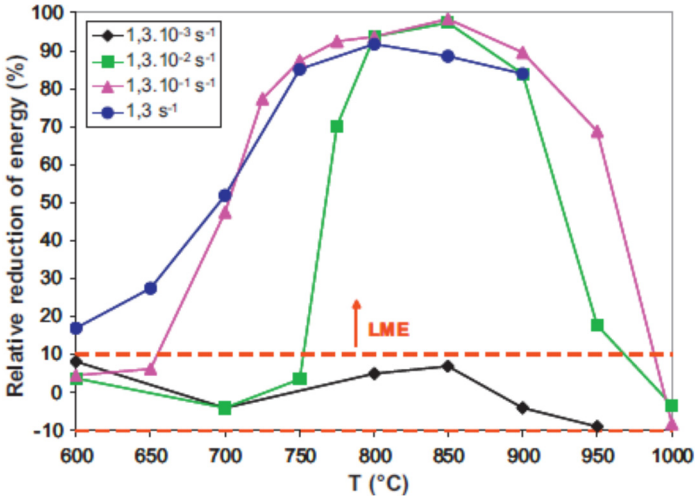

Figure 4: Influence of different strain rates on "ductility trough" of Fe–22Mn–0.6C steel in liquid zinc [31]

Pre-exposure time

Moreover, the influence of pre-exposure time was studied by some authors. This is the time when the sample is in contact with the embrittling metal without the application of force. Figure 5a shows a thermo-mechanical cycle with the pre-exposure labelled.

Beal [3] discovered, when applying different pre-exposure times after the zinc coated steel reached the target temperature of 800°C, a significant change of mechanical behaviour. The results, displayed in Figure 5b show in case of the Fe–22Mn–0.6C TWIP steel that the material experienced a complete recovery of ductility and strength after a sufficient holding time. Already with a pre-exposure time of 20 seconds the influence of the LME on the mechanical properties was fully eliminated.

This effect was addressed to the liquid zinc forming intermetallic compounds with the base material, which consumes more and more liquid zinc with increasing holding time. In conclusion, if the material has enough time to form those intermetallic compounds at high temperature before reaching the critical stress (e.g. due to pre-exposure time before tensile testing or due to a very low strain rate) LME does not occur.

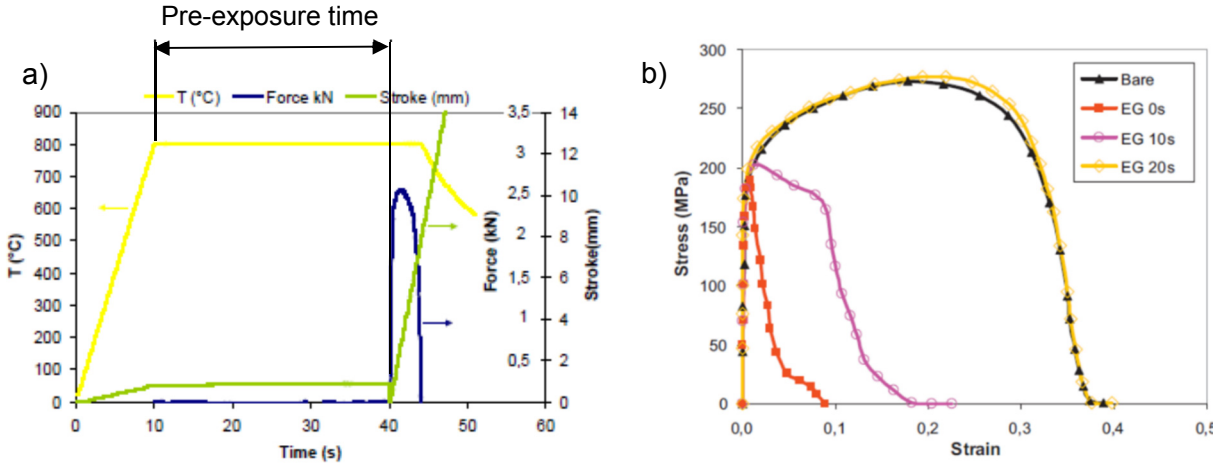

Figure 5: a)Thermo-mechanical cycle for applying pre-exposure time during a hot tensile test [3] **b) Engineering stress-strain curves of Zn-coated Fe–22Mn–0.6C steel deformed with 1.3x10^{-1}s^{-1} at 800°C after holding at the same temperature for 10 and 20 seconds** [31]**.**

Similar results were also found by Lee et al [32]. The investigated 22MnB5 steel was hot dip galvanised and tensile tested by means of a thermo-mechanical simulator. After using significantly longer holding times between 4 and 20 min it again resulted in a significant recovery of ductility which can be seen in Figure 6. With a pre-exposure time of 20 min the mechanical behaviour of the material is fully recovered.

The explanation stated is that when the tested 22MnB5 steel is covered by a solid solution of Zn in the α-Fe, which can be performed with an increased austenitisation time, the presence of liquid Zn can be fully suppressed by diffusion of Zn into the surface of the material. Only in the coating layer cracks were found after testing.

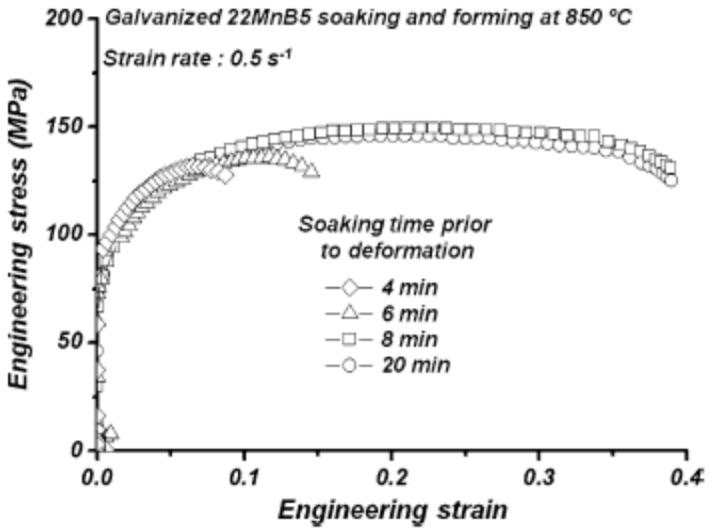

Figure 6: Engineering stress-strain curves of Zn-coated 22MnB5 steel deformed at 850°C with 0.5 s^{-1} after holding at the same temperature for 4, 6, 8 and 20 min [32]**.**

Some authors also mentioned that the time of contact between solid metal and liquid embrittling metal had no influence on the LME occurrence of the tested system. For example, systems as aluminium-mercury and zinc-copper alloy-mercury show no influence of time of exposure before testing, since the fracture stress remains unchanged after different pre-exposure times [33].
Others [24], [30] found that preliminary wetting during pre-exposure is a necessary requirement for embrittlement to occur.

2.1.3 Fracture type

LME is known for its very high crack propagation rate of up to several meters per second [2], [29]. It is often linked with intergranular fracture, since the grain boundary region is known to be heavily influenced by LME mechanisms [2].

In the literature different fracture types of LME tested samples can be found.

As illustrated in Figure 7, Legris et al [28] observed a dimpled area, typical for a ductile transgranular fracture surface after testing steel 91 in liquid lead.

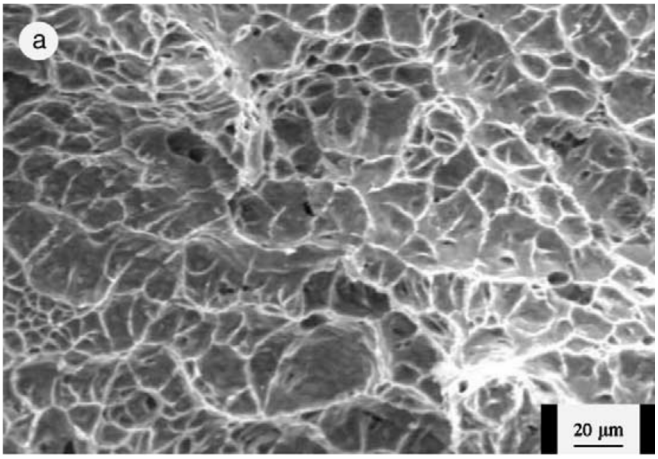

Figure 7:Ductile transgranular fracture surface of steel 91 tested in liquid lead at 260°C [28]

Brittle intergranular fracture was observed in many studies targeting LME [11], [26], [34]. Figure 8 shows this type of fracture surface of a steel screw plated with cadmium after the cadmium melted during a fire [15].

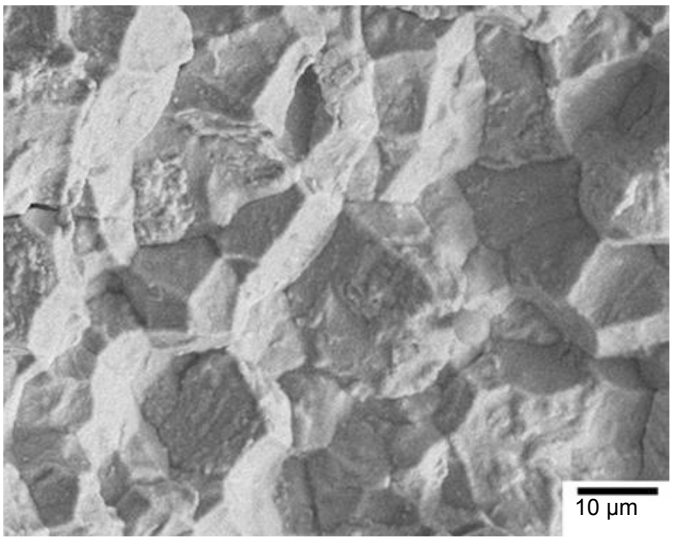

Figure 8: Brittle intergranular fracture surface of cadmium plated steel screws [15]

Mixed fracture surfaces consisting of ductile and brittle zones were found at MANET II steel in liquid Pb-Bi eutectic [24], T91 steel in Pb-Bi eutectic [14] and EUROFER97 in liquid Pb-Li environment [35].

Figure 9 shows the transition zone of a mixed fracture surface area of T91 steel embrittled in lead bismuth eutectic [14].

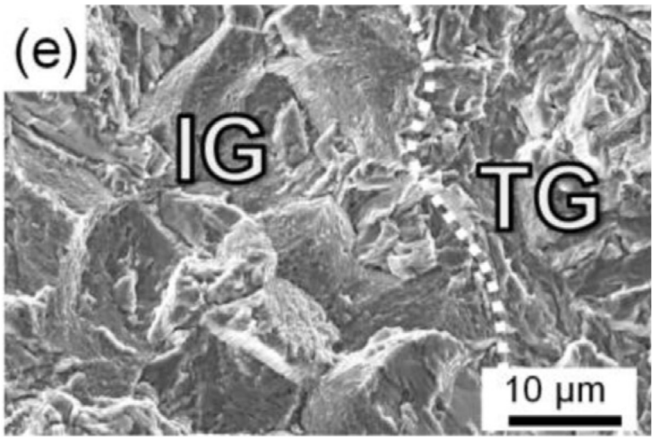

Figure 9: Transition zone of intergranular (IG) and transgranular (TG) fracture zone of T91 steel in lead-bismuth eutectic [14]

Fernandes and Jones [26] described the mixed fracture surface that occurred during their investigations on CZ109 brass tested in gallium by the limited amount of gallium that was applied to the surface of their specimen. For conditions defined by the ductility trough and when liquid gallium was available they found a brittle fracture. Due to the limited amount of gallium that

was applied to the surface of specimen before testing, Fernandes and Jones observed specimens in which the gallium depleted when the brittle cracks grew. In those cases, a transition from brittle fracture mode to ductile microvoid fracture, which is the expected fracture type for this material without LME influence, was found.

Glasbrenner et al [24] experienced similar results and stated that embrittlement only occurs when the crack tip of their MANET II steel is wetted by liquid Pb-Bi eutectic. This suggests that the presence of embrittling liquid metal at the tip of the crack is a basic condition for brittle cracks to grow.

Figure 10 shows the distribution of embrittling metal in a LME induced crack, observed in a zinc coated TWIP steel. The wide red layer in the upper part represents the zinc coating on the surface of the sample. Further into the material the crack shows a decreasing concentration of zinc getting close to zero at the tip of the crack.

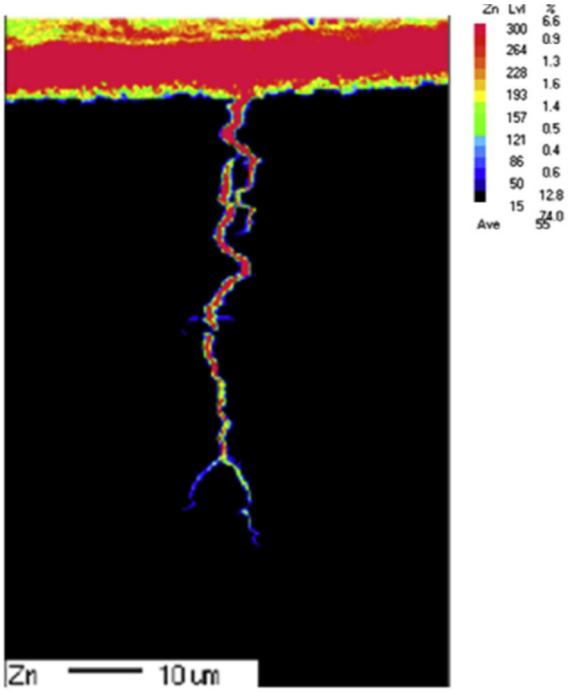

Figure 10: EPMA investigation of zinc distribution of a LME crack formed on Zn-coated TWIP steel during tensile testing/ adapted from [4]

When testing steel with liquid zinc the occurrence of a fracture surface completely covered with zinc is also mentioned by some authors [3]. An example is presented in Figure 14c).

2.1.4 LME of steel by zinc

Literature reports about many cases of steels being embrittled by a number of liquid metals [27], [34], [36], [37]. One could consider them as having a poor resistance to LME. Especially in nuclear applications many structural steels have been investigated while being in contact with liquid Pb, Bi, Pb-Bi or Pb-17Li [3].

This work focuses on LME of steel by liquid zinc, which is a common problem when welding galvanised steels. Different studies [11], [38]–[40] focused on this issue. LME of iron by zinc presents an exception to the empirical rule of LME due to the possibility of those elements to form intermetallic compounds. This is further discussed in chapter 2.1.4.1.

Bruscato [11] describes two different interactions between molten zinc and austenitic steel. Type I embrittlement occurs when molten zinc erodes unstressed 300 series steel at a temperature range between 419–570°C, penetrating grain boundaries relatively slowly.
Above 750°C type II embrittlement takes place in stainless steels when put under load and exposed to liquid zinc. This is described as the classical LME process.

Kang et al. [6] carried out tensile tests on Zn-coated TWIP steel with a thermo-mechanical cycle shown in Figure 11. The tests were performed after each of the samples was heated to a target temperature of 850°C with a heating rate of 10°C s^{-1}. After reaching this temperature the sample was isothermally held for 30 s and then strained to a value of 40% with a strain rate of 0.5 s^{-1}. Finally the sample was air cooled with a rate of -60°C s^{-1}. This procedure is displayed in Figure 11.

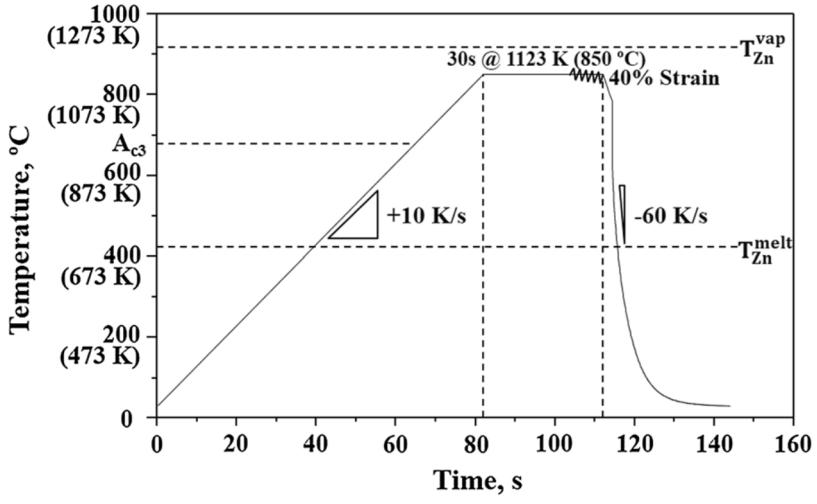

Figure 11: Thermal cycle used to test for the sensitivity to LME of Zn-coated TWIP steel

In Figure 12a) the results of these tests are illustrated. The two engineering stress-strain curves represent a typical case of LME on austenitic steel [6]. The tensile test results of the Zn-coated

sample is dominated by highly brittle behaviour, especially visible when compared to its uncoated reference sample.

The image in Figure 12b) of the fracture of the sample gives further confirmation about the embrittlement. Little signs of necking are visible which would occur on tensile tests of ductile materials and furthermore the macroscopic image reveals the presence of many cracks, typical for LME incidents.

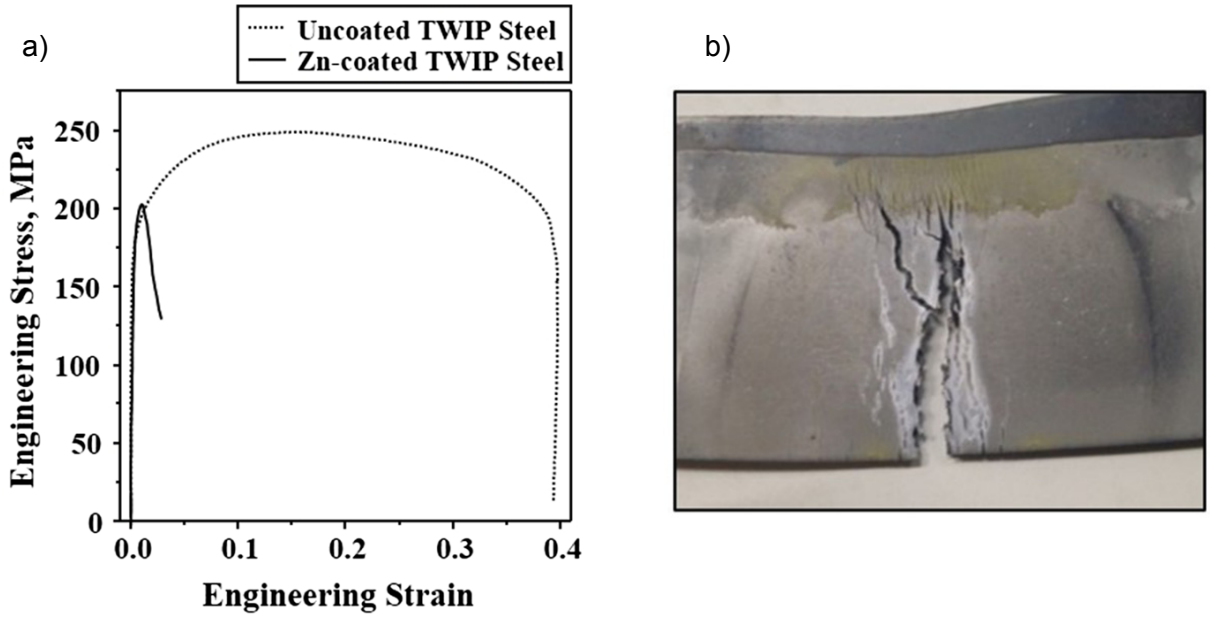

Figure 12: a) Engineering stress-strain curves of uncoated TWIP steel and Zn-coated TWIP steel. b) Zn-coated TWIP steel after the tensile test at 850°C [6]**.**

In 2012 Beal [31] came up with a possible scenario for the liquid zinc penetration and crack propagation after performing the below mentioned testing procedure:

Interrupted tests were carried out with zinc coated austenitic steel. The specimen was heated up in a thermo-mechanical simulator and put under constantly increasing tensile load. The experiment was stopped after crack initiation started, but before the specimen was fully fractured (see red cross in Figure 13).

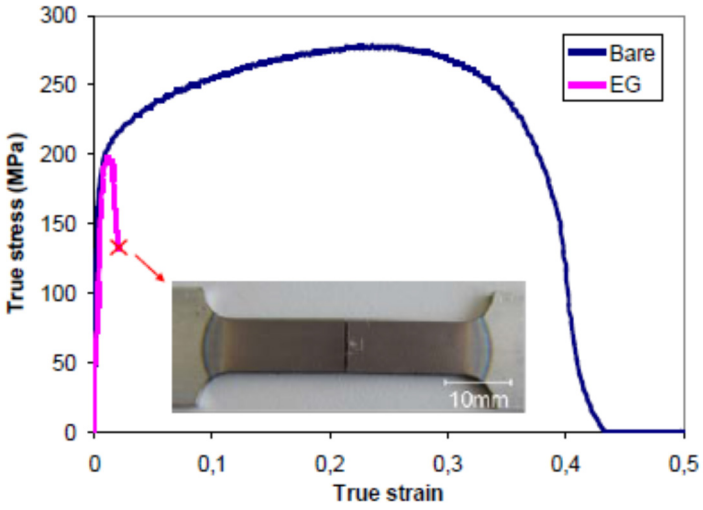

Figure 13: Interrupted tensile test on zinc coated austenitic steel [3]

Afterwards, when the sample was torn apart at room temperature two different types of fracture surfaces were found.

At first, a typical LME affected surface which was produced at 800°C and secondly, a surface typical for ductile failure produced at room temperature. The fracture surface of this test is shown in Figure 14: Picture a) shows an overview of the different zones within the fracture surface. In b) a dimpled surface is revealed, typical for ductile fracture. Image c) displays an area of the fracture surface fully covered by zinc while d) reveals the interface between the 2 different zones in the fracture surface

a) b)

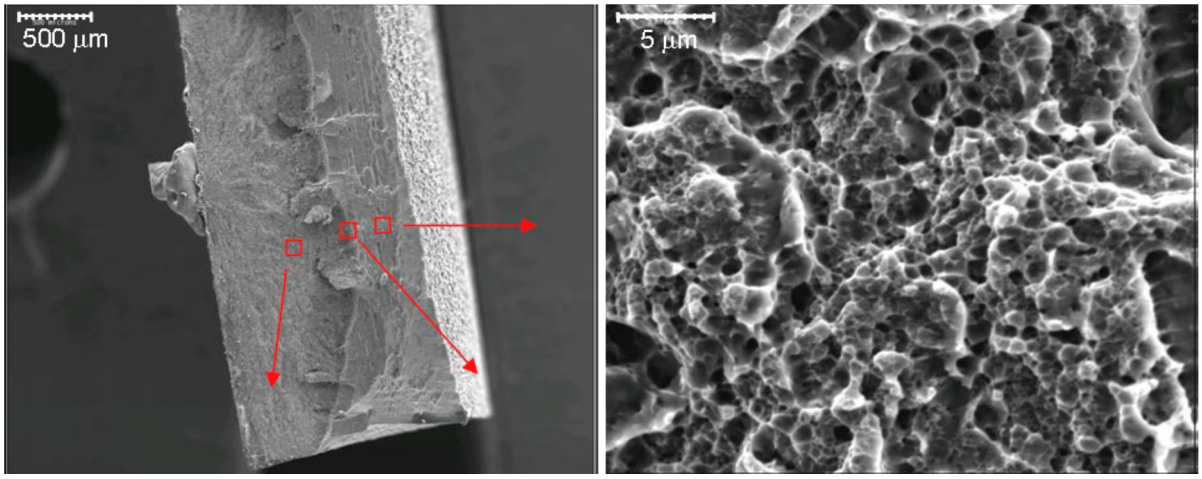

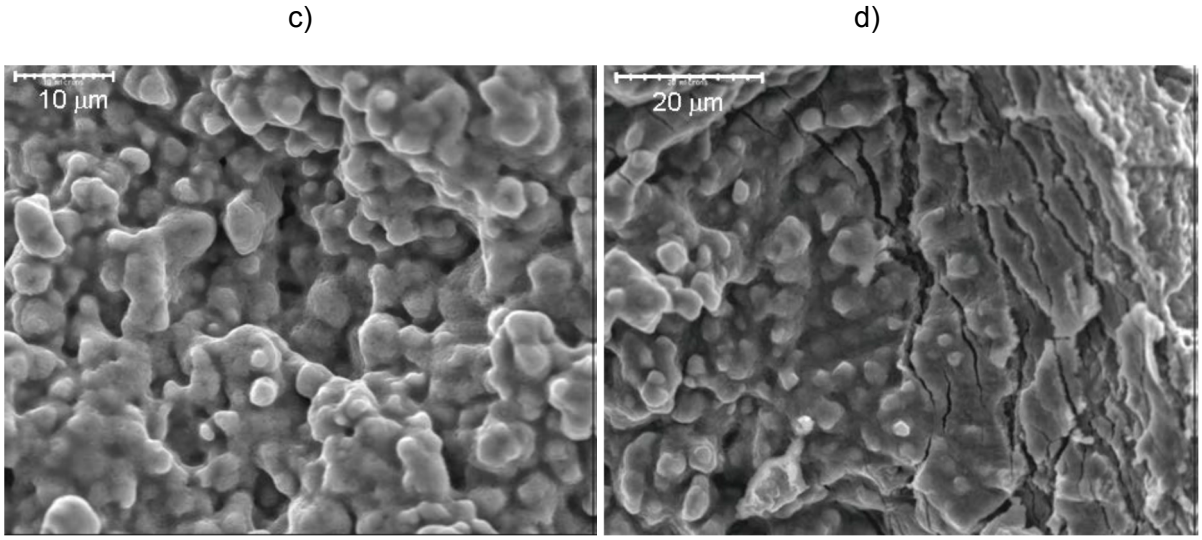

Figure 14: SEM micrographs of the different fracture surface zones [3] **(a): Overview of the fracture surface of (b) dimpled surface after room temperature deformation, (c) surface in contact with liquid zinc and (d) interface between the two previous zones**

A subsequent EDX analysis made clear that zinc was present on the whole brittle fracture surface produced at 800°C but could not be detected any further than in the cracked zone. Therefore Beal states, as illustrated in Figure 15

- At first, liquid zinc penetrates at grain boundaries along a certain distance due to high tensile stresses and good wettability (a)
- Crack opens along the zinc penetration path because of tensile stresses and is filled in with liquid zinc (b)
- Liquid zinc penetrates further than crack tip (c)
- Crack opens along zinc penetration path and so forth

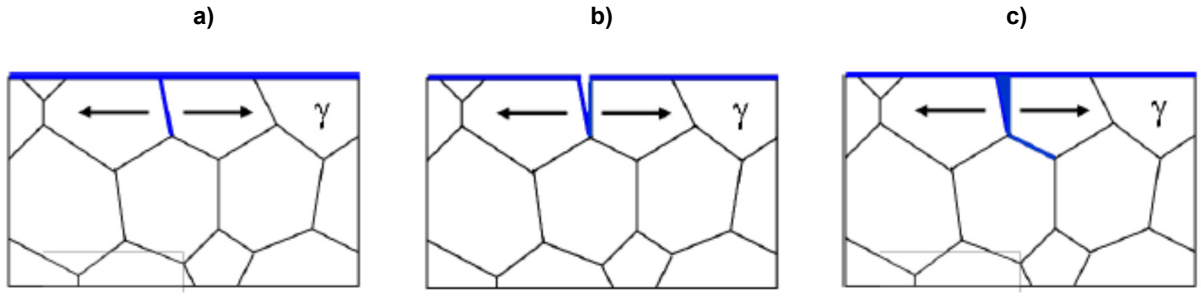

Figure 15: Possible scenario of liquid zinc penetration and crack propagation [31]

More recently, Cho et al [5] introduced a model for LME failure mechanism when experimenting with crack formation of Zn-coated Press hardened steel (PHS) while die quenching. The samples were heated in a Gleeble® thermo-mechanical simulator to 900°C in 30s, strained to 40% engineering strain and afterwards quenched to room temperature with -60°C s^{-1}. During

austenitisation the zinc coating reacted with the base material and formed a phase mixture of body-centred cubic (bcc) solid solution of Zn in α-Fe, designated α-Fe(Zn), and the Γ- Fe_3Zn_{10}.

Figure 16 reveals the microstructure of a LME crack formed on Zn-coated 22MnB5 press hardening steel. Figure 16a) displays that the crack initiated in the surface alloy layer and then propagated into the base material. The surface alloy layer had a thickness of approximately 15 µm and consisted mainly of coarse α-Fe(Zn) grains. Γ-Fe_3Zn_{10} was found in the intergranular region between those coarse α-Fe(Zn) grains.

In Figure 16b) the elemental distribution of zinc is displayed. In the central region of the crack and in the Γ-Fe_3Zn_{10} part of the surface alloy layer the Zn content was 70 – 80 wt.%.

Figure 16c) shows the EBSD phase map for the bcc phase. In the surface alloy layer the α-Fe(Zn) located on both sides of the Γ-Fe_3Zn_{10} (see white arrows in the picture) showing different orientation on either side and therefore suggesting that Zn_{liq} penetrated the grain boundaries of α-Fe(Zn) in the surface alloy layer. The α-Fe(Zn) grain boundaries in the surface alloy layer are the most favourable for the nucleation of cracks.
In the base material, the cracks also showed indications of the presence of liquid zinc at high temperature at α-Fe(Zn) grain boundaries rather than prior austenite grain boundaries. Zinc tends to stabilise ferritic structure and is insoluble in γ-Fe at 900°C (see chapter 2.1.4.1). The observation of α-Fe(Zn) grains around the cracks suggest that the grain boundary region was not austenitic before the quench which concludes that the austenitic grains that surround the cracks had to some extent transformed to α-Fe(Zn) grains. This was explained with the zinc grain boundary diffusion-mitigated phase transformation of the austenitic grain boundary in this region.

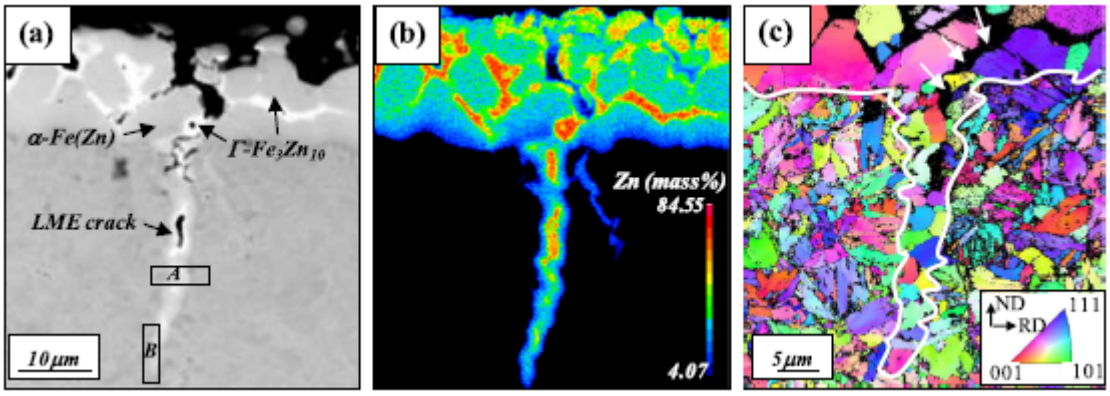

Figure 16: Micrograph of a LME crack formed on Zn-coated 22MnB5 PHS [5]**: a) SEM image b) FE-EPMA of Zn distribution c) EBSD phase map for the bcc phase**

The results of Cho et al lead to the following schema:

a) At high temperature, a deformation easily initiates cracks at α-Fe(Zn) grain boundaries in the surface alloy due to the much lower strength in comparison to the austenite phase of the matrix.
b) The austenitic grain boundaries serve as Zn diffusion paths. Since zinc is a strong ferrite stabiliser the boundary region of the Zn paths transforms to α-Fe(Zn). Due to the higher substitutional solute diffusivity in ferrite compared to the austenite, this further increases the Zn grain boundary diffusion.
c) Cracking along grain boundaries of the diffusion transformed region, where the low strength α-Fe(Zn) replaced the austenite grain boundary region.
d) After the crack has formed, the Zn_{liq} progresses due to capillarity, again transforming the grain boundary at the crack tip to α-Fe(Zn). This leads to crack propagation once the grain boundary is weakened and unable to withstand the applied stresses, being magnified locally at the crack tip. Through repetition of the stages (b) and (c) the crack propagates further.
e) During quenching, the Fe saturated Zn_{liq} transforms to Γ-Fe_3Zn_{10} which makes it possible to map accurately the distribution of the liquid in the matrix. The matrix, consisting of austenite, transforms to martensite but the α-Fe(Zn) in the surrounding area of the crack remains unchanged.

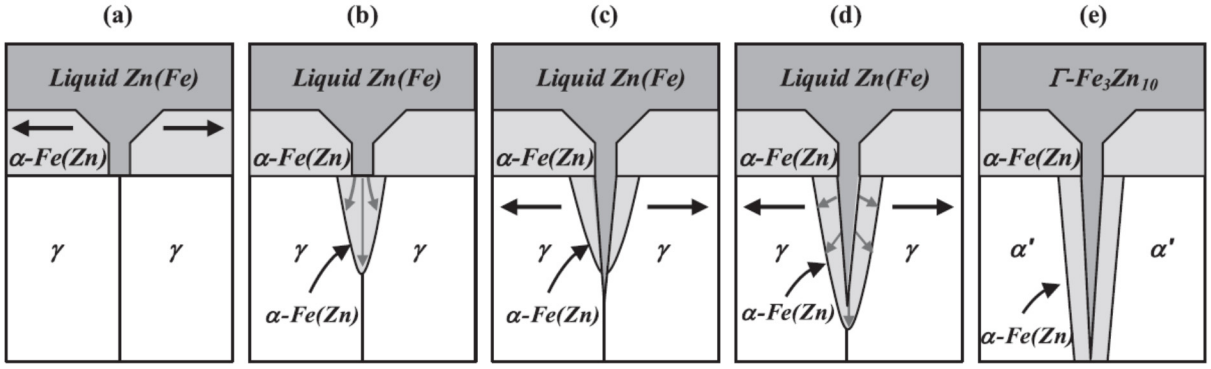

Figure 17: Schematic illustration, revealing the mechanism of Zn grain boundary diffusion-weakening phase transformation leading to crack formation on Zn-coated PHS during die quenching. γ: austenite, α': martensite. (a) High-temperature crack initiation at a α-Fe(Zn) grain boundary in the surface alloy layer. (b) Zn diffusion along the γ grain boundary and transformation of the Zn-diffused γ grain boundary region to α-Fe(Zn). (c) Crack propagation through the weak α-Fe(Zn) grain boundary layer. (d) Crack propagation by repetition of the diffusion-transformation stages (b) and (c). (e) After cooling, the high-temperature Zn_{liq} distribution is reflected in the room-temperature distribution of Γ-Fe_3Zn_{10}. The absence of transformation of Γ to α' lath martensite allows for the identification of the Zn diffusion layer in the vicinity of the crack tip. [5]

Another explanation about LME mechanism was developed by Pańcikiewicz et al [38]. Their experiments focused on joining hot dip galvanised E275D+Z steel with 304 grade steel by gas metal arc welding. Thereby the following interaction of zinc was observed:

Liquid zinc at 419 – 570°C slowly penetrates unstressed base material by forming intermetallic β nickel-zinc compounds. Similar to the depletion of chromium during sensitization (see chapter2.2.1.3), the resulting depletion of nickel in the surrounding areas reduces the stability of the austenite, causing a transformation to α-phase. This leads to internal compressive and possibly tensile stresses resulting in fractures along grain boundaries.

2.1.4.1 Iron – zinc phases

The Fe-Zn phase diagram, embodied in Figure 18 unveils a γ loop, considerable solubility of Zn in bcc Fe (α) at high temperatures, as well as four intermetallic phases: Γ, $Γ_1$, δ and ζ [41]. The Γ phase evolves peritectically at 782°C, the $Γ_1$ phase peritectoidally at 550°C. δ and ζ phases develop through peritectic reactions at 665 and 530°C, respectively.

a) b)

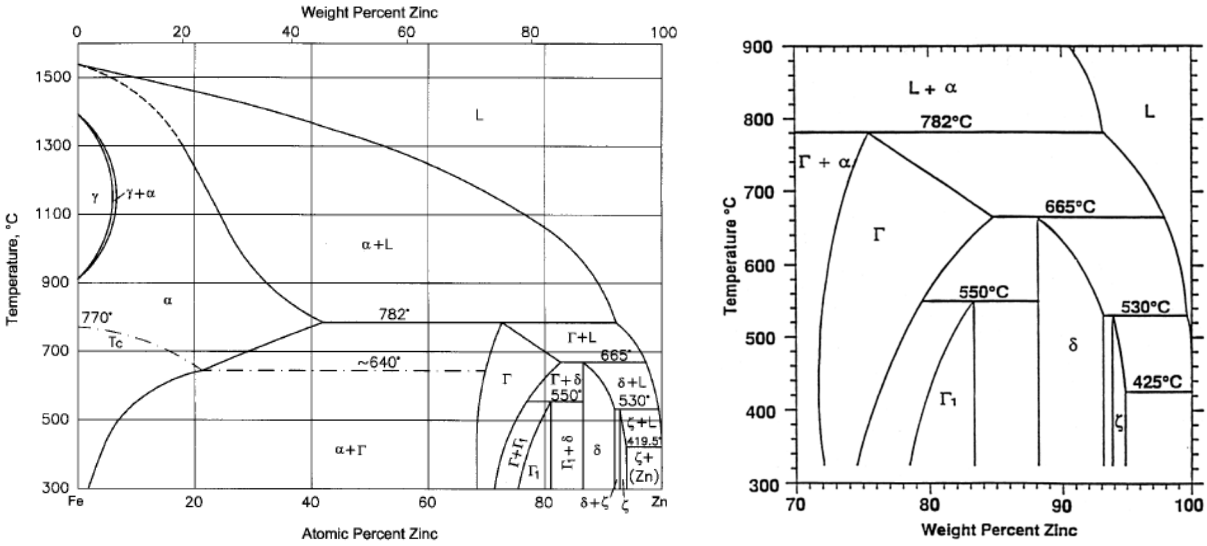

Figure 18: a) Iron – zinc binary phase diagram [42] **b) zinc rich region of the iron – zinc binary phase diagram** [12]

Table 1 lists the possible intermetallic phases of iron and zinc with its chemical designation and range of composition.

Table 1: Intermetallic phases of iron and zinc [42]

Phase	Composition, at.% Zn	Pearson Symbol	Space Group
Γ (Fe_3Zn_{10})	68.5-82.5	*cI*52	$I\bar{4}3m$
$Γ_1$ ($Fe_{11}Zn_{40}$)	75-81	*cF*408	$F\bar{4}3m$
δ ($FeZn_{10}$)	86.5-91.8	*hP*555	$P6_3mc$
ζ ($FeZn_{13}$)	92.8-94	*mC*28	*C*2/*m*

2.1.5 Methods to test LME susceptibility

LME incidents for research purposes were studied by using different methods and techniques. Commonly found ones are listed below.

- *Hot tensile test with embrittling metal coating*

A common method of testing LME is to perform tensile tests with specimens that are coated with embrittling metal and then heated above the melting temperature of the coating. This can be achieved by the means of a Gleeble® simulator [5], [6], [12], [31], [32].

- *Hot tensile tests in liquid embrittling metal bath*

Hot tensile tests in liquid embrittling metal were carried out by [24], [27], [43].

- *Hot tensile test after soaking in embrittling environment*

Hemery et al [37] investigated a Fe18Cr9Ni1Mn austenitic stainless steel in liquid sodium after soaking for 250h in liquid sodium.

- *Cups immersed in liquid embrittling metal*

Beal et al. [25] carried out tests with deep drawn cups of Fe22Mn0.6C TWIP steel that were immersed in liquid zinc.

- *Low cycle fatigue tests in liquid embrittling metal*

Strain controlled low cycle fatigue tests of 9Cr-1Mo steel in lead-bismuth eutectic were performed by Gong et al [14].

- *Welding tests*

Welding tests with different material combinations have been carried out in different studies. Bruscato [11] welded hot dip galvanised carbon steel plate to Type 304L austenitic stainless steel, using E309L electrodes. Ashiri et al [8] used resistance spot welding to test Zn-coated twining induced plasticity steels with a Cu-Cr electrode.

2.1.6 Methods to characterise LME incidents

All of the techniques listed beneath can be found in the literature.

- *LOM – Light optical microscopy*

Light optical microscopy was used by different authors including Bruscato et al [11], Pańcikiewicz et al [38] and Mraz et al [7] in order to investigate and measure cracks and reveal the cracking path.

- *SEM – Scanning electron microscopy*

Scanning microscopy was used by the majority of LME focused researches [6], [14], [24], [37], [43]. This technique is used to investigate the fracture surface of LME tested samples as well as for length characterisation of cracks and coatings in cross sections.

- *TEM – Transmission electron microscopy*

Fewer researchers used TEM technique to investigate LME. Some authors [5], [6], [44], [45] used transmission electron microscopy for high resolution cross-sectional micrographs in order to identify the microstructural features such as enriched areas or different phases within the samples.

- *EDX – Energy-dispersive X-ray spectroscopy*

EDX systems were used to detect different elemental distributions within tested samples and for identifying intermetallic compounds [3], [24], [38].

- *EPMA – electron probe microanalyser*

EPMA found use in the quantification of single elements on sample surfaces [5], [6], [8].

- *EBSD – Electron backscatter diffraction*

In order to gain information about the orientation of grains and to find different phases within a structure EBSD technique was employed [5], [6], [37], [45]

2.2 Stainless steels

Stainless steels are characterised by high corrosion resistance, achieved by a substantial amount of chromium. In oxidational environment, this leads to the formation of a thin oxide layer, passivating the steel and thereby preventing further oxidation. Therefore the chromium has to be evenly distributed in the material. The minimum amount of chromium in stainless steels is 12% [46].

The majority of stainless steels come with a chromium content of 12–18%. Additionally alloying elements such as nickel, molybdenum, nitrogen, titanium and manganese are common in these type of steels [47].

According to the American Iron and Steel Institute (AISI) classification, stainless steels are divided into five groups:

- Austenitic stainless steels
- Ferritic stainless steels
- Martensitic stainless steels
- Austenitic-ferritic (Duplex) stainless steels
- Precipitation hardening stainless steels

In this framework, the focus is set on austenitic stainless steels.

2.2.1 Austenitic stainless steels

The 300 series austenitic stainless steels are characterised by a significant chromium content of at least 16% and a minimum nickel content of 6% as main alloying elements [48]. Their austenitic phase is a face centred cubic - fcc structure resulting from the high amount of austenite stabilising elements inside its matrix [47].

Figure 19 shows the microstructure of a commonly used austenitic stainless steel.

a) b)

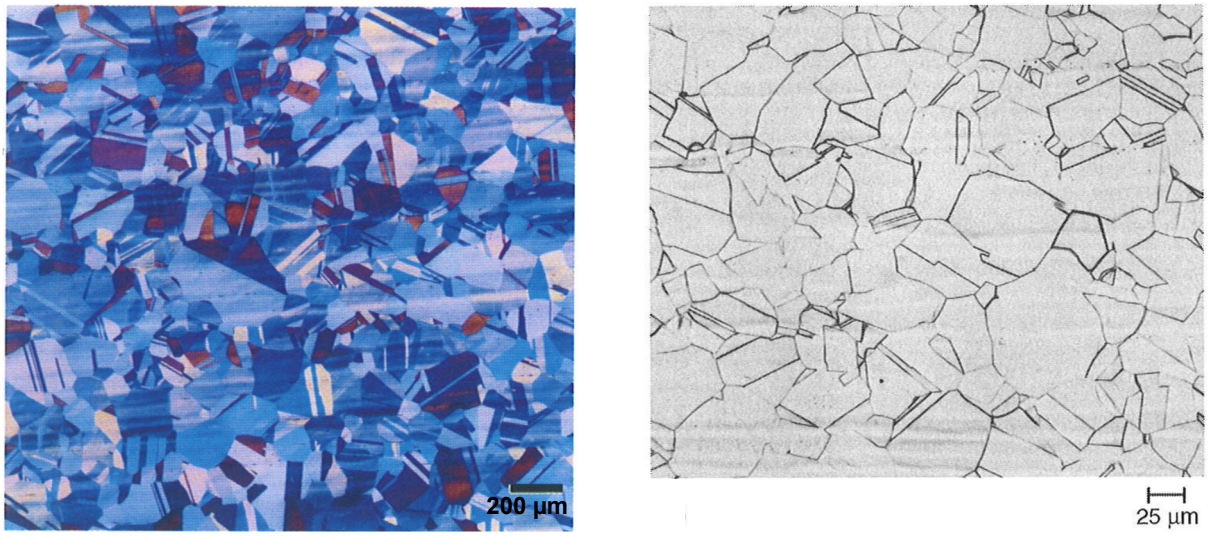

Figure 19: a) Microstructure of 316L steel after hot rolling, cold reducing 30% thickness and solution annealing and etching with Berasha´s BII reagent [49] **b) Grain structure of 316L steel after solution annealing and etching with a waterless Kailing´s tint etch** [50]

Austenitic materials are known for being non-magnetic and having relatively low yield strength but high ductility, high work hardening rates and very good toughness. In addition to superb machining ability those specifications make austenitic stainless steel the most common type of stainless steels.

Another important specificity is the highest corrosion resistance of all groups of steels and the fact that these steels maintain good mechanical properties at elevated temperatures.

The sensitivity of austenite towards intergranular corrosion must be mentioned as downside. When thermally exposed by welding or other thermal processes, chromium tends to precipitate in form of chromium carbides in grain boundaries and deplete in the adjacent area of those [51]. This phenomenon is called sensitization and is further described in chapter 2.2.1.3

Typical applications of austenitic stainless steels are [47]:

- Chemical equipment
- Food equipment
- Kitchen sinks
- Medical devices
- Heat exchangers
- Parts of furnaces and ovens

2.2.1.1 General properties

Some general properties of austenitic stainless steels are [46]:

- Good formability (ductility)
- Good weldability
- Good corrosion resistance, but sensitive to sulphurous mediums and chlorides
- Tendency towards chromium carbide precipitation, resulting in a sensitivity to intergranular corrosion
- Tendency towards stress corrosion cracking

The chemical composition of a selection of 300 series austenitic stainless steels is listed in Table 2.

Table 2: Chemical composition of 300 series steels [48]

	C max.	*Si* max.	*Mn* max.	*Cr*	*Ni*	*Mo*	*Ti*	*Nb*
Steels								
301	0·15	1·00	2·00	16–18	6–8			
302	0·15	1·00	2·00	17–19	8–10			
304	0·08	1·00	2·00	18–20	8–12			
310	0·25	1·50	2·00	24–26	19–22			
316	0·08	1·00	2·00	16–18	10–14	2·00–3·00		
321	0·08	1·00	2·00	17–19	9–12		5×% C min.	
347	0·08	1·00	2·00	17–19	9–13			10×% C min.
316 (Dev. spec.)[a]	0·03–0·08	0·2–0·6	1·6–2·00	16·5–18	11–12·5	2–2·75	0·02 max.	0·02 max.

Some commonly used mechanical properties are listed in Table 3.

Table 3: Mechanical properties of 300 series steels [52]

ASTM Grade	$R_{p\ 0.2}$	$R_{p\ 1.0}$	R_m	Elongation A	Elongation A_{80}	Hardness
	Mpa	Mpa	Mpa	%	%	HR
TYPE 301	300	325	770	65	56	90HRB
TYPE 301LN	360	400	750	55	50	89HRB
TYPE 304	285	315	640	70	57	82HRB
TYPE 304L	255	285	585	70	55	78HRB
TYPE 305	260	280	570	70	56	77HRB
TYPE 316	295	330	600	70		
TYPE 316L	290	320	610		53	80HRB
TYPE 321	260	285	625	70	55	81HRB

2.2.1.2 Influence of alloying elements

Alloying means to change the chemical composition of a steel by adding elements with the purpose to improve its properties in comparison to the material's original performance [47].

Chromium

Chromium is the most important element concerning the formation of the passive film. Several elements can influence the ability of chromium forming this film but no other element can create the properties of stainless steel by itself. This film first appears at a chromium content of around 10%, though it is quite weak at this composition. With a chromium content of 12% steel is designated as stainless. This nomination cannot be taken by word since corrosion can still occur but it supposes a certain stain resistance [51].

Nickel

In sufficient amounts nickel stabilises the austenitic microstructure, which also improves the fabrication properties and the mechanical properties. Adding nickel as alloying element also effectively rises the re-passivation ability of stainless steel [51].

Manganese

Manganese is usually used to increase hot ductility. Its contribution to stabilise ferrite/austenite varies with temperature: at low temperature manganese acts as austenite stabiliser and at high temperatures ferrite stabiliser. Manganese, as an austenite former, can also replace some of the nickel in stainless steel [53].

In stainless steels manganese interacts with sulphur to form manganese sulphides. Depending on morphology and composition, these sulphides may have significant influence on pitting corrosion resistance [47].

Silicon

Silicon improves the oxidation resistance not only in high temperatures but also at lower temperatures in highly oxidative environments. Additionally silicon favours ferritic microstructure and improves mechanical strength [53].

Carbon

Carbon is a strong austenite former and known for providing strength of stainless steels in high temperature applications [53]. For other applications, carbon influences corrosion resistance negatively by its tendency to react with chromium (see chapter 2.2.1.3) [46].

Molybdenum

Molybdenum to some extent increases mechanical strength and favours ferritic microstructure. It also raises the risk of secondary phases in ferritic, duplex and austenitic microstructure [53].

In combination with chromium, molybdenum effectively promotes the formation of the passivation layer. This makes it especially important to improve the resistance to pitting corrosion [51].

2.2.1.3 Sensitization

As previously mentioned, sensitization can occur in austenitic steels when exposed to high temperatures for a certain amount of time. At elevated temperatures chromium tends to react with carbon and precipitate as chromium carbides in the boundary region of grains thus lowering the chromium content in the surrounding area and undercutting the passivation limit of 12% Cr [51].

Figure 20 shows the chromium distribution of austenitic steel close to a grain boundary with a formation of chromium carbides. Close to the edge, the chromium content is very high and one can clearly see the depletion of chromium around this area. There, the chromium content is significantly lower than in the base material and therefore favours intergranular corrosion [54].

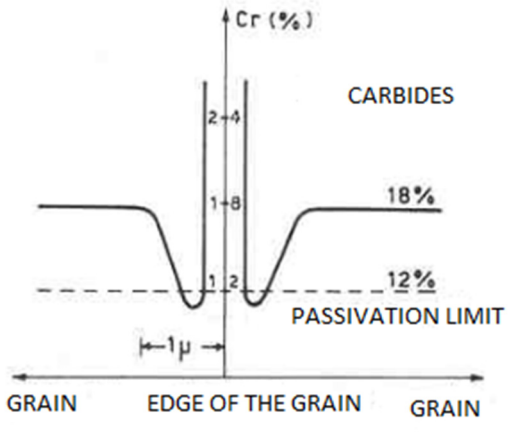

Figure 20: The chromium content trend close to the grain boundaries of a stainless steel [54]

Figure 21 displays the time to sensitization of type 304 stainless steel in respect to temperature and carbon-content. For a 304 type steel with a carbon content of 0.08% one can clearly see that an exposure of 700°C for around 1 min is enough for carbide precipitations to be generated.

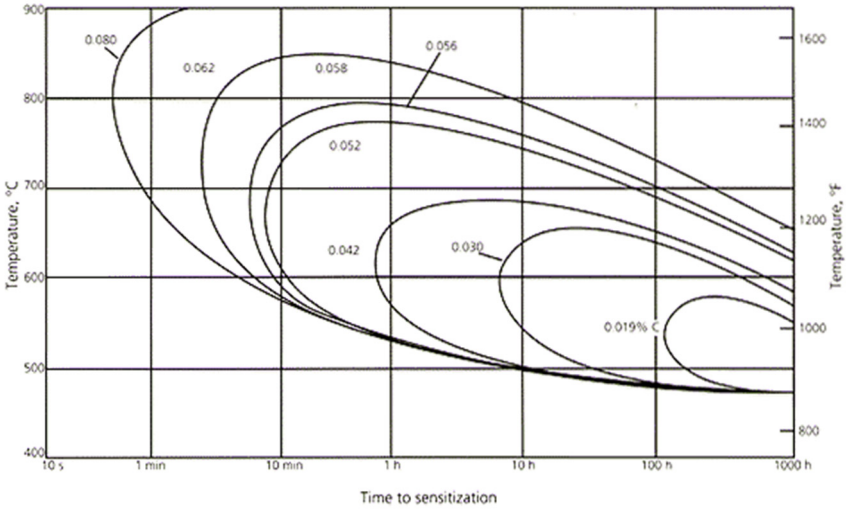

Figure 21: Time-temperature-sensitization curves for type 304 stainless steel in a mixture of $CuSO_4$ and H_2SO_4 containing free copper [51].

This tendency of sensitization occurs in a temperature range of approximately 425 to 870°C. It can be depressed by lowering the carbon content to 0.03% or less and also with the addition of carbide stabilising alloying elements such as titanium, niobium, tantalum and zirconium. Those elements are preferred for the formation of carbides instead of the chromium [51] [47].

2.2.2 Austenitic steel grade 301M – X10CrNi18-8

The material investigated in this study is 301M austenitic stainless steel. The chemical composition of this grade is listed in Table 4.

Table 4: Chemical composition of 301M [55]

Grade designation	EN	C	Cr	Ni	Mn	Si	Fe
301M	1.4310	0.1	17.3	7.3	0.9	0.6	bal.

European designation: X10CrNi18-8/1.4310 American designation: Type 301

It is characterised by [55]:

- fairly low nickel content
- strong mechanical characteristics, promoted by high carbon level
- really low sulphur content combined with the chromium content, guaranteeing strong pitting corrosion resistance
- good formability without risk of delayed cracking after deep drawing
- good weldability
- good polishing ability

2.2.2.1 Microstructure

This austenitic grade is fully constituted by face centred cubic austenite. Cold deformation might induce a transformation of the austenite into martensite. The standard annealing treatment for this steel is performed at 1050°C and followed by a quench.

Figure 22 shows the typical microstructure for this grade of steel after deformation.

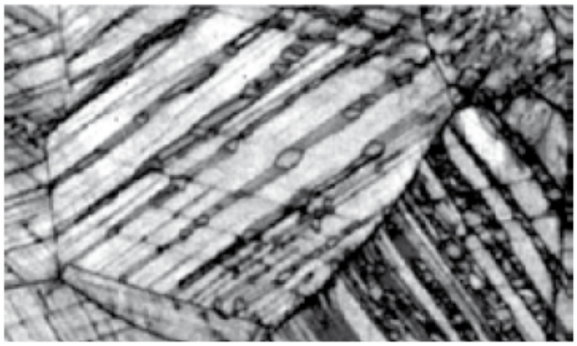

Figure 22: Microstructure of deformed austenite [55]

2.2.2.2 Purpose of this alloy

301M steel offers a stable austenitic phase. Its high potential for work hardening makes it possible to achieve an Ultimate Tensile Strength of 950 MPa and more. This ability qualifies this steel grade for the use in applications where safety is required such as rolling stock, pressure cooker closure systems or safety shoe reinforcement [55].

2.2.2.3 Mechanical properties [55]

Table 5 provides the mechanical properties of 301M grade steel.

Table 5: Mechanical properties of 301M [55]

Grade designation		Rm MPa	Rp0.2% MPa	A %
	A pillar target	950-1100	650-800	>26
301M	C1000	1000	740	30

The high work hardening potential allows to order 301M in a wide range of mechanical properties. For this grade an ultimate tensile strength UTS of 1000 MPa has been chosen to fulfil sufficient yield strength and elongation. An elongation of 30% allows the fabrication of difficult parts [55].

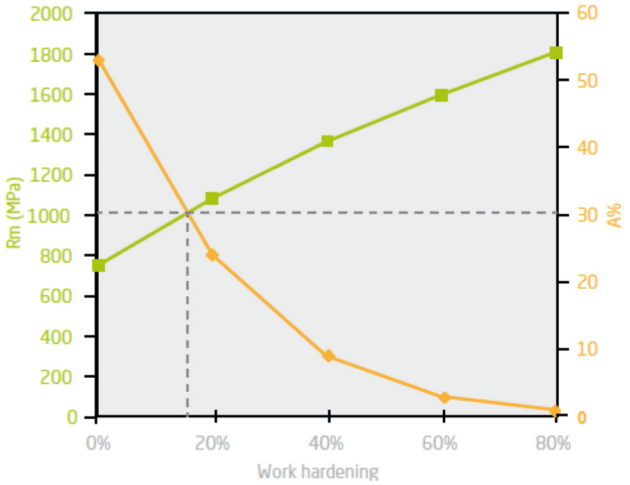

Figure 23: Work hardening point of 301M grade steel [55]

2.3 Overview of zinc coatings

Zinc is a well suited corrosion protection for iron, commonly used since 1979. Because of its dense and adherent corrosion by-products the rate of corrosion is considerably reduced over ferrous materials [56].

There is a number of different zinc coatings on the market which vary in adhesion to the base material, hardness, corrosion resistance and thickness. Figure 24 gives an overview of some of them.

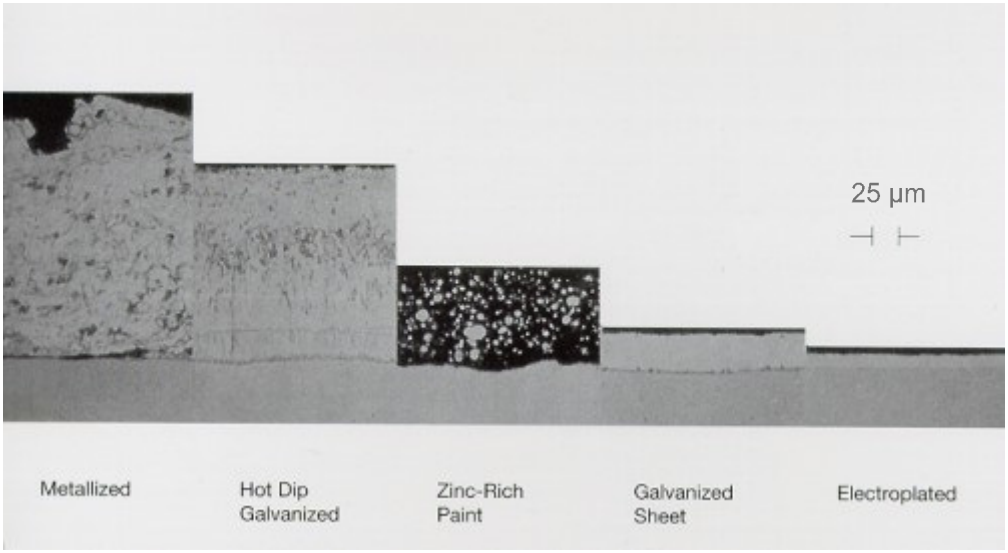

Figure 24: Microstructure of different zinc coatings [57]

- Metallizing

Metallizing is carried out by delivering zinc in form of a wire or powder through a heated gun where it is melted and distributed onto the part with the help of compressed air or combustion gases

- Hot dip galvanising

Hot dip galvanising, also known as galvanising, produces a zinc coating on iron as well as steel products through immersion of the material in liquid zinc. Prior, the steel has to be cleaned by a common procedure of degreasing, pickling and fluxing.

- Zinc painting

Zinc painting names the application of zinc dust mixed with organic or inorganic binders with the help of a brush. The zinc rich paintings usually contain 92-95% metallic zinc in dry film. Before applying, the surface of the steel must be properly cleaned to near white metal.

- Sheet galvanising

Following the hot dip galvanising process, the zinc coating gets physically wiped by air knives in order to receive a consistent coating across the whole coating surface.

- Electro-galvanising

This electro-chemical process produces pure zinc coatings tightly adherent to the steel. The zinc layer is highly deformable and stays intact even after severe deformation.

Figure 25 gives an overview of the different zinc coatings and some additional specifications.

Zinc Coatings				
Method	*Process*	*Specification*	*Coating Thickness*	*Application*
Electrogalvanizing	Electrolysis	ASTM A 879	Up to 0.28 mils[1] (7.11µm)	Interior. Appliance panels, studs, acoustical ceiling members
Zinc Plating	Electrolysis	ASTM B 633	0.2 to 1.0 mils[2] (5.1 to 25.4µm)	Interior or exterior. Fasteners and hardware items.
Mechanical Plating	Peening	ASTM B 695	0.2 to 4.3 mils[2] (5.08 to 109.2µm)	Interior or exterior. Fasteners and hardware items.
Zinc Spraying (Metallizing)	Hot Zinc Spray	AWS C2.2	3.3 to 8.3 mils (83.8 to 210.8µm)	Interior or exterior. Items that cannot be galvanized because of size or because on-site coating application is needed.
Continuous Sheet Galvanizing	Hot-Dip	ASTM A 653	Up to 4.0 mils[1] (101.6µm)	Interior or exterior. Roofing, gutters, culverts, automobile bodies.
Batch Hot-Dip Galvanizing	Hot-Dip	ASTM A 123 ASTM A 153 ASTM A 767 CSA G164	1.4 to 3.9 mils[3] (35.6 to 99.1µm)	Interior or exterior. Nearly all shapes and sizes ranging from nails, nuts, and bolts to large structural assemblies, including rebar.
Zinc Painting	Spray Roller Brush	SSPC-PS Guide 12.00, 22.00 SSPC-PS Paint 20 SSPC-PS 12.01	0.6 to 5.0 mils/coat (15.2 to 127µm/coat)	Interior or exterior. Items that cannot be galvanized because of size or because on-site coating application is needed. Large structural assemblies. Aesthetic requirements.

[1] Total for **both sides** of sheet.
[2] Range based on **ASTM minimum thicknesses for all grades, classes, etc., encompassed by the specifications.**
[3] Range based on **ASTM and CSA minimum thicknesses** for all **grades, classes, etc., encompassed by the specifications.**

Figure 25:Specifications of different zinc coatings [56]

3. Experimental procedures

After reviewing the literature this section describes the procedures carried out during this work.

3.1 Specimen

The tested material is a grade 301M austenitic stainless steel, provided by the company Aperam.

As a base material for samples tested during this work, a sheet of 1.2 mm thickness was used which underwent the process displayed in Figure 26.

The slabs that formed after casting were hot rolled, cold rolled, annealed at 1050°C, afterwards pickled and skin-rolled until reaching its target thickness.

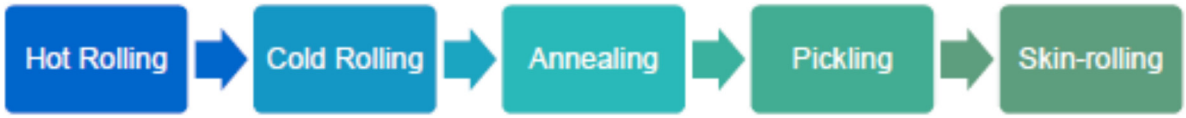

Figure 26: Production procedure of 301M steel sheets of 1.2mm thickness [1]

Afterwards the specimens for the tensile tests were laser cut out of the base material sheets in the shape displayed in Figure 27. This shape was chosen for the usage in the thermo-mechanical simulator. The samples were cut out in a way that the tensile direction of the sample was perpendicular to the rolling direction of the sheet.

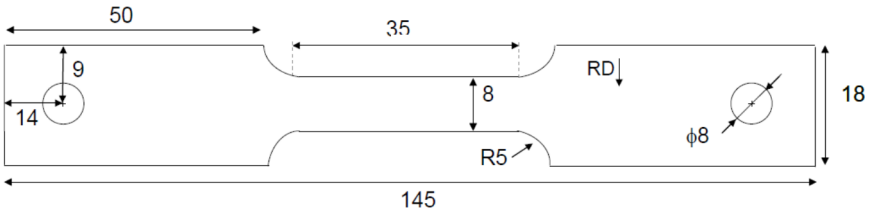

Figure 27: Shape and dimensions of tensile specimen

3.2 Coating

Two different coating methods were used with the aim of studying the possible influence of the coating method on the embrittlement. Both are described within this chapter.

3.2.1 Painting

For zinc application by painting, a one component zinc-rich paint from the company ZINGA was used. It consists of 96% Zn dust by weight in its dry film. The rest is binder and aromatic hydrocarbons [58].

Before application, the tensile specimen were cleaned with ethanol. The paint was stirred for several minutes until one homogenous fluid developed. Finally the zinc coating was applied with a commercial paintbrush on the centre part of the specimen, only on one side, as shown in Figure 28. It was taken care of that the applied coating was as homogenous as possible. The samples were then kept for several hours under aspiration to dry the painted layer. Finally after the paint dried, the remains of the coating which were found on any other side than the front were carefully removed with the help of a scraper.

Figure 28: Sample of 301M material with zinc-rich painting

Figure 29 shows the zinc enriched painting which was investigated with SEM in order to check the thickness of the layer. It was found that the zinc layer is about 40 µm along the whole painting area.

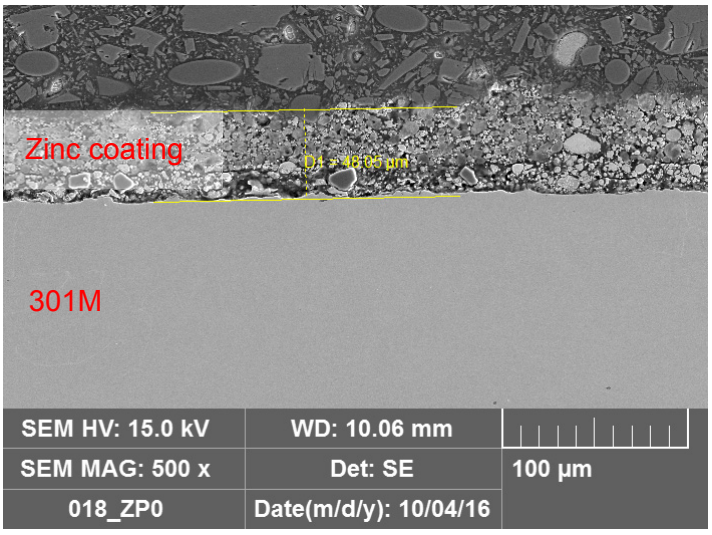

Figure 29: SEM micrograph of a layer of zinc-enriched painting on 301M steel

3.2.2 Electro-galvanising

Figure 30a) displays the principle of electro-galvanising. The bare specimen (Me) is immersed in an electrolytic bath. The specimen is set as a cathode and a preferably pure zinc electrode (Zn) is used as anode. When applying a voltage (- +), the resulting current leads to dissolution of the coating material (pure zinc) which goes into solution and through adsorption a reduction at the specimen takes place. This leads to a relatively constant metal plating of the specimen. The thickness of the plating layer increases with longer time and / or higher electrical current density [59].

Figure 30b) shows the practical setup that was used for the electro-galvanising process. As electrolyte, a product of the ATOTECH Company was used. Specifically it was weak-acidic, ammonium-free zinc electrolyte designated Zylite 1160, containing mainly boron acid, zinc chloride and potassium chloride. On anodic side a pure zinc bar (99,995%) was used. A regulated power supply unit was used to apply the voltage to the system. The process was carried out with a current density of around 25 mA/cm^2 for different times to achieve thicknesses of 2.5 and 10 µm.

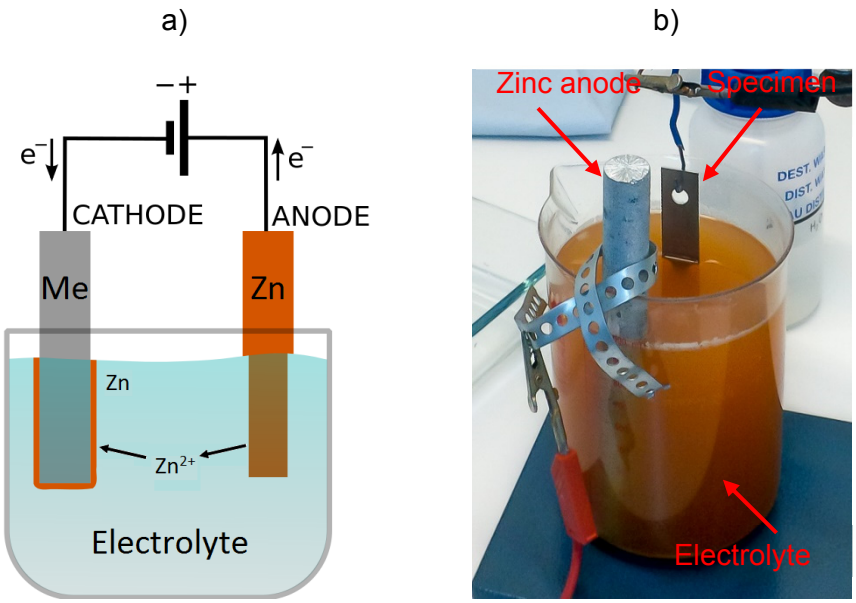

Figure 30: Electro-galvanising: a) Principle of electro-galvanising / adapted from [59] **b) Setup for electro-galvanising in the laboratory of the IWS**

The growth rate of the zinc layer over time is displayed in Figure 31a). During several test series a linear increase over time has been determined. In b) a SEM micrograph of the electro-galvanised zinc layer with a target thickness of 10 µm is shown.

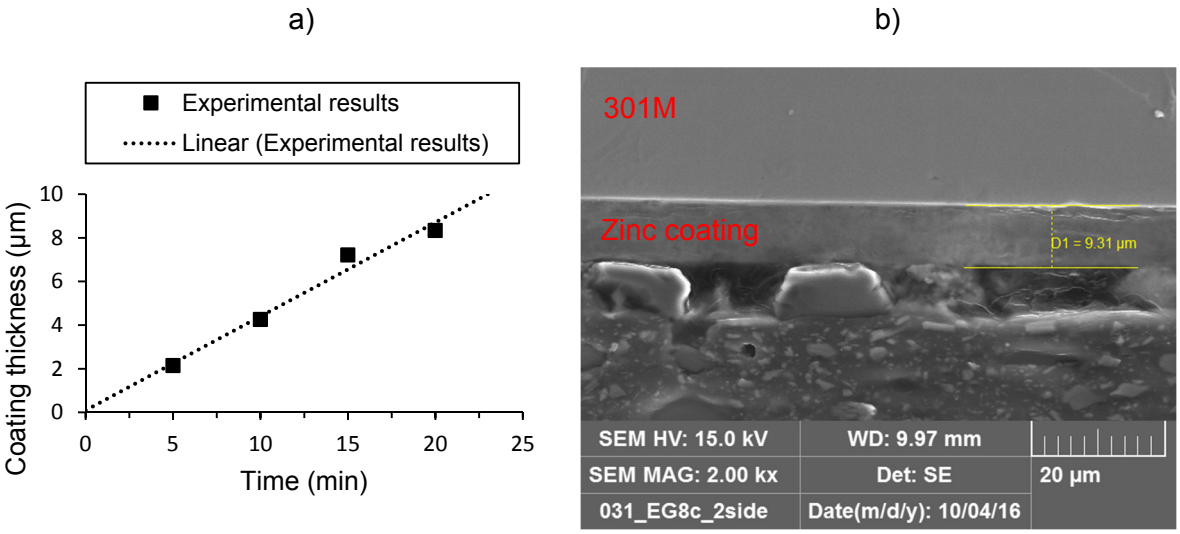

Figure 31 a) Linear growth of zinc coating on 301M by electro-galvanising b) SEM image of electro-galvanised coating on base material

Based on this method, the electro-galvanised samples used during this investigation were produced. To reach 2.5 µm and 10 µm thick zinc coating, 6 min and 23 min were necessary, respectively.

3.3 Thermo-mechanical tests

To investigate the embrittlement that occurs during spot welding in a laboratory environment the chosen test method was to perform specific hot tensile tests with a Gleeble® simulator. In this project the Gleeble® 3800 simulator came to use. All mechanical tests were carried out with the help of this device. The advantage of this system is the high accuracy of reproducibility and the ability to make fast changes to different test parameters.

For every testing condition at least two repetitions have been made and in case of non-conformity additional tests have been carried out with the goal of minimising inaccuracies in the test setup. The results shown in chapter 4 display the average curves of all repetitions.

For all tests covering the effects of LME also bare samples were tested in order to get a reference behaviour to compare the zinc painted samples to and thereby characterise the influence of LME.

3.3.1 Principle

To investigate the embrittlement that occurs during spot welding in a laboratory environment the chosen test method was to perform specific hot tensile tests with a Gleeble® 3800 simulator. The advantage of this system is the high accuracy of reproducibility and the ability to make fast changes of possibly influencing parameters.

This device enables to carry out thermo-mechanical cycles with high dynamics, similar to those encountered during spot welding processes and others. Parameters such as temperature and mechanical load, as well as strain rate, heating rate, force can be controlled through a driving computer. Also data recording of all the internal sensors of the machine is carried out with this computer.

Figure 32 shows the scheme of the Gleeble and the model used by the Institute of Material Science and Welding of the TU Graz.

a) b)

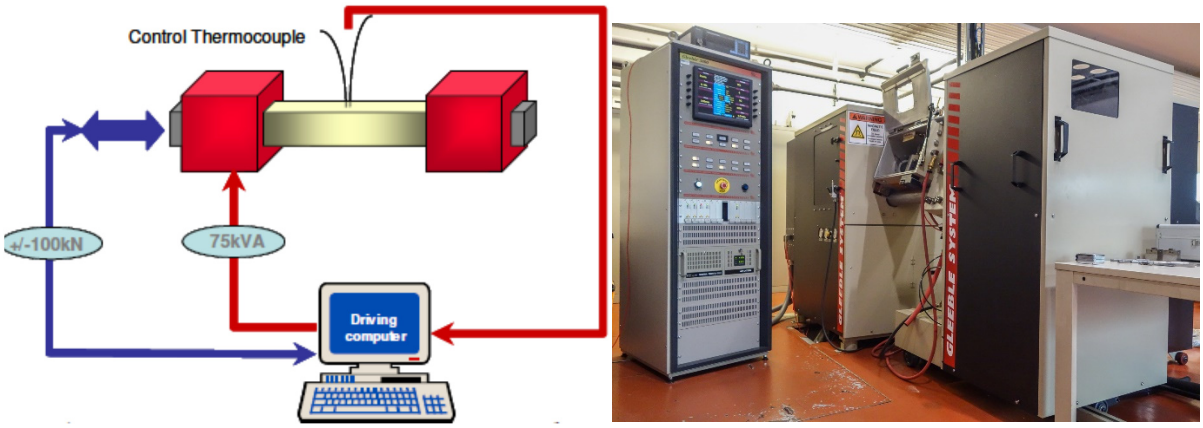

Figure 32: Gleeble 3800 simulator: a) Scheme [3] **b) Image of the Gleeble® simulator at TU Graz**

Figure 33 shows the inside of the test chamber of the Gleeble® simulator. The temperature of the specimen can be influenced by changing the electrical current, conducted via the copper grips and copper jaws through the sample and thereby heating it up. This process is addressed to the Joule effect. The temperature can also be rapidly decreased by air or water quenching. The mechanical load can be adjusted by moving the flexible end of the copper jaws in longitudinal direction.

a) b)

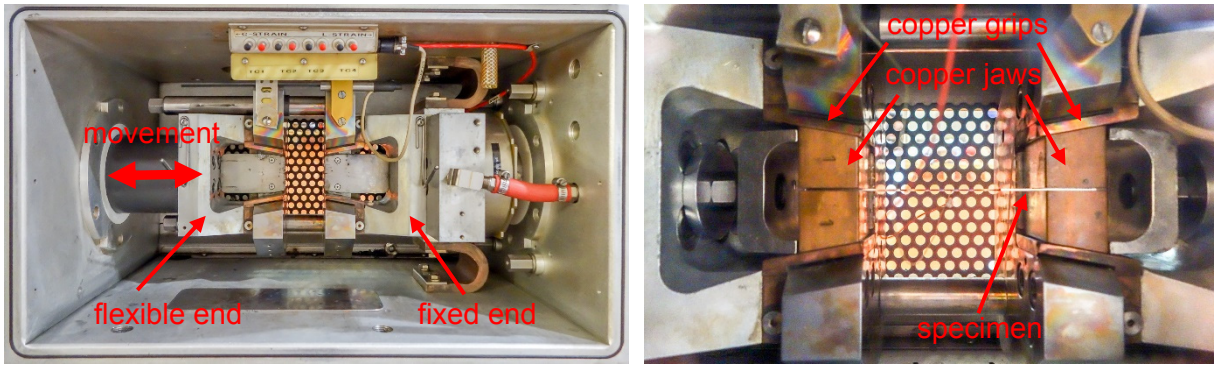

Figure 33: Chamber of Gleeble® 3800 simulator: a) empty chamber b) detail of chamber loaded with specimen and prepared for testing

A major advantage of this system is that thermo-mechanical cycles can be controlled dynamically and independently from each other. Different control modes can be changed during a running test procedure between force, stroke, stress and strain. The chamber can also be set under vacuum or inert gas atmosphere.

3.3.2 Specimen preparation

A type K thermocouple was welded in the centre of the specimen (see Figure 34a)) to permit the control of the temperature during testing. Therefore the samples underwent the following procedure:

At first, the oxide layer of the sample was removed by hand-grinding followed by ethanol cleaning. Afterwards the sample was designated with a marker, the thickness and width in the centre was measured and logged in a database. The centre of the sample was marked for the positioning of the thermocouple as well. Finally, the thermocouple was welded with the help of the thermocouple welder, displayed in Figure 34b). The best results were achieved with a voltage setting of 38-45 V.

a) b)

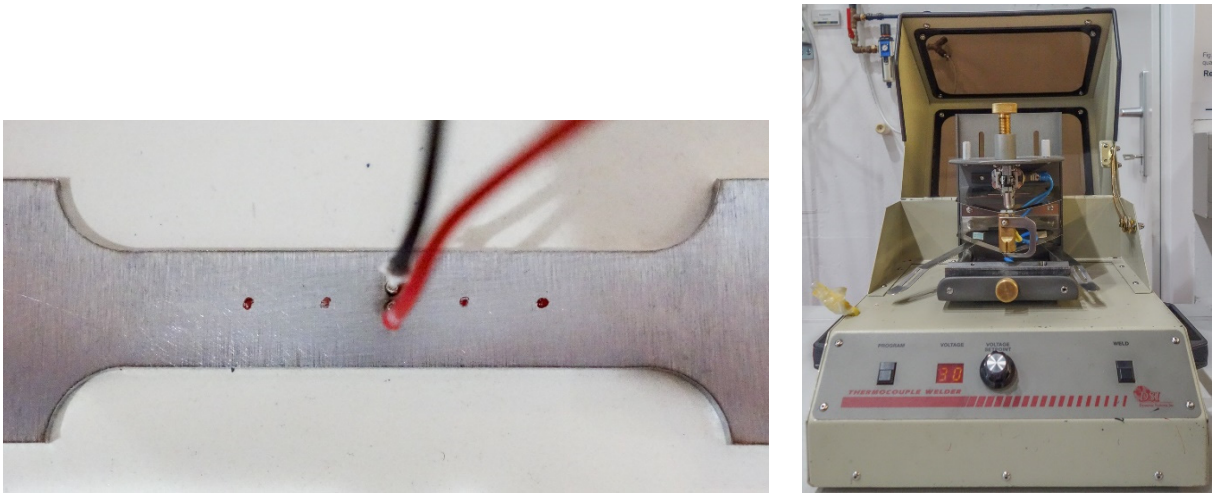

Figure 34: a) Tensile specimen with welded central thermocouple and marks for further thermocouples b) Thermocouple welder by DSI

3.3.2.1 Temperature distribution within the sample

In order to gain information about the temperature distribution within the samples when heated to high temperatures, some specific tests have been performed. Therefore, samples were outfitted with additional thermocouples in different distances from the centre of the sample (± 5/10/12.5 mm) with the aim of measuring the temperature profile at different temperatures (400–1000°C; 100°C steps in between).

The results revealed that the homogeneous temperature zone got smaller with increasing temperature. This zone was defined by a maximum temperature deviation of 10°C from the target temperature.

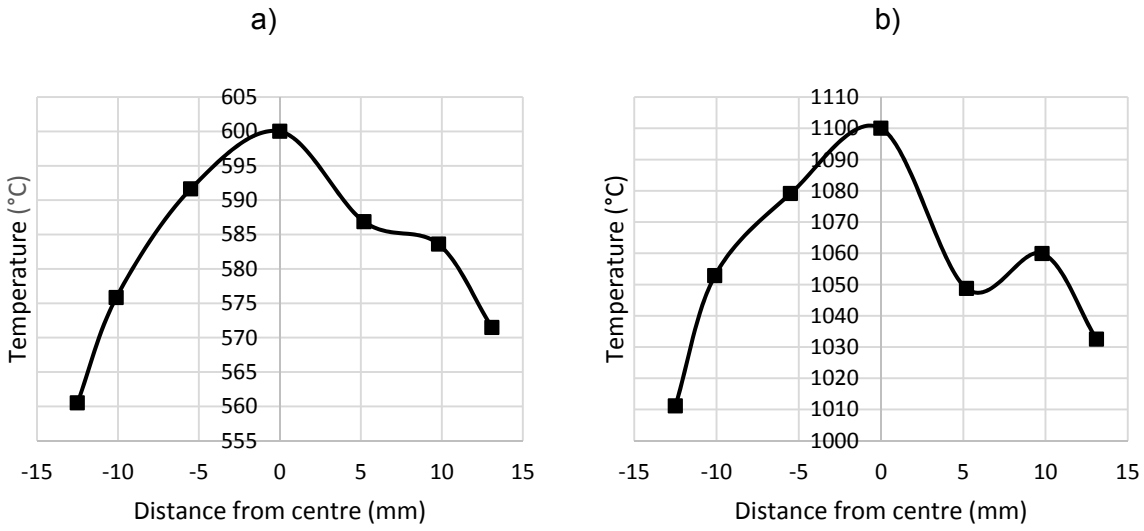

Figure 35: Temperature profile of tensile specimen at: a) 600°C b) 1100°C

In order to get a better understanding of the real temperature where cracks appeared and at which temperature the rupture appeared, each tested sample was virtually divided into 3 different zones. Figure 36 gives an overview about these zones where zone 1, zone 2 and zone 3 where defined as T_{target} till T_{target} -10°C, T_{target} -10°C till T_{target} -50°C and less than T_{target} -50°C, respectively.

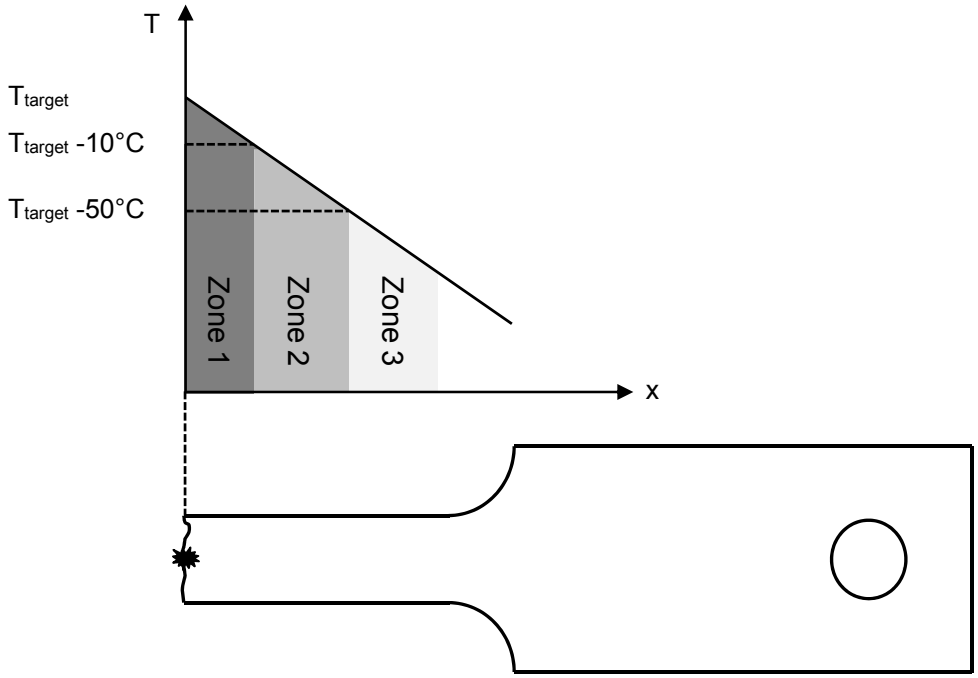

Figure 36: Illustration of 3 different temperatures zones within a ruptured samples

3.4 Thermo-mechanical cycles

Different thermo-mechanical cycles were realised with the Gleeble® simulator. All tests were carried out in air atmosphere.

3.4.1 Tensile test

The base material was tensile tested at room temperature to get a reference behaviour for comparative reasons. Also the specimen that went through the interrupted test without being ruptured were tensile tested at room temperature to investigate how much the interrupted tests had pre-damaged the samples. All room temperature tensile tests were performed with 1 mm/s displacement speed on the Gleeble® simulator.

3.4.2 Hot tensile test

Hot tensile tests were performed in a temperature range of 600–1100°C with displacement rates of 1 mm/s and 100 mm/s. The thermo-mechanical cycle of a hot tensile test at 800°C is shown in Figure 37.

The sample is heated with 80°C/s to its target temperature of 800°C. Thereby the stroke is constantly increased in order to compensate the thermal expansion thus avoiding bending of the sample. When reaching the target temperature, the stroke level is reset to null and the tensile test starts. With a displacement rate of 1 mm/s, the maximum stroke of 15 mm is reached after further 15 s, while the temperature is still kept constant. During this time, force increases until rupture of the sample. Afterwards the sample cools down due to heat transfer to the copper jaws and the surrounding air.

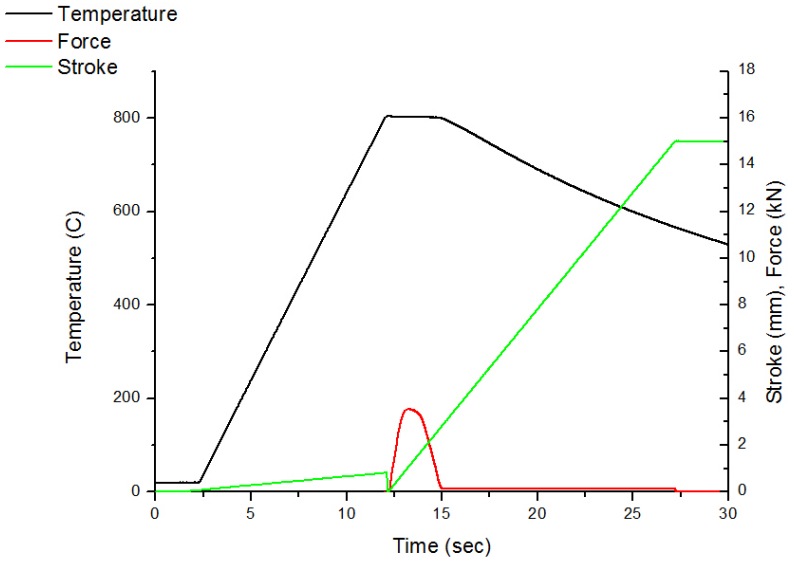

Figure 37: Thermo-mechanical cycle at 800°C

3.4.3 Interrupted test

Interrupted hot tensile tests were carried out in order to find the point of crack initiation and observe crack growth with respect to displacement. Therefore, specific hot tensile tests have been performed. The hot tensile tests were stopped at different stroke levels before the sample was fully ruptured. Those tests were carried out with a displacement rate of 100 mm/s at 800°C since the faster tests turned out to be the most reproducible ones. After stroke levels of 0.5, 0.7, 1.0 and 1.5 mm the straining has been stopped and the specimen was cooled down with water while the force was reduced to null.

3.4.4 Hot tensile test with pre-exposure time

The influence of time of contact between the steel and liquid zinc was also tested with the Gleeble® system. After reaching the target temperature of 800°C, pre-exposure times of 5–40 s were applied to the specimen and subsequent tensile test was conducted at the same temperature with a displacement rate of 100 mm/s.
This thermo-mechanical cycle is displayed in Figure 38.

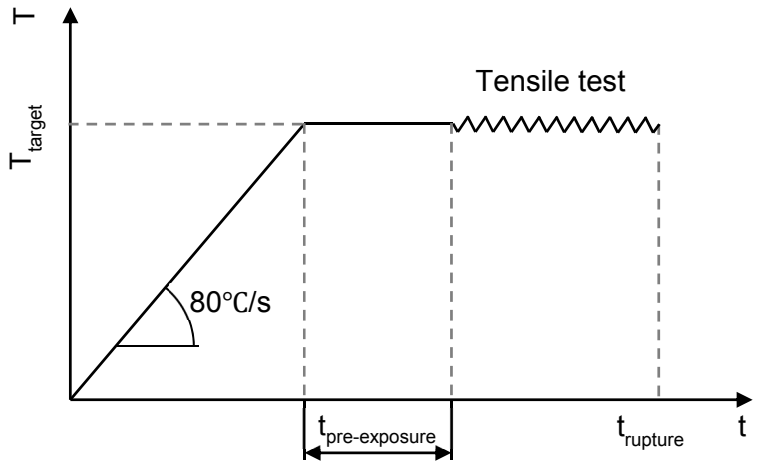

Figure 38: Thermo-mechanical cycle for hot tensile tests with pre exposure time

3.4.5 Towards resistance spot welding simulation

A specific test procedure has been developed with the goal of being more comparable to the resistance spot welding (RSW) cycle.

Based on the RSW procedure, at first the mechanical tensile load was applied to the specimen. Afterwards the zinc coated sample was heated up to different target temperatures while attempting to keep the force constant. After reaching the target temperature the force and temperature was held for 1 s additionally. Subsequently the force was reduced to null and the specimen was cooled down by heat transfer through the copper jaws and surrounding air.

With the experience of previous tensile tests, a pre-tension value of 3 kN was chosen for the first test series. This value was built up linear in force-control mode in a time span of 5 s, resulting in a force rate of 0.6 $kN.s^{-1}$. Afterwards, the sample was heated with a heating rate of 80°C.s^{-1} to different target temperatures. Of course, for simulating a RSW process a higher heating rate would be desired but limiting factors lead to this chosen value. Higher heating rates resulted in a decrease of force during the heating process due to the inertia of the machine not being able to compensate the thermal expansion.
The idea behind this routine was to check for a given force at which temperature LME-induced cracks start to appear.

3.5 Quantification of embrittlement

As characterisation of embrittlement and to compare tests to one another the quantity of energy to fracture has been calculated as the area under the curve of the force-stroke diagram.

$$E_{fracture} = \int F_{tensile} \cdot ds$$

Formula 1: Definition of fracture energy

For each test, the values were numerically integrated with the help of Origin Studio software and the reduction of fracture energy of the zinc-coated sample in respect to the bare sample was plotted as a function testing temperature. The reduction of fracture energy was defined as:

$$\Delta E_{red} = \frac{E_{bare} - E_{coated}}{E_{bare}}$$

Formula 2 Definition of reduction of fracture energy

3.6 Microscopy investigations

Following the analysis of Gleeble® test data a metallography matrix was created. Therefore samples of interest were chosen to be examined with light optical and/or electron microscopy.

3.6.1 Metallography

Samples chosen for fracture surface analysis do not need require any specific preparation.

All other sample chosen for microscopy investigation underwent the following procedure:

- Cutting the sample to desired size
- Embedding sample in epoxy resin
- Grinding in the following steps with Silicon Carbide grit: 80, 160, 320, 500, 800, 1200, 2000, 4000
- Polishing with following steps: 3, 1 µm grain size

- OPS polishing with colloidal silica and 0.25 µm grain size
- Ethanol cleaning and air drying

Samples chosen for EBSD measurements additionally underwent a vibration polishing treatment in Struers AP-A solution with 0.05 µm gamma alumina for a duration of 16 hours.

3.6.2 Light Optical Microscopy (LOM)

The embedded and polished samples were analysed by means of a light optical microscope; in this case a Zeiss Axio Observer.Z1m. The goal was to observe the longitudinal section of the sample (as shown in Figure 39) and quantify the appearance of cracks (number of cracks, average crack length, maximum crack length, total crack length and position of crack).

Figure 39: Light optical image of cracks induced by LME

As shown in chapter 3.3.2.1 the temperature cannot be considered as constant over the whole length of the sample. Therefore each sample was virtually divided into 3 temperature zones and the cracks were accounted separately for each of those.

3.6.3 Stereo Microscopy

Samples that underwent the RSW simulation test have been observed with a stereo microscope. A Zeiss Discovery V20 was used for this purpose.

3.6.4 Scanning Electron Microscopy (SEM)

After evaluation of the Gleeble® data and light microscopy data some samples were picked for further investigation in different scanning electron microscopes (SEM).

The aim was to get a better understanding of the crack path and due to the higher magnification and increased resolution possibly find some traces for zinc penetration and intermetallic compound formations.
Also some samples were chosen for fracture surface analysis using a SEM.

3.6.5 Energy-dispersive X-ray spectroscopy (EDX)

In order to get a better understanding of the behaviour of zinc in the embrittling process EDX scans were performed. Especially the area of the zinc layer and also the element distribution over a cracked area was investigated.

Therefore the following hardware was used:

- LEO 1450 VP (ZEISS) + Bruker EDX
- TESCAN MIRA 3 + EDAX Octane Super Silicon Drift Detector EDX

3.6.6 Electron backscatter diffraction (EBSD)

To conclude the microscopic investigation one sample was investigated with EBSD technique aiming to reveal the expected brittle fracture mode along grain boundaries and detect possible phase changes.

A TESCAN MIRA3 + EDAX Hikari XP2 EBSD detector was used to fulfil this task. Results were analysed with OIM Analysis 7.1.0 Software.

4. Results and discussion

After a review of the literature and a description of the experimental procedure including an overview of used techniques in this section results of the performed experiments are listed and discussed.

4.1 Tensile behaviour of 301M

The tensile behaviour of the base material was tested at room temperature and at elevated temperatures.

4.1.1 Room temperature behaviour

Tensile tests at room temperature were performed using a strain rate of 1 mm/s. The results of engineering stress and strain are shown in Figure 40. The material exhibits an UTS of around 1000 MPa with an elongation to rupture of around 30%, which confirms the target values provided by the steel producer [55].

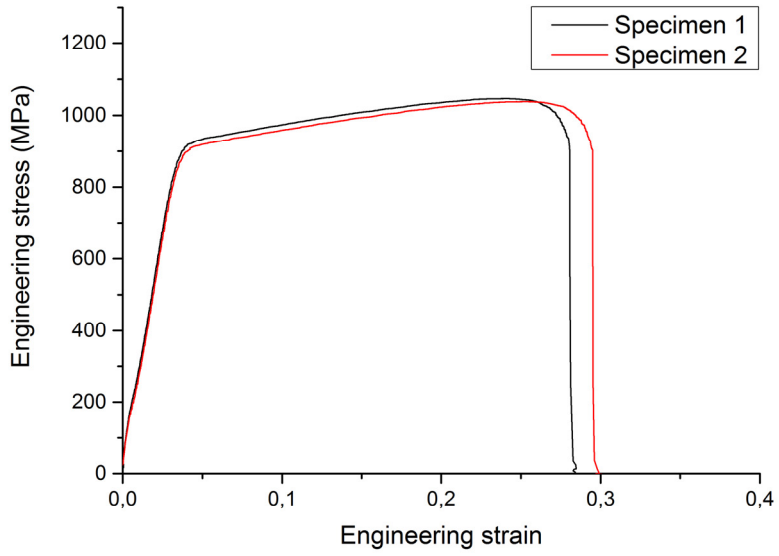

Figure 40: Engineering stress-strain curves of 301M obtained at room temperature with a strain rate of 1 mm/s

The calculated values for true strain and true stress are shown in Figure 41.

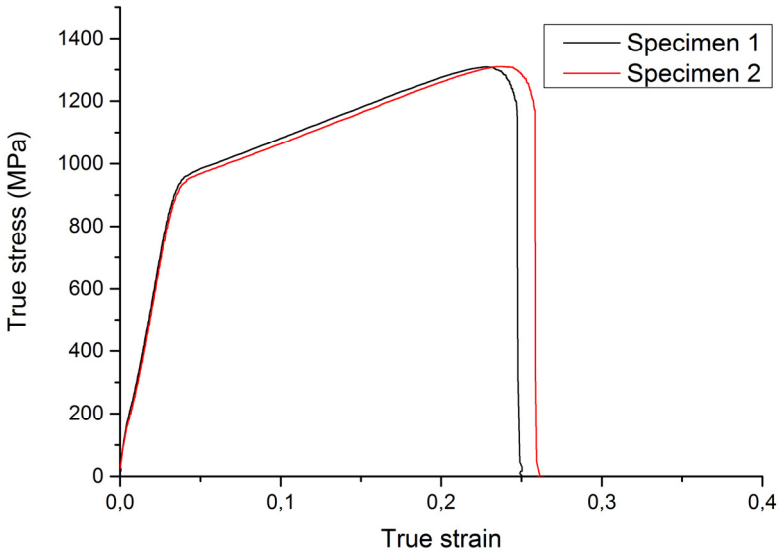

Figure 41: True stress-strain curves of 301M obtained at room temperature with a strain rate of 1 mm/s

4.1.2 High temperature behaviour

Figure 42 gives an overview of the mechanical behaviour of 301M steel at high temperatures observed during tensile testing with strain rates of 1 mm/s and 100 mm/s.

In both cases a clear trend of decreasing maximum force with increasing temperature is apparent in the Force-Stroke diagram. Also the maximum elongation, displayed through the stroke, follows a trend of higher elongation to rupture with increasing temperature. However, the temperature 700°C at 1 mm/s as well as 700°C and 800°C at 100 mm/s present an exception to the temperature-elongation trend. This could be linked to the occurrence of $M_{23}C_6$ precipitation which is further described by Lewis et al. [60].

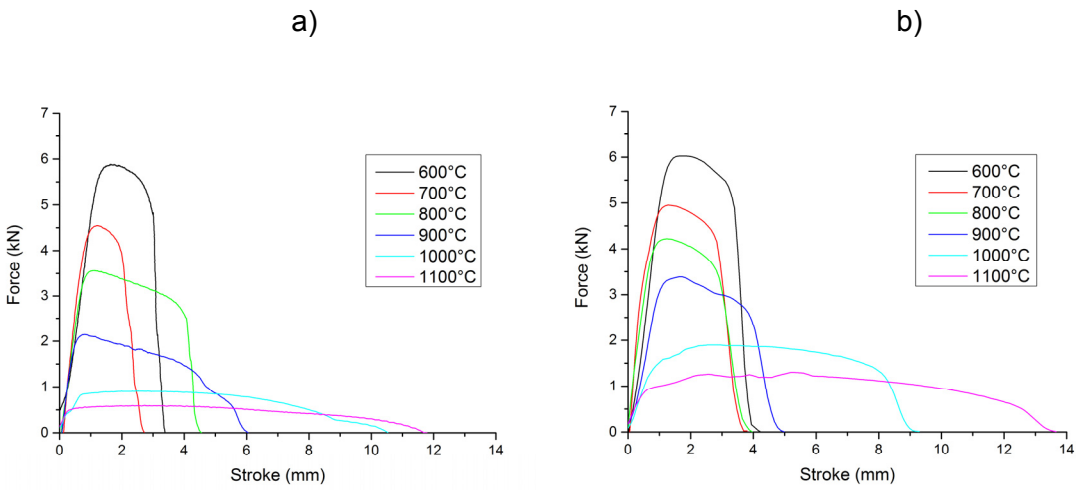

Figure 42: Force-Stroke diagram of 301 steel at different temperatures: a) with 1 mm/s strain rate b) with 100 mm/s strain rate

4.2 Sensitivity of 301M steel to embrittlement by liquid zinc

The results of LME in the most severe conditions found during this investigation are displayed in Figure 43a). The diagram presents the mechanical behaviour of bare and zinc-painted 301M steel during a hot tensile test. The test was carried out at 800°C with a strain rate of 1 mm/s. One can clearly see the effects of LME as the elongation to rupture experiences a drastic reduction in case of the zinc-coated sample. Additionally the maximum force is fairly reduced. Finally, this leads to a massive reduction of absorbed fracture energy in case of the sample coated with zinc.

It is worth pointing out that the mechanical behaviour shown in the Force-Stroke diagram is not influenced by the liquid zinc until preliminary fracture occurs.

In b), a macroscopic picture of both samples is displayed. For the ZP sample the fracture occurs at a very low elongation value. Therefore no signs of necking are observed in the macroscopic image. On the other hand, the bare sample shows clear signs of necking in the centre zone typical for such material.

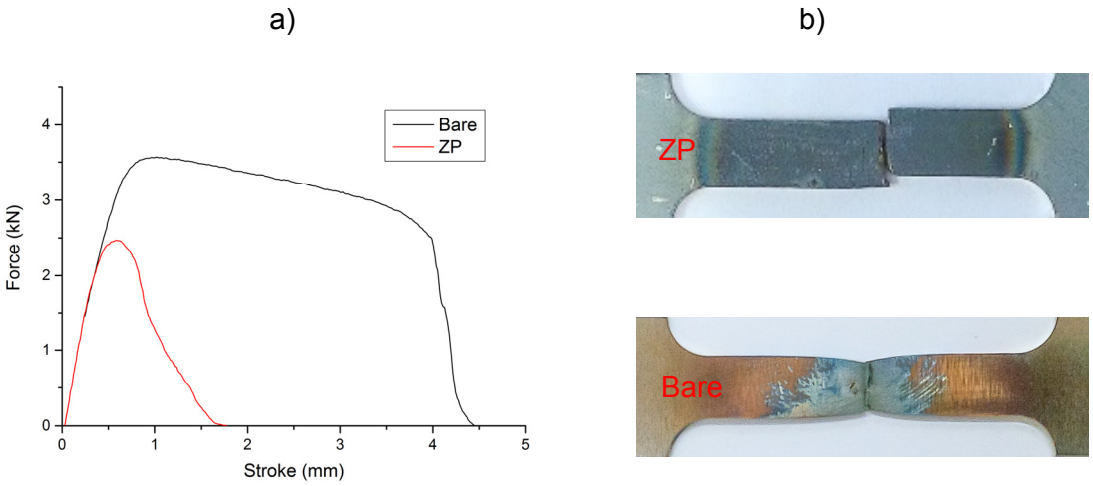

Figure 43 a) Force-Stroke diagram of bare and zinc-painted 301M steel tensile tested at 800°C with 1 mm/s train rate b) macroscopic image of bare and zinc painted samples

4.3 Results of thermo-mechanical tests

In this section, the influence of different parameters on the LME process is shown. At first the temperature range where LME occurs is discussed, followed by results concerning the influence of strain rate, time of contact between liquid metal and base material, influence of coating method and influence of coating thickness (amount of embrittling metal).

Finally the results of interrupted tests and some welding approximation tests are shown and discussed.

The reproducibility in some conditions was moderate, sometimes leading to fairly different levels of maximum force especially of zinc-coated samples. Therefore the average of multiple curves was calculated and used for the following results shown in this chapter. Figure 44 presents the individual test results while the averaged version is displayed in Figure 43a). It should be stated that this test series represents the worst case in terms of reproducibility experienced during the present work.
Furthermore, it can be concluded that the criterion of reproducible critical stress for occurrence of LME, introduced by Beal [3], cannot be applied here.

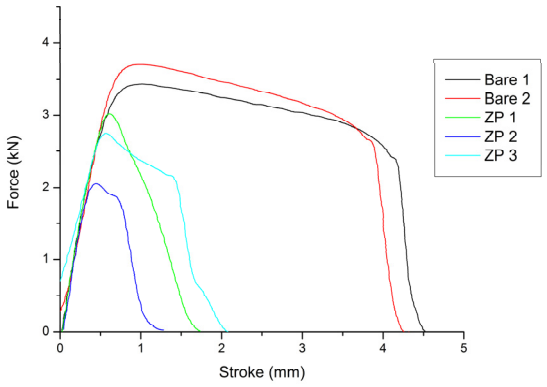

Figure 44: Hot tensile test of ZP and bare samples tested at 800°C and 1 mm/s strain rate illustrating the moderate reproducibility

4.3.1 Influence of temperature

The influence of testing temperature on the LME effects was observed via tensile tests. Figure 45 displays the Force-Stroke curves of zinc painted and bare samples in a temperature range of 600–1100°C carried out with a constant strain rate of 1 mm/s.

The reduction of mechanical properties by zinc comes into play at a temperature of 700°C, finds its maximum at 800°C and starts then a progressive recovery until 1100°C. In those specific conditions at 600°C as well as at 1100°C no noteworthy influence of LME can be distinguished.

a) b)

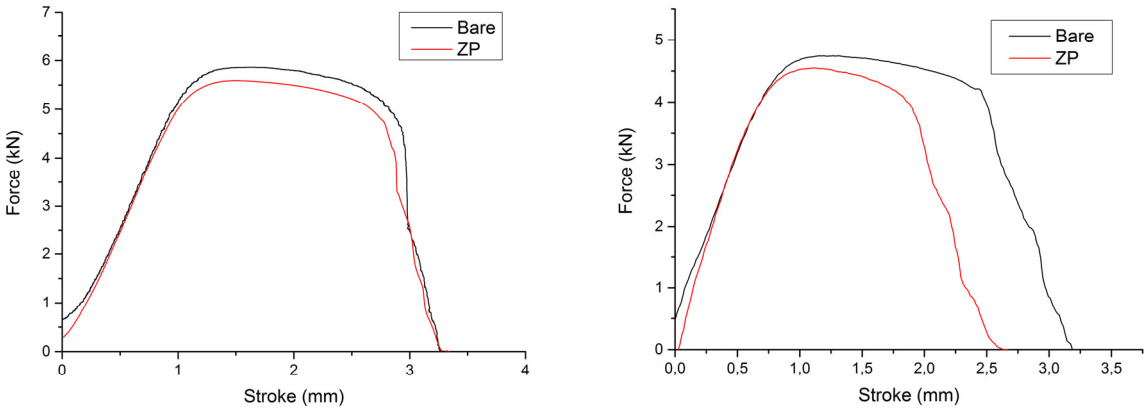

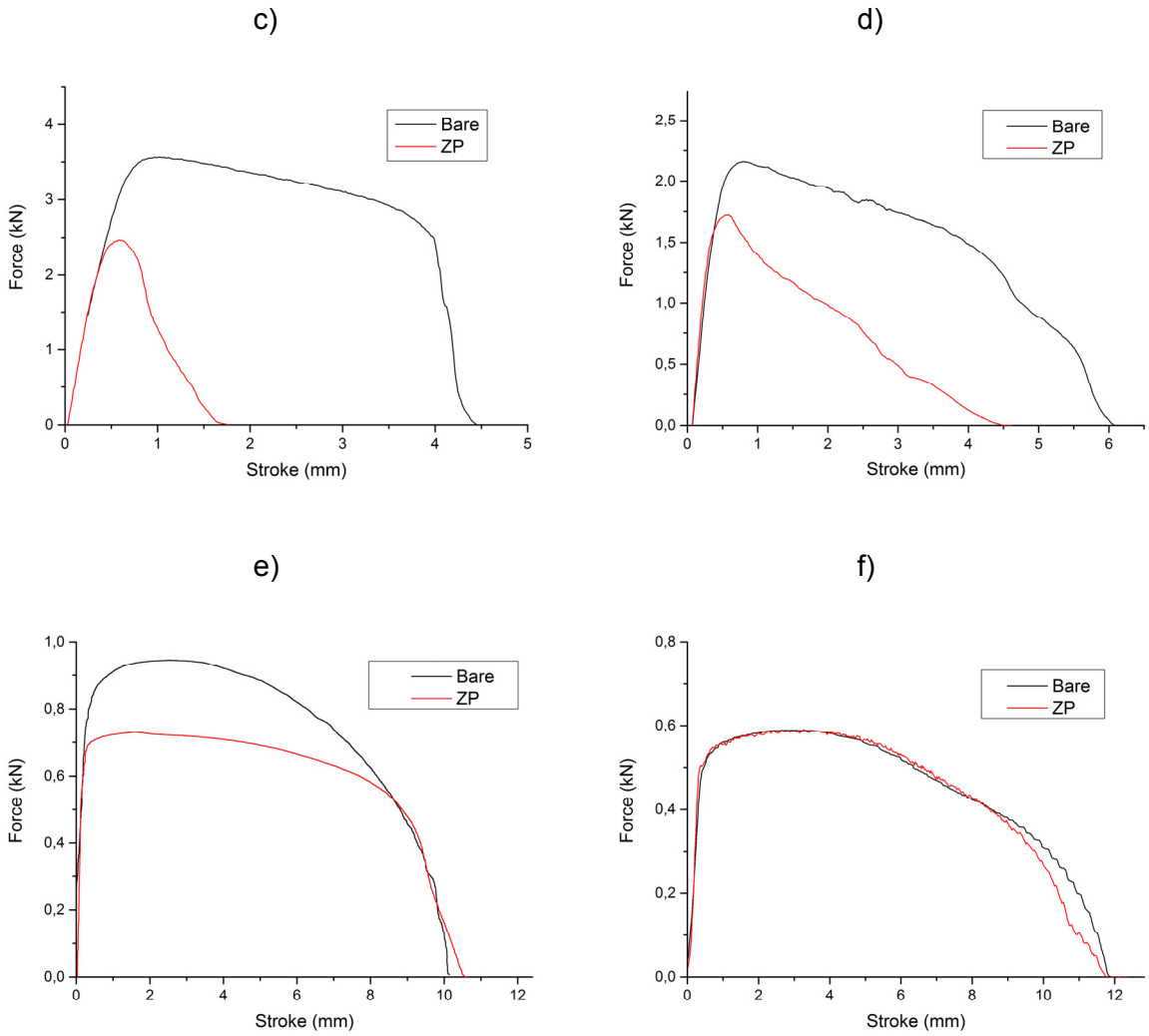

Figure 45: Force-Stroke curves of 301M steel samples coated with zinc-rich paint with 1 mm/s strain rate at: a) 600°C b) 700°C c) 800°C d) 900°C e) 1000°C f) 1100°C

As described in chapter 3.5 the reduction of fracture energy has been used for determining the severity of embrittlement. The scattering of the performed tests was estimated to be around 10% which led to the definition of LME starting from a decrease of fracture energy of more than 10%.

Figure 46 shows the reduction of fracture energy of ZP samples compared to bare ones for different temperatures. Again, the temperature range where LME occurs is confirmed ranging from 620–1010°C. In the most severe conditions at 800°C with 1 mm/s strain rate the fracture energy of the ZP sample is reduced by 82%.

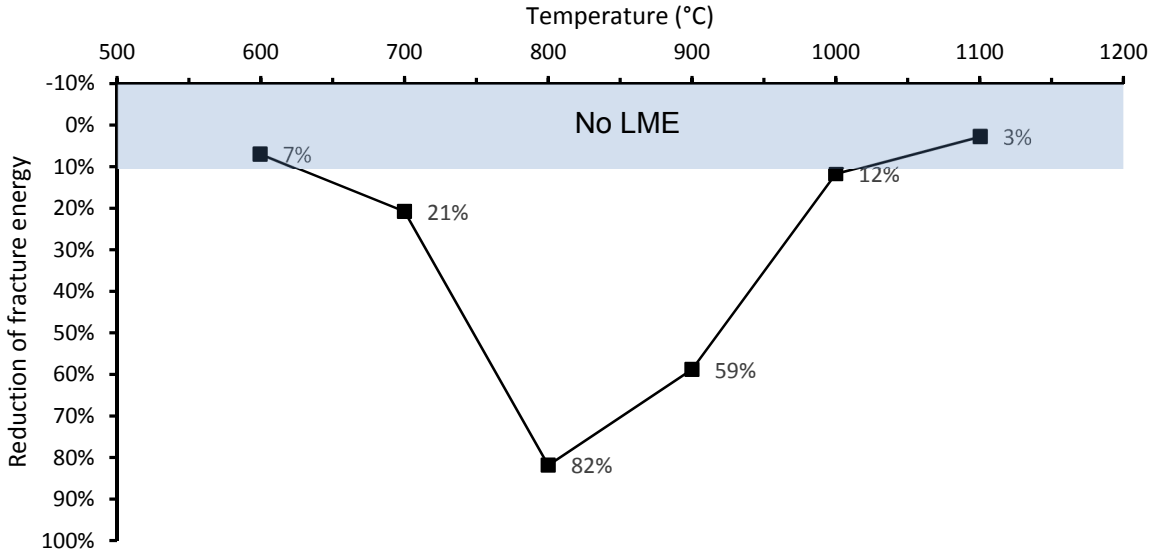

Figure 46: Fracture energy reduction in respect to testing temperature for 301M coated with zinc-rich paint for 1 mm/s strain rate

Figure 47 gives information about the temperature zone where the samples ruptured. In general a bare sample tensile tested at increased temperature with the Gleeble® simulator will most likely rupture in the centre. This is explained by the temperature distribution having its maximum there and therefore inducing a minimum of mechanical strength.
It is worth reminding that the sample was virtually divided into 3 different temperature zones. Those zones are displayed in Figure 47a) and further described in 3.3.2.1.

Between 600 and 700°C as well as at 1000 and 1100°C the samples failed in the centre area where the sample had the highest temperature.

At temperatures between 800 and 900°C the samples tend to fail outside their area of highest temperature. This suggests for the test at 800°C that there must be even greater LME initiated decrease of strength and ductility at lower temperatures than 800°C, otherwise its rupture would take place in the centre. For the samples tested at 900°C it confirms that embrittlement exceeded its maximum at this temperature and the higher temperature leads to a decrease of LME effects.

The reason for the samples at 1000°C failing again in the centre might be based on the significant decrease of ultimate tensile strength between 900 and 1000°C displayed in Figure 42, additionally to the recovery of LME effects above 1000°C.

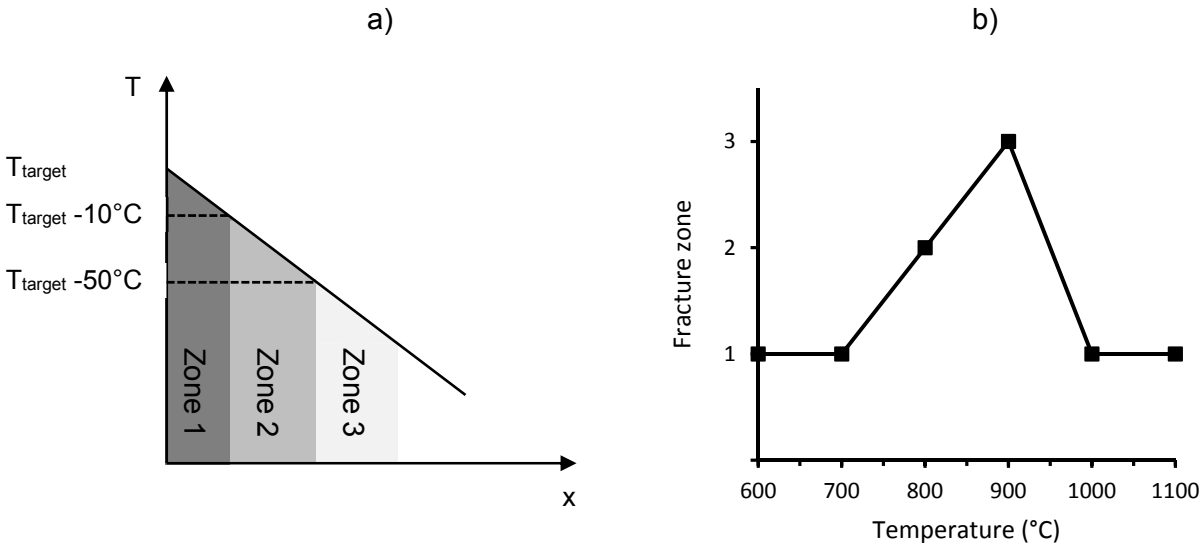

Figure 47: a) Reminder of different temperature zones within the sample b) Zones of fracture for zinc-painted 301M steel samples tested at different temperatures with 1 mm/s strain rate

4.3.2 Influence of strain rate

The influence of strain rate was observed by comparing tests of bare and zinc-painted samples of 301M type of steel at same temperatures.

Figure 48 displays the results of hot tensile tests at 800°C carried out with 1 mm/s and 100 mm/s strain rates. Apart from the change in behaviour of the bare sample at higher strain rate it is clearly noticeable that the severity of liquid metal embrittlement decreases significantly. The decrease of maximum force of the ZP sample and also the reduction of elongation experiences a serious recovery at higher strain rate.

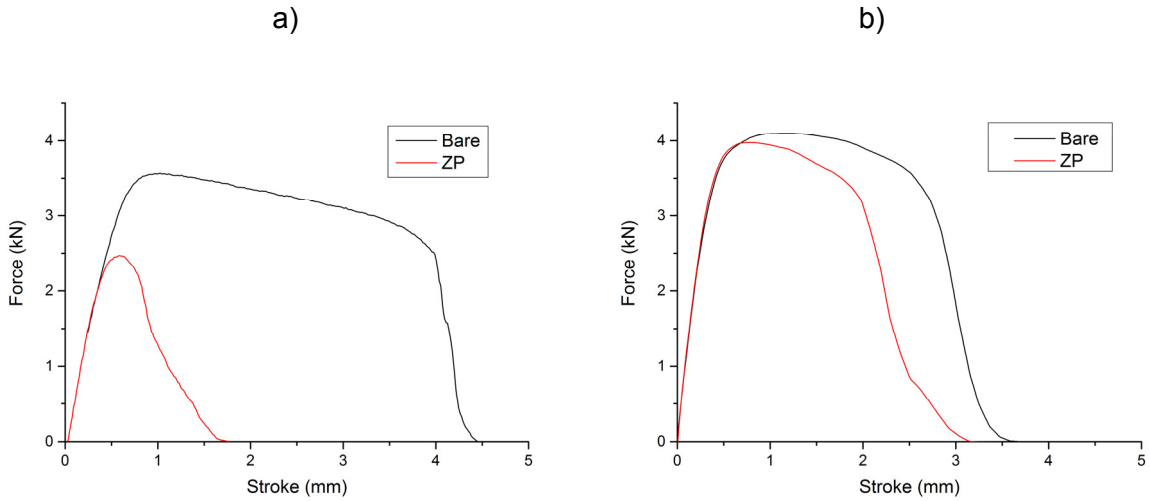

Figure 48: Force-Stroke curves of 301M steel coated with zinc-rich paint at 800°C: a) with 1 mm/s strain rate b) with 100 mm/s strain rate

Figure 49 presents the reduction of fracture energy of zinc-painted samples for different temperatures again, with a strain rate of 1 and 100 mm/s. In comparison one can clearly see that the severity over the whole temperature range decreased with the higher strain rate. Also the width of the ductility trough got narrower as LME starts very slowly at 700°C and no more LME occurs at 970°C. The maximum reduction of fracture energy has changed from 800°C for 1 mm/s strain rate to 900°C for 100 mm/s. These results are contradictorily to results found in literature where the opposite trend was observed by Beal [3] and Fernandes et al [26]. In both cases increasing the strain rate led to more severe embrittlement.

For comparative reasons values obtained in a previous project were added to this chart. The dashed curve was observed in very similar conditions when samples with the same geometry made of the same 301M steel were coated with zinc-rich paint on one side and tested with a constant strain rate of 16 mm/s in a thermo-mechanical simulator. The shape of this curve is likewise the one obtained with 100 mm/s strain rate but has an offset towards higher reduction of energy. Also at 600°C strong embrittlement with a fracture energy reduction of 30% has been observed. This is contradictory to the results found during this work. More tests would be necessary to confirm the curves for 16 mm/s strain rate.

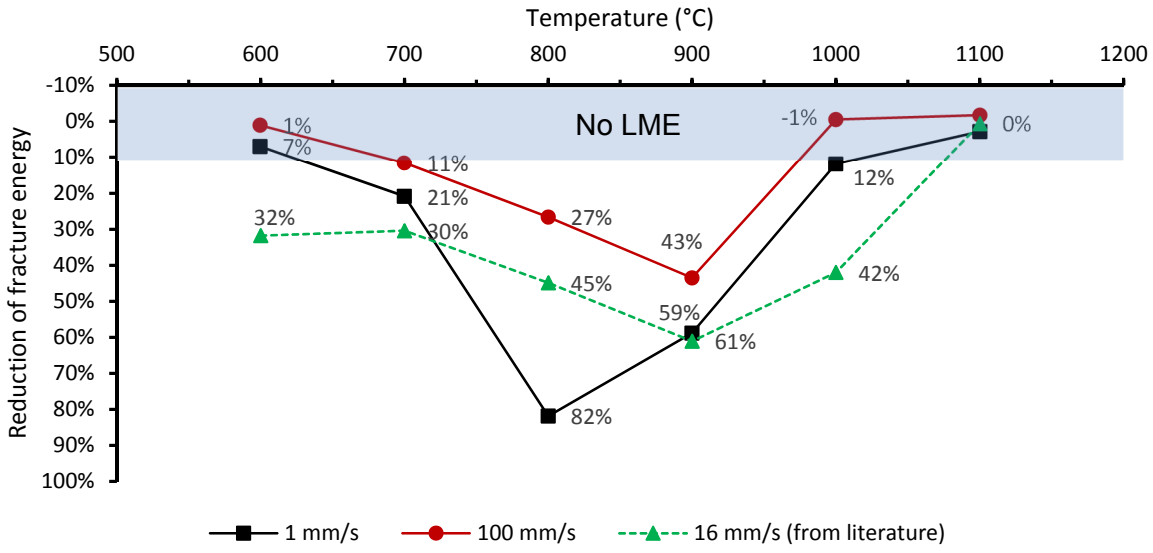

Figure 49: Fracture energy reduction in respect to testing temperature for 301M coated with zinc-rich paint for 1, 16 and 100 mm/s strain rate. Data for 16 mm/s strain rate from literature [1]

4.3.3 Influence of time of contact between base material and liquid metal

The influence of time of contact between base material and liquid metal on the effect of LME was studied with two test series, executed with different strain rates.

Figure 50a) presents the results from hot tensile tests at 800°C with 1 mm/s strain rate and holding times between 0 and 40 s. The Force-Stroke diagram reveals the increase of maximum force and stroke with longer holding times. While at 0 s holding the effects of LME are drastic, after an applied holding time of around 40 s the behaviour does not differ much from a bare sample that was tensile tested after a pre-exposure time of 50s.

In Figure 50b) the Force-Stroke curves of tests with apllied pre-exposure time with a strain rate of 100 mm/s are shown. Again, the mechanical behaviour follows a recovery process where after an applied holding time of approx. 20 s the zinc-painted samples show the same behaviour as the bare ones.

These results go along with some reports listed in the literature review where the same trend was observed [3], [32]. Others found no influence of preliminary exposure on mechanical properties or even negative influence where preliminary wetting of the grain boundaries was a requirement for LME to take place [24], [30], [33].

a) b)

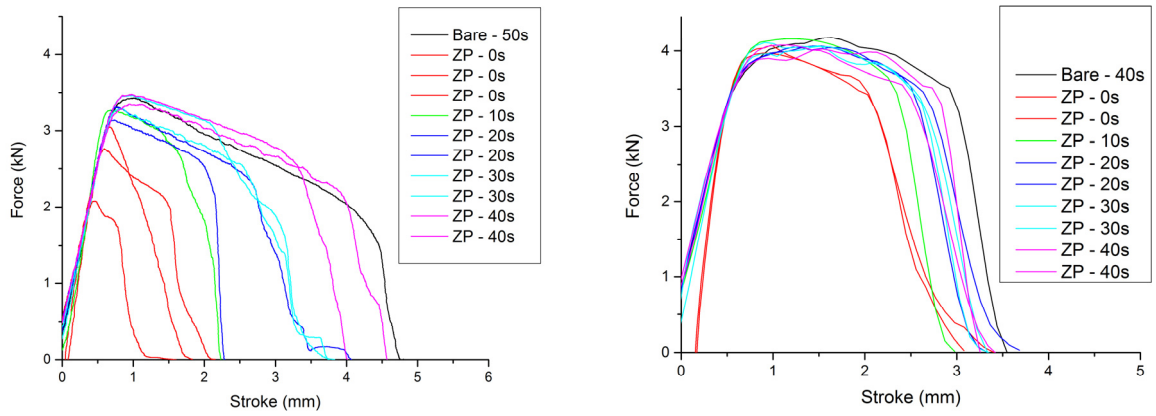

Figure 50: Force-Stroke curves of 301M steel coated with zinc-rich paint at 800°C for different holding times: a) with 1 mm/s strain rate b) with 100 mm/s strain rate

Figure 51 illustrates the reduction of fracture energy for the above mentioned tests over pre-exposure time. For both strain rates an approximately linear recovery of fracture energy over time is found. While the higher strain rate shows no more signs of LME after 20 s of holding time, the more severe starting condition of the lower strain rate led to a full recovery of fracture energy after a holding time of little over 40 s.

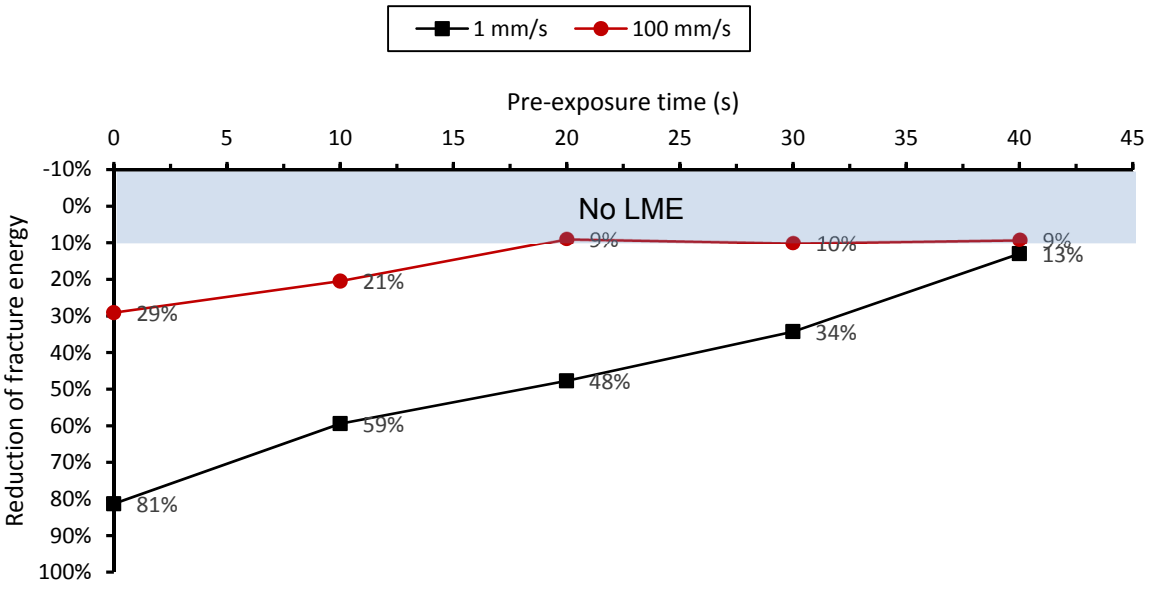

Figure 51: Fracture energy reduction of 301M coated with zinc-rich paint at 800°C for 1 mm/s and 100 mm/s strain rate

4.3.4 Influence of coating method

The influence of coating method was investigated by testing samples with 3 different coatings: zinc painting (>40 µm thickness), EG2.5 (~2.5 µm thickness) and EG10 (~10 µm thickness).

Figure 52a) shows the Force-Stroke curves of samples with different coatings tested at 800°C with 100 mm/s strain rate. The tested samples show no significant influence of coating method in their results. The reduction of fracture energy of samples tested with the 3 different coatings lies within the variation of those tests.

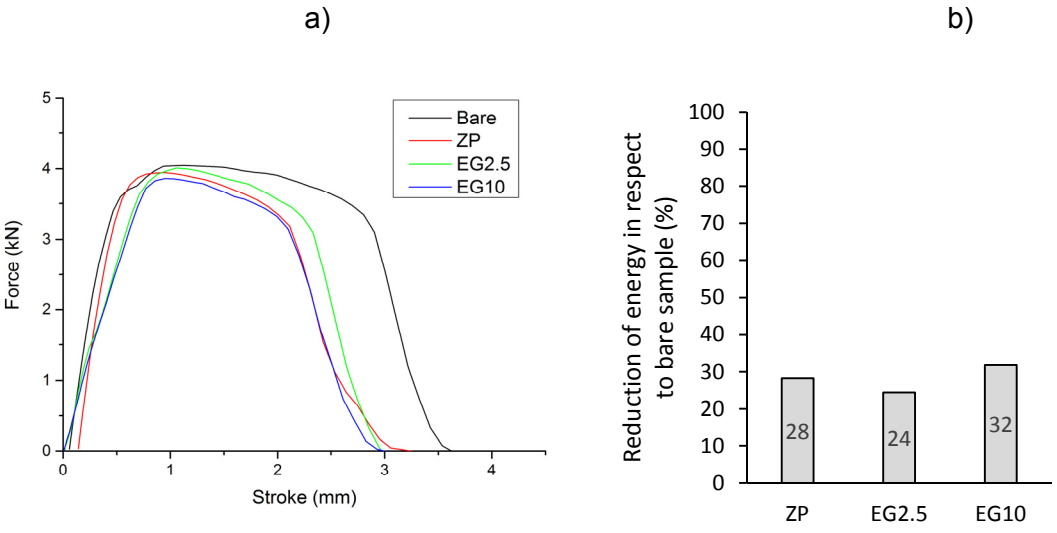

Figure 52: Influence of coating method on LME: a) Force-Stroke curves of samples tested with different coatings at 800°C with 100 mm/s strain rate b) Reduction of fracture energy of samples shown in a)

4.3.5 Influence of available amount of liquid metal

In Figure 53a) the Force-Stroke curves for samples electro-galvanised with 2.5 µm of zinc and for different pre-exposure times are displayed. The tests that were carried out with an applied pre-exposure time of 5 s lead to a successful recovery of mechanical properties. After a time span of 20 s no more influence of the zinc layer on the mechanical behaviour was observed.

In b) the same tests were carried out with samples containing a zinc layer of 10 µm thickness. In contrast to other tests performed with holding time, here the holding time of 10 s led to heavier embrittlement. Clearly the maximum force as well as the elongation to rupture are reduced from the sample tested without holding time. When extending the holding time this trend is reversed and the sample recovers more and more until the mechanical properties of the bare sample is met again after 40s holding time.

a) b)

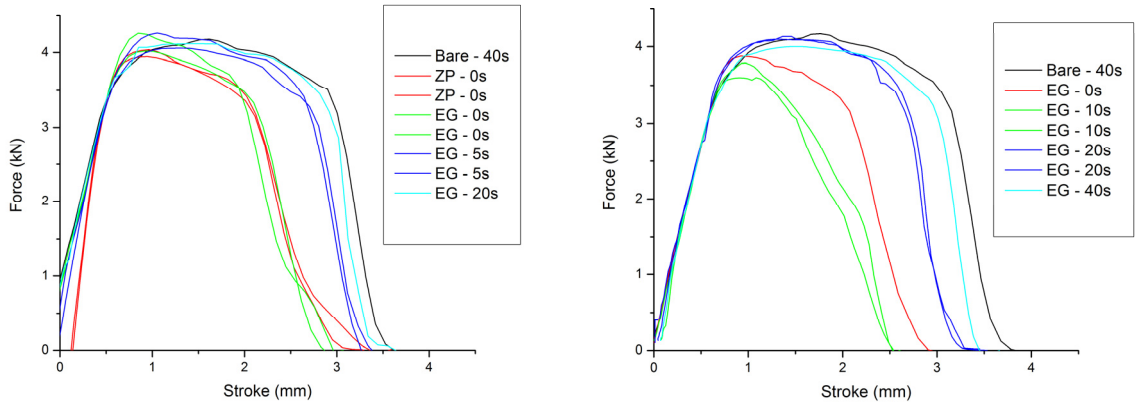

Figure 53: Force-Stroke curves obtained at 800°C with 100 mm/s strain rate and different holding times: a) of samples electro-galvanised with 2.5 µm of pure zinc b) of samples electro-galvanised with 10 µm of pure zinc

Figure 54 shows the reduction of fracture energy of those samples described above. It is clear that the lower amount of zinc on the EG2.5 samples leads to a faster recovery which is observed after less than 5 s. Both the 10 µm EG and the ZP samples recover after an applied holding time of 20 s.

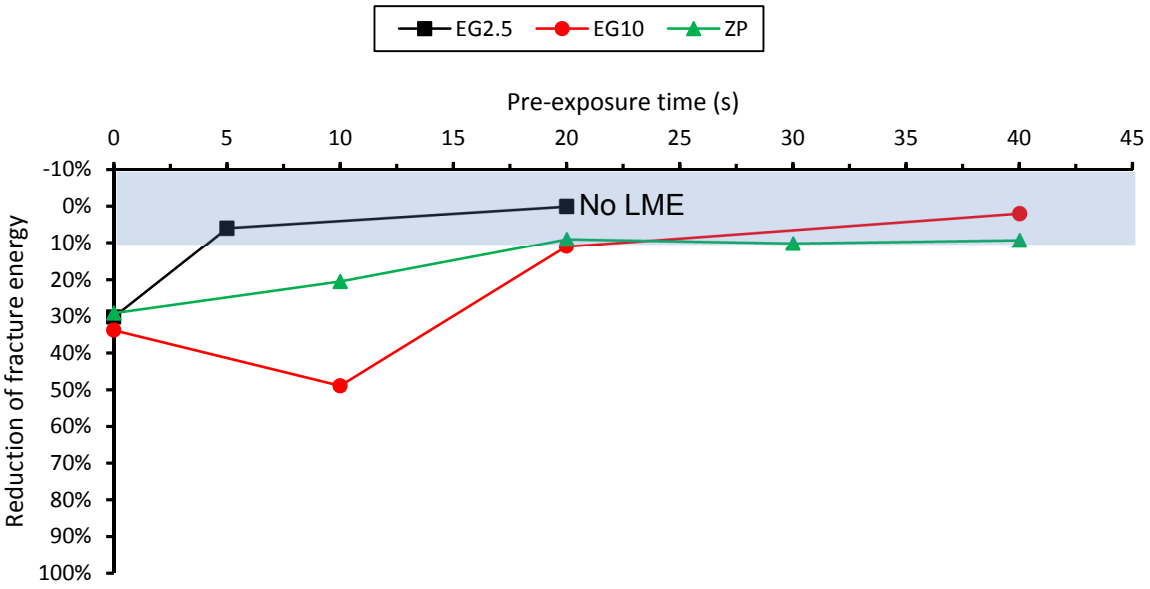

Figure 54: Fracture energy reduction of 301M at 800°C for 100 mm/s strain rate for samples coated with different coating thickness

4.3.6 Interrupted tests

Some additional tests have been performed in order to find the stage of crack initiation in a subsequent microscopy investigation. Figure 55a) shows the Force-Stroke curves of those tests where the values in the legend represent the maximum stroke level that was targeted at the Gleeble® machine. The curve of a bare sample is added as well for comparative reasons.

Afterwards those pre-tensioned samples underwent room temperature tensile tests as presented in Figure 55b). A significant effect of pre-straining could be observed for sample ZP-0.7 and ZP-1.5. However, the expected tendency of higher pre-straining leading to more severe cracks and therefore lower values of elongation in the room temperature test could not be proved; the sample with second lowest pre-tension value ruptured the earliest in the subsequent tensile test; the sample with 1.5 mm pre-straining showed a very similar behaviour as the one pre-strained to a value of 0.5 mm.
An explanation for it could be found in the testing procedure when after reaching the desired stroke level the sample is water quenched. The rapid temperature decrease leads to a contraction of the material, resulting in an uncontrolled load situation that cannot be compensated fast enough by the machine.

The curves of the bare sample are again added for comparative reasons. It would have been interesting to perform the same interrupted tests on bare samples to have a valid reference behaviour.

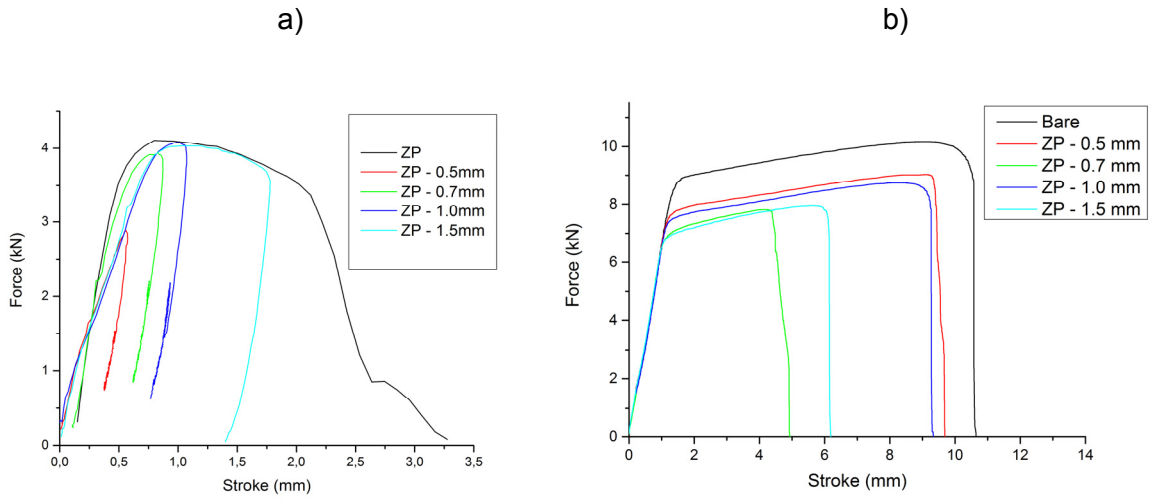

Figure 55: a) Interrupted tests with ZP samples at 800°C and 100 mm/s strain rate b) room temperature tensile test with pre-strained samples

Light optical microscopy investigations of those samples revealed that crack initiation started with a minimum strain of 0.7 mm. A further trend between pre-strain level and systematic crack occurrence could not be established. More tests would be necessary.

4.3.7 Approximation of resistance spot welding

Another thermo-mechanical cycle was tested with the aim of connecting the laboratory tests to the real RSW process. The results of these tests are displayed in Figure 56.

In Figure 56a) the results of a sample that underwent the RSW test cycle with a target temperature of 700°C are shown. At first, a tensile force of 3 kN is applied linearly within 5 s. Afterwards the sample is heated with 80°C.s^{-1} to its target temperature. During this time span the thermal expansion leads to a decrease of force, which should be compensated by the Gleeble® simulator but still leads to a slight decrease of force to roughly 2.8 kN while heating. After reaching target temperature the force and temperature are applied for 1 s additionally and afterwards the sample is relaxed and cooled down in air atmosphere.

In Figure 56b) results of different ZP and bare samples with target temperatures of 700, 800 and 900°C are shown while the force control mode was always setup to maintain a tensile load of 3 kN.

As one can clearly see this level could roughly be held at 700°C but higher temperatures resulted in a decrease of force, due to lower yield strength of the sample. One trend worth mentioning is that for all testing temperatures the bare samples show a yield strength which results in lower total elongation compared to the ZP ones.

a) b)

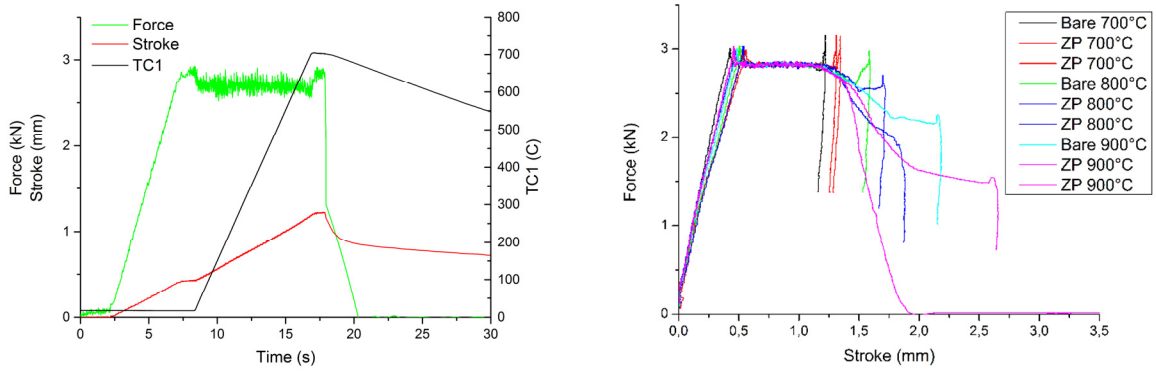

Figure 56: a) Force, stroke, temperature as a function of time displayed for a bare sample with a target temperature of 700°C b) Force-Stroke curves of RSW tests with 3 kN pre-tension and 80°C/s heating rate

4.4 Towards an explanation for mechanical behaviour

With the aim of finding explanations for the mechanisms behind LME, different microscopy investigations were performed.

This section discusses at first the different types of fracture surfaces found on the tested samples and later gives an overview of the data gained from light optical microscopy. Afterwards samples that underwent the RSW test cycle are observed.

Finally the coating layer and its surrounding area are studied and further investigations of cracks are presented and described.

4.4.1 SEM investigation of fracture surfaces

The microscopy investigation of fracture surfaces reveals some details related to the mechanical behaviour during hot tensile tests.
At first, a bare sample tested at 800°C is studied in order to get a reference for the usual failure mode of this material. Afterwards a zinc-painted sample tested at 800°C with different strain rates is investigated.

4.4.1.1 Bare sample at 800°C 1mm/s strain rate

For the bare sample of 301M Figure 57a) gives an overview of an even fracture surface and shows signs of necking as it is typical for ductile failure during tensile tests. Figure 57b) shows the highlighted area of Figure 57a) with higher magnification. It reveals a surface typical for ductile failure of this type of steel characterised by dimples of about 5 µm distributed over the whole area.

a) b)

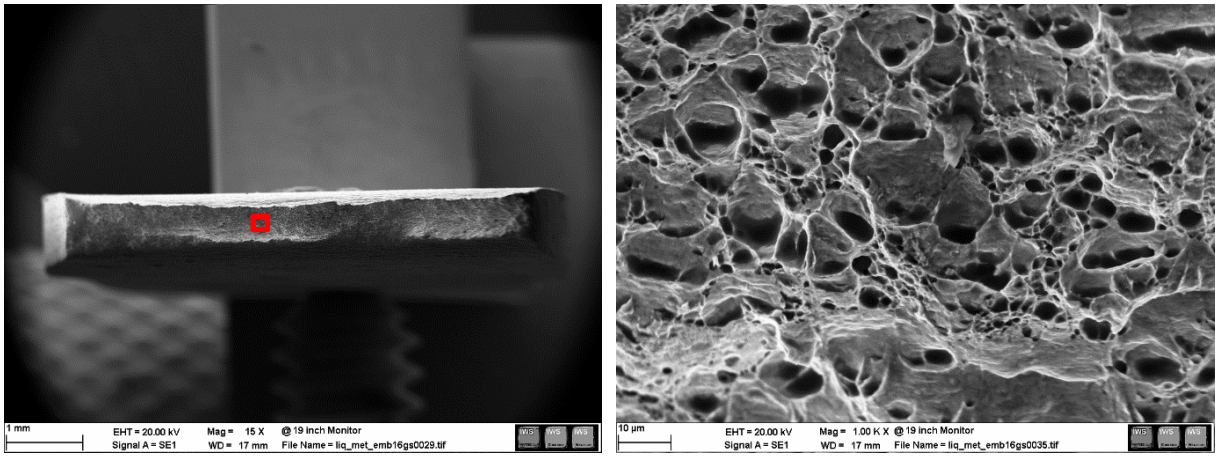

Figure 57: Fracture surface of 301M steel tensile tested at 800°C with 1 mm/s strain rate: a) Overview of fracture surface with rectangle showing the magnified area of b): higher magnification of fracture surface revealing dimples all over the area

4.4.1.2 ZP sample at 800°C and 1mm/s strain rate

The decrease of elongation can be explained by the evolution of the fracture surface that is initiated at the side of the zinc layer of the specimen.

In Figure 58a) an overview of the fracture surface is given. Two different areas of fracture mode divided by a clear line are visible throughout the whole width of the sample. Compared to the fracture surface of the bare specimen in Figure 57a) the very limited amount of necking is noticeable indicating a brittle failure mode. Figure 58b) shows the highlighted area of Figure 58a). It displays the border region of the two different zones of fracture surface in higher magnification. Figure 58c) displays an area of intergranular fracture typical for a brittle failure mode which is present all over the upper part of the fracture surface starting at the zinc layer with a depth of around 200–900 µm. The lower part features the same structure as the bare specimen which failed with ductile behaviour.

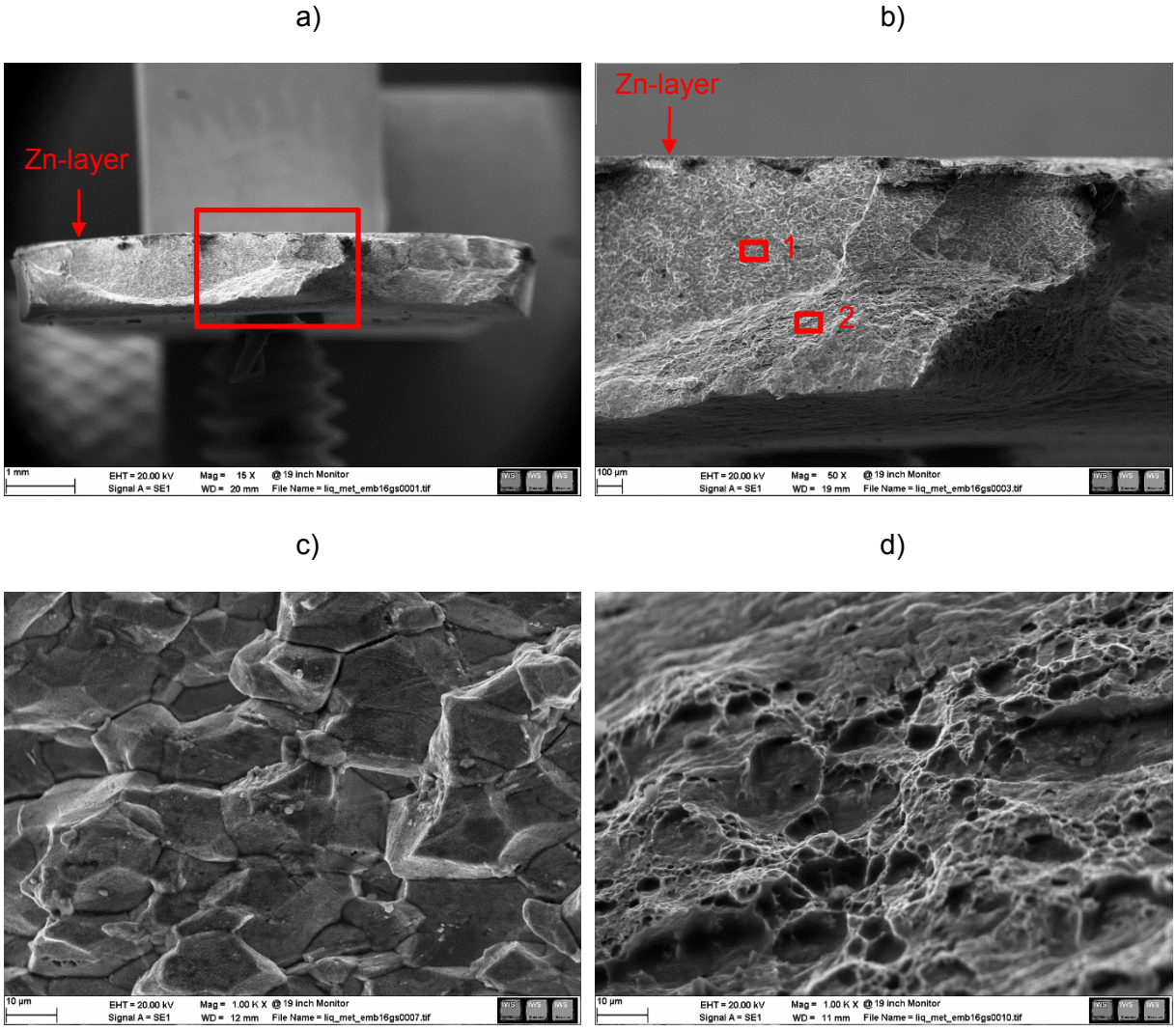

Figure 58: Fracture surface of 301M steel coated with zinc-rich paint and tensile tested at 800°C with 1 mm/s strain rate: Overview of fracture surface with rectangle showing the magnified area of b): borderline of two different fracture zones with rectangle 1 showing the brittle fracture mode displayed in c) and rectangle 2 showing dimples of the ductile fracture mode displayed in d)

It is worth repeating that a zinc layer of around 40–100 µm on only one side was applied to the sample.

The impact of the zinc coating on the 301M steel in those particular testing conditions must be stated as very high. The total elongation was reduced by roughly two thirds and also the UTS experienced a serious reduction. Zinc tends to change the failure mode of the material from normally ductile to brittle behaviour over major parts of the cross section of the sample.

4.4.1.3 ZP sample at 800°C and 100 mm/s strain rate

In Figure 59 the fracture surface of a ZP sample also tested at 800°C but with a much higher strain rate of 100 mm/s is displayed. It exposes the reason for the lower degree of reduction

of the fracture energy in comparison to the samples tested with 1 mm/s strain rate. This can be explained by the amount of brittle area in the fracture surface that is significantly lower here, than at 1 mm/s. As Figure 59b) reveals only a depth of around 150 µm is embrittled while the test with 1 mm/s strain rate experiences embrittlement to a much further depth of up to 900 µm. This could be addressed to the significantly lower time till fracture of, resulting from the very high strain rate. Once the tensile load is applied it only takes hundreds of a second till fracture occurs which is also the time span were LME mechanisms take place.

a) b)

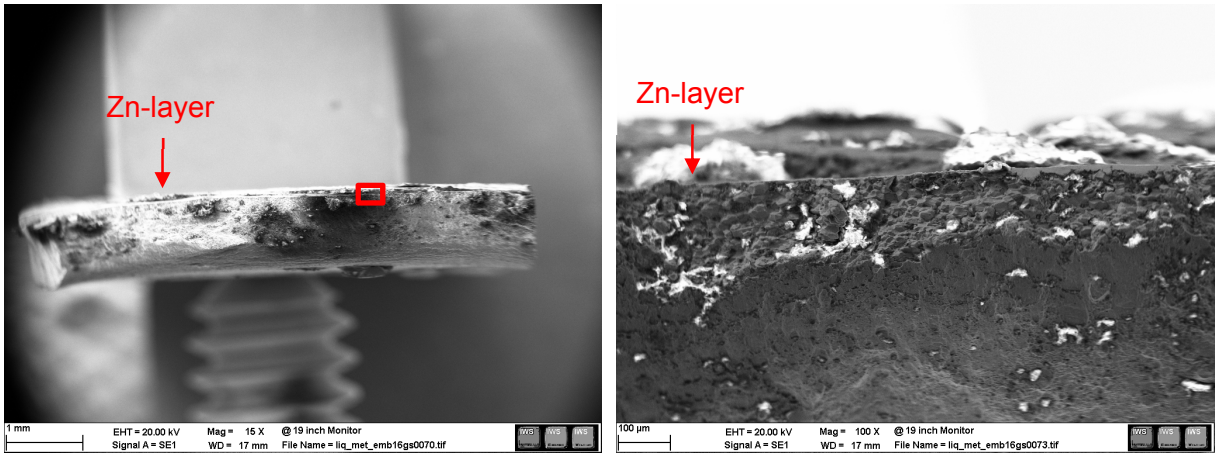

Figure 59: Fracture surface of ZP sample tensile tested at 800°C with 100 mm/s strain rate: a) whole fracture surface b) magnified area with visible borderline between ductile and brittle part

4.4.1.4 Summary

The investigation of fracture surfaces revealed a brittle cracking mode starting from the zinc layer of the samples and reaching far into the base material. This brittle fracture zone explains the significant reduction of elongation to rupture of the ZP samples.
The higher strain rate led to a decrease of the width of the brittle zone clarifying the less severe embrittlement found in these conditions.

4.4.2 Investigation of longitudinal section / quantitative LOM data

Figure 60 shows the longitudinal section of two zinc-painted samples tested at 800°C with 1 mm/s strain rate. In a) the overview of the fracture zone and some cracks is presented for a sample tested without any holding time. Additionally to the crack that led to rupture 3 more large cracks with a length up to around 500 µm are visible.

Image b) shows a sample with same testing conditions but after an applied holding time of 40 seconds. The zone of fracture indicates clear signs of deformation before rupture which accords with the mechanical behaviour observed after successful recovery. The amount of cracks is increased when compared to a) but the length decreased drastically.

a) b)

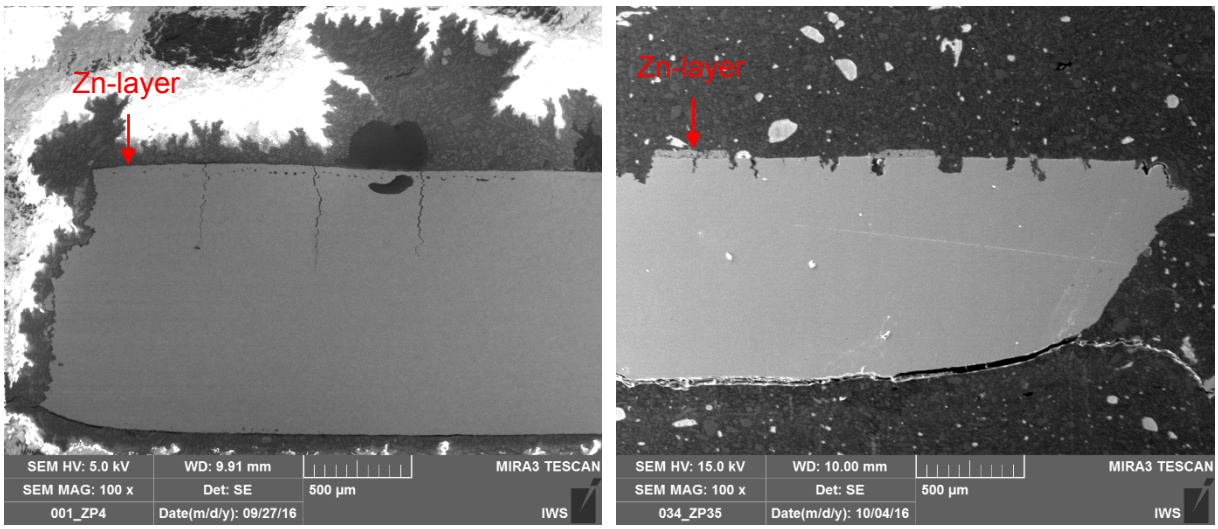

Figure 60: SEM image of longitudinal section of ZP sample tested at 800°C with 1 mm/s strain rate: a) without holding time b) after 40 s holding time

Figure 61 displays the data gained from investigating the samples with a light optical microscope. As described in chapter 3.3.2.1 the tensile sample was divided into 3 different zones corresponding to a certain temperature range. Here the data for all cracks on the sample (all 3 zones), for cracks in the homogeneous temperature zone (Zone 1) and for cracks in the fracture zone (either Zone1, Zone 2 or Zone 3) are displayed. The fracture zone means the one zone out of all three defined ones, in which the sample ruptured. The zones of rupture for the corresponding temperatures are displayed in Figure 47.
The quantification of crack geometry data could not exactly explain the mechanical properties observed during testing, nevertheless some trends and interesting information can be stated.

As shown in a) up to 133 cracks have been found in one longitudinal section of one sample, tested at 900°C. The number of cracks in the respective fracture zones show similarities to the temperature ductility trough, though the maximum here is shifted from 800 to 900°C. At temperatures higher than 800°C many cracks appear outside the fracture area.
At upper and lower end of the testing temperature very few cracks appeared which corresponds to the ductile mechanical behaviour of the sample.

A look into the chart of total crack length in b) shows a similar behaviour as a). The maximum of both curves is at 900°C and at upper and lower end the crack length is comparatively very low. It is noteworthy that one sample contains up to 25 mm of cracks in one longitudinal section while the thickness of the sample is around 1.2 mm. This figure gives an idea of how serious the appearance of cracks is.

The average crack length is presented in c) without further description.

In d) the maximum depth of cracks is displayed. When comparing the value for the fracture zone (green curve) to the reduction of fracture energy over temperature / temperature ductility trough (see Figure 46) a clear similarity can be found.

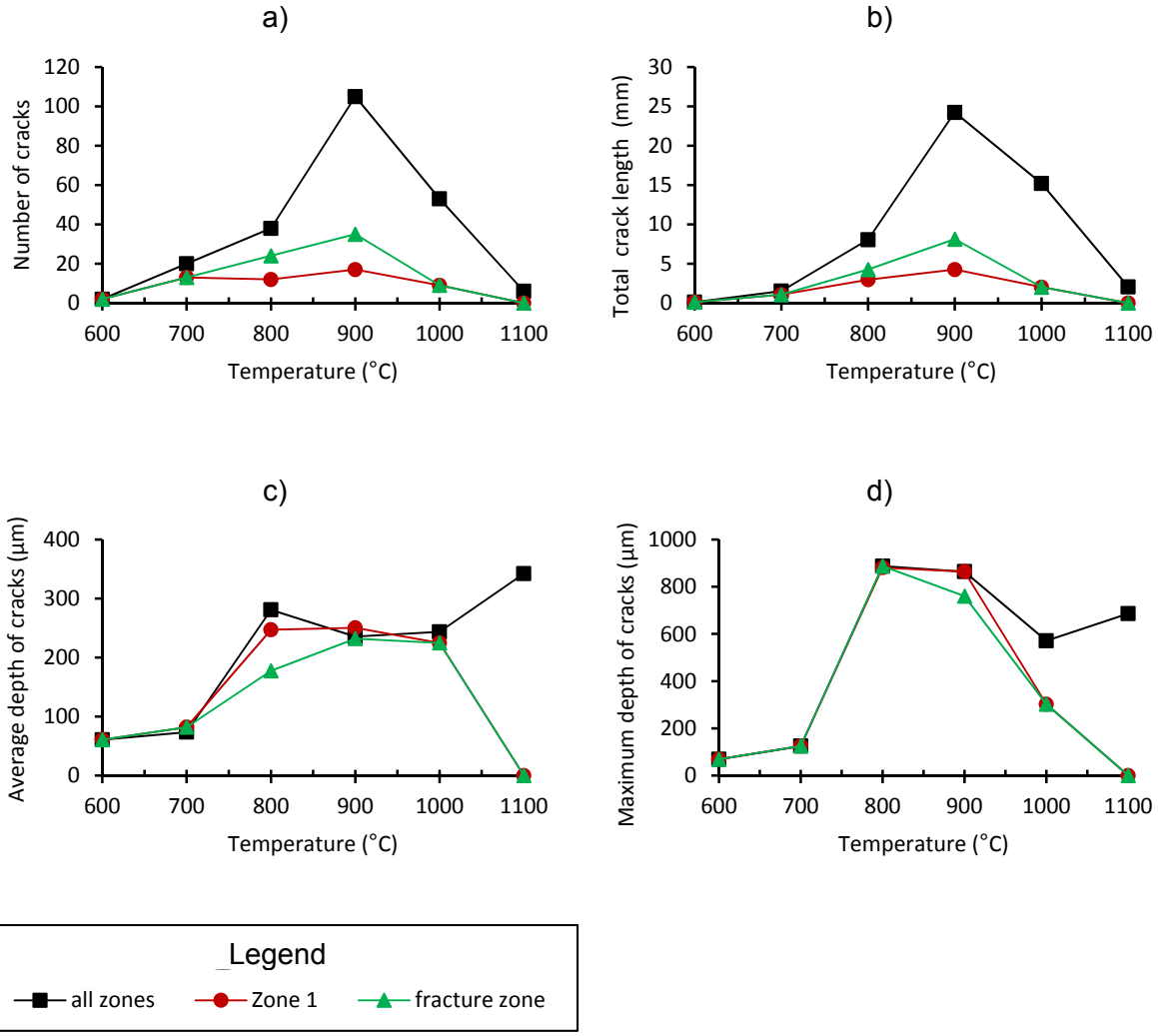

Figure 61: Summary of light microscopy data of hot tensile test of zinc-coated 301M steel at different temperatures with 1 mm/s strain rate: a) Number of cracks b) Total length of cracks c) Average depth of cracks d) Maximum depth of cracks

Figure 62 presents histograms of crack lengths for the above mentioned samples. The black bars indicate the total amount of cracks whereas the red ones only count the cracks in the homogeneous temperature zone in the centre part of the sample.

At 600°C only a few small cracks up to maximum 100 µm were found. With increasing temperature, the diagram for 700°C shows a higher amount of total cracks with a few of those being up to 200 µm.

At a testing temperature of 800°C the amount of cracks decreases, though cracks of over 400 µm of depth were found. The highest number of cracks was found on the sample tested at

900°C which also has the highest number of >400 µm cracks, indicating that the embrittlement might be the worst in these conditions. With a testing temperature of 1000°C the amount of cracks decreases significantly and at 1100°C only a few cracks outside of the homogeneous temperature zone (Zone 1) were found.

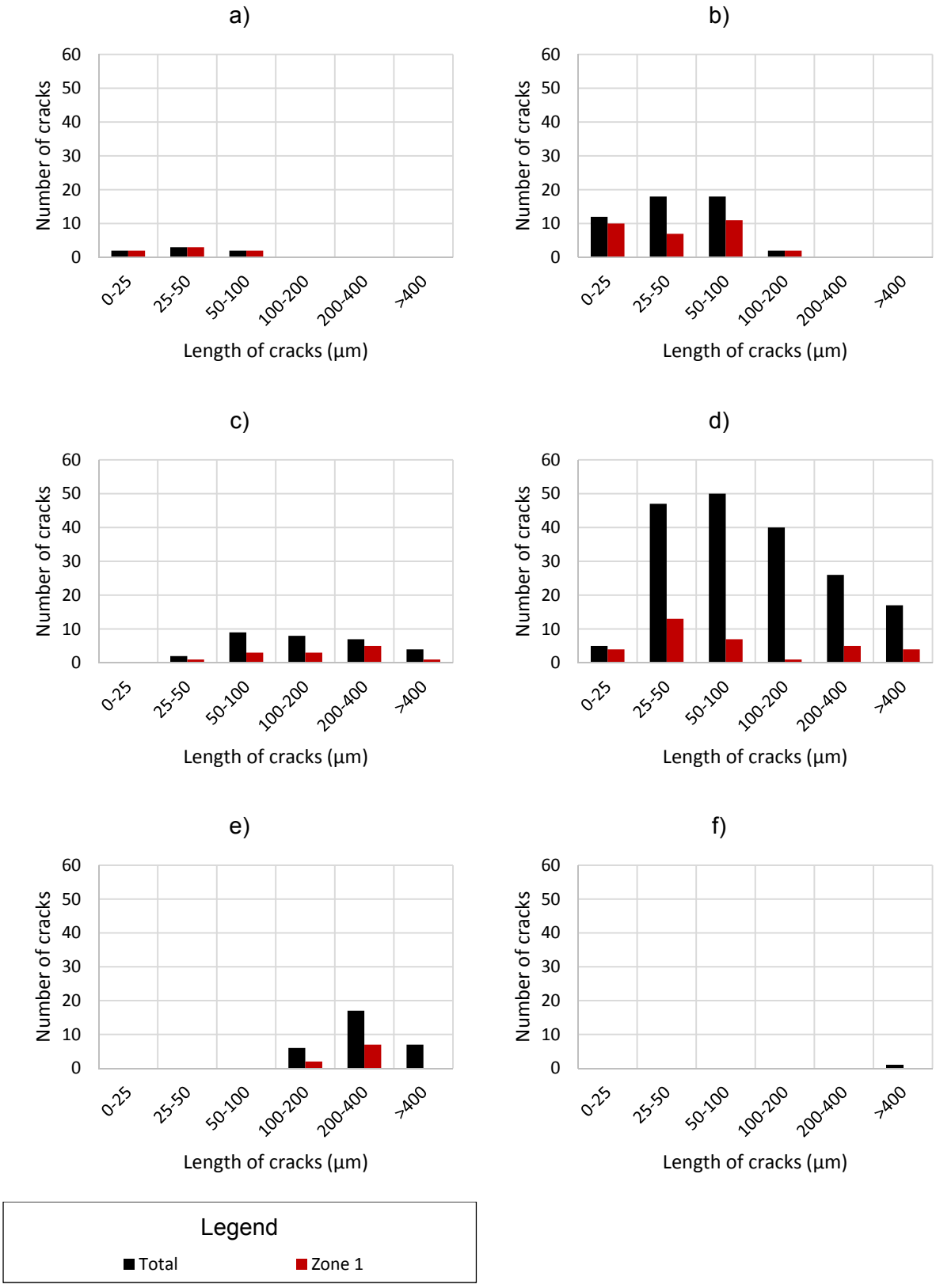

Figure 62: Histogram of crack lengths at tested at: a) 600°C b) 700°C c) 800°C d) 900°C e) 1000°C f) 1100°C

In Figure 63 the crack data from a test series of zinc-painted samples with different holding times is displayed. The black curves represent the data of cracks on the whole sample (in all 3 temperature zones).

The amount of cracks in a) shows an increase of cracks with longer holding times but a decrease of average crack depth (c)) and maximum crack depth(d)) compared to the sample without holding.

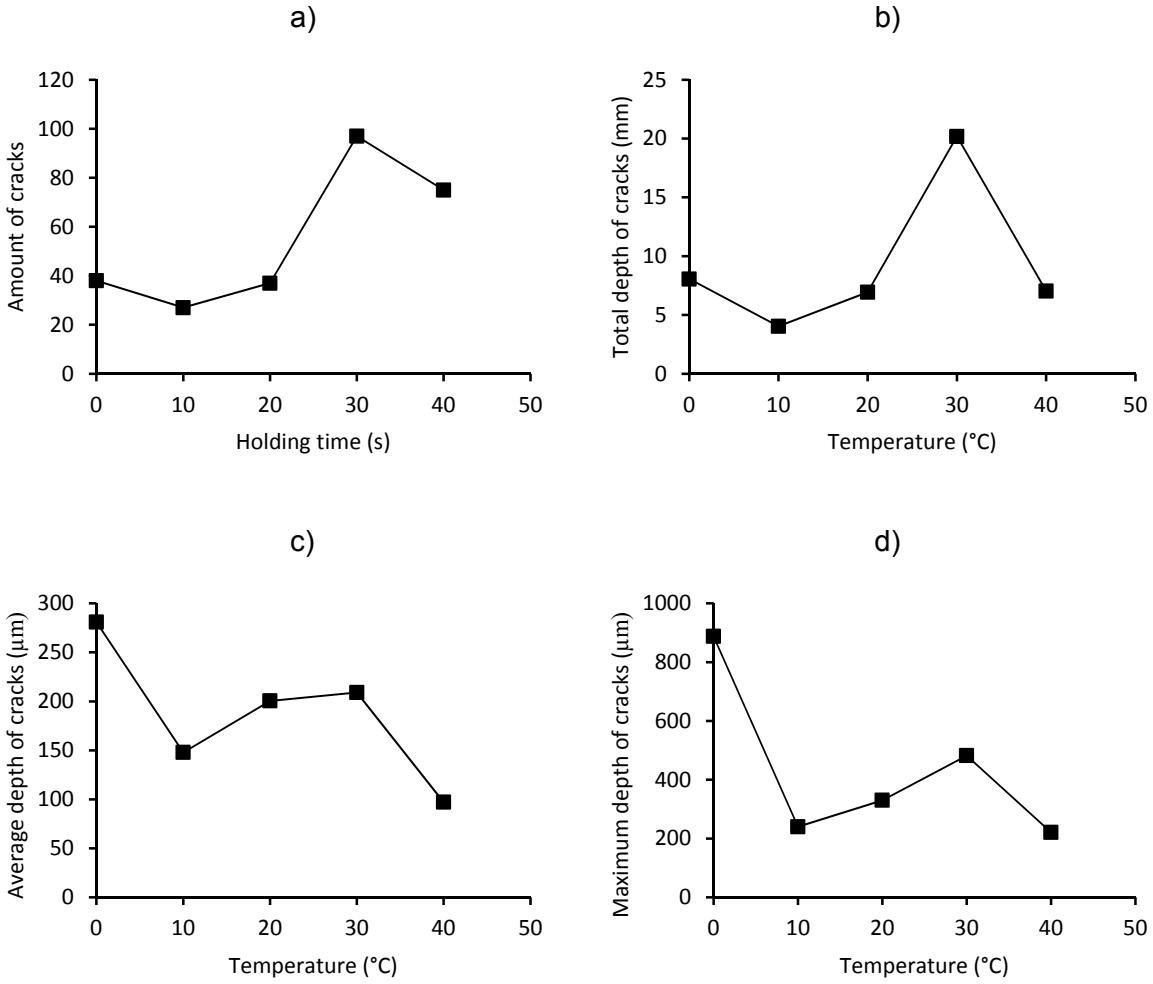

Figure 63: Summary of light microscopy data of hot tensile test of zinc-coated 301M steel at 800°C with 1 mm/s strain rate: a) Number of cracks b) Total depth of cracks c) Average depth of cracks d) Maximum depth of cracks

4.4.3 LOM investigation of RSW simulation test samples

Samples that underwent the RSW simulation test were observed by means of a stereo microscope. The centre parts of 3 different samples are shown in Figure 64 which all went through the RSW simulation test with target temperatures of 700, 800 and 900°C.
In a) the sample heated to 700°C is displayed. It did not reveal any cracks on the surface but only shallow scratches which were most likely created through spalling of the zinc paint during deformation.
The sample heated to 800°C is shown in b). One can clearly see the appearance of cracks which also lead to a rupture of the sample.
Even more cracks are visible in c) which shows the sample heated to 900°C.

The testing procedure of the RSW simulation clearly proved that changing the sequence of thermal and mechanical load still resulted in LME occurrence when reaching the right temperature. With improvement through higher heating rates, laboratory simulations could get even closer to the practical RSW process.

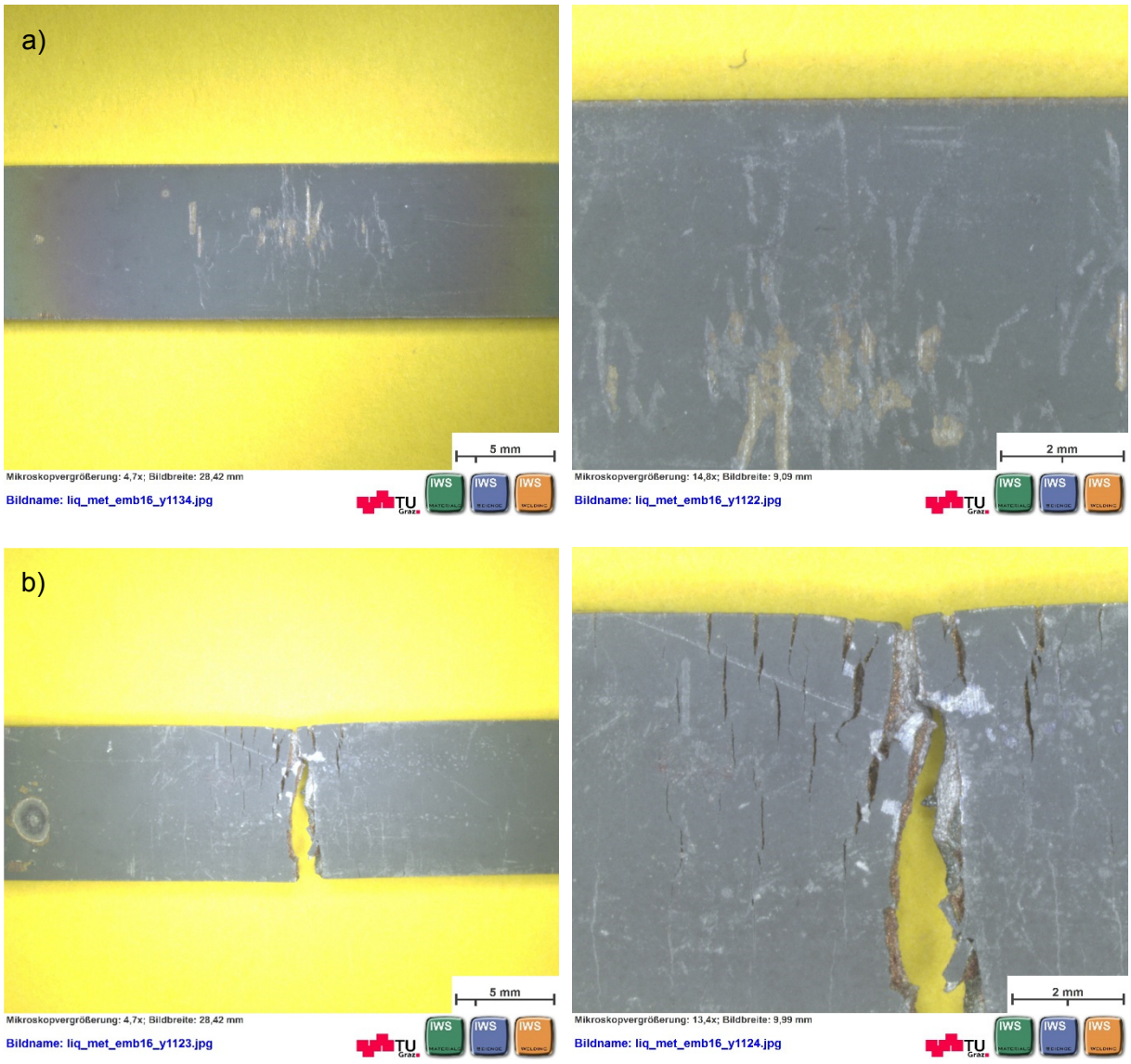

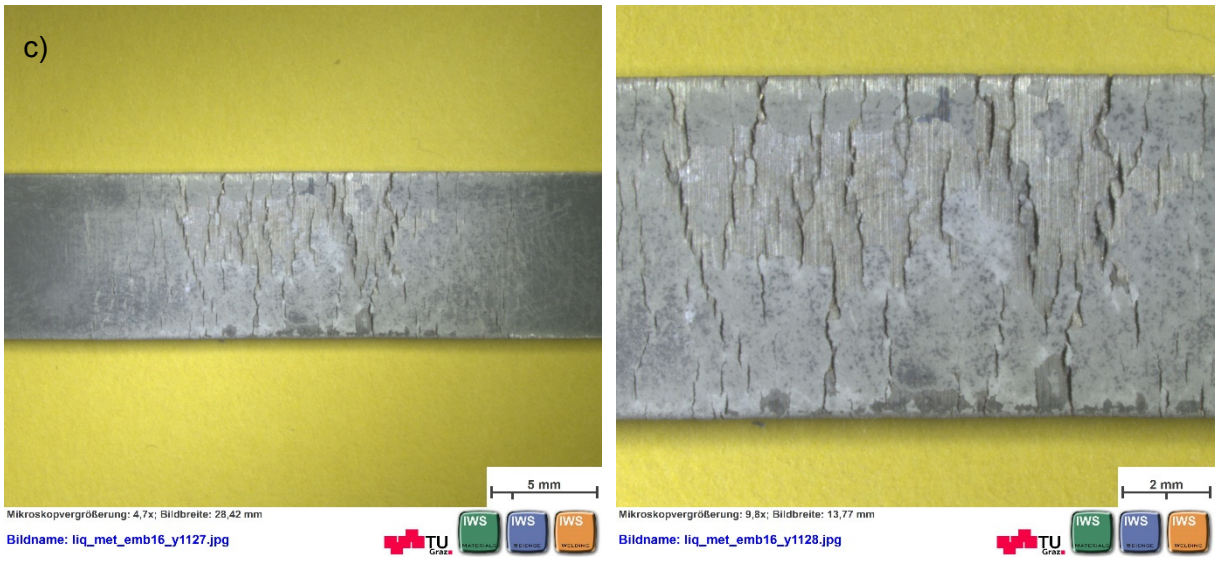

Figure 64: Stereo microscopy images of samples after RSW simulation test procedure at: a) 700°C b) 800°C c) 900°C

4.4.4 SEM investigation of zinc layer after testing

In order to get a better understanding of the mechanisms involved, some samples were investigated using EDX technique. In this section results of EG and ZP samples that underwent hot tensile tests are presented and discussed.

4.4.4.1 Zinc painted sample

Figure 65 shows the area of the coating and its surroundings of two zinc-painted samples.
The sample displayed in a) was tensile tested at 800°C without any holding time. The coating layer that before testing consisted of 96% zinc [58] declamped from the base material and is not visible on this picture. Before declamping, some zinc diffused into the base material during the thermo-mechanical test.
5 µm into the material the zinc content was found to be around 10–15 wt% with a peak of 15 wt% at 7 µm. Within this zone, the zinc amount led to a slightly decrease of iron when compared to the base material composition and a nearly complete depletion of nickel. Further into the material the zinc content dropped drastically and the original composition of the base material was found.

In b) the EDX analysis of a sample tested under the same conditions but with an applied holding time of 40 s is presented, which resulted in a nearly full recovery of mechanical properties. Here, the coating layer was still in place but showed clear signs of debonding with a distance around 2 µm between coating and base material. The coating consists mainly of zinc and possibly zinc oxide with some a peaks of nickel up to approx. 7 wt%. In the base material a

larger amount of zinc is present which gets smaller when going further into the material. Noteworthy is that the zinc-rich areas also contain a higher percentage of nickel. This leads to a depletion of nickel in the surrounding areas where a content as little as 3 wt% has been found.

Another noteworthy feature are the bright areas visible in the base material. Those have been investigated with additional EDX point scans and are further discussed below.

a) b)

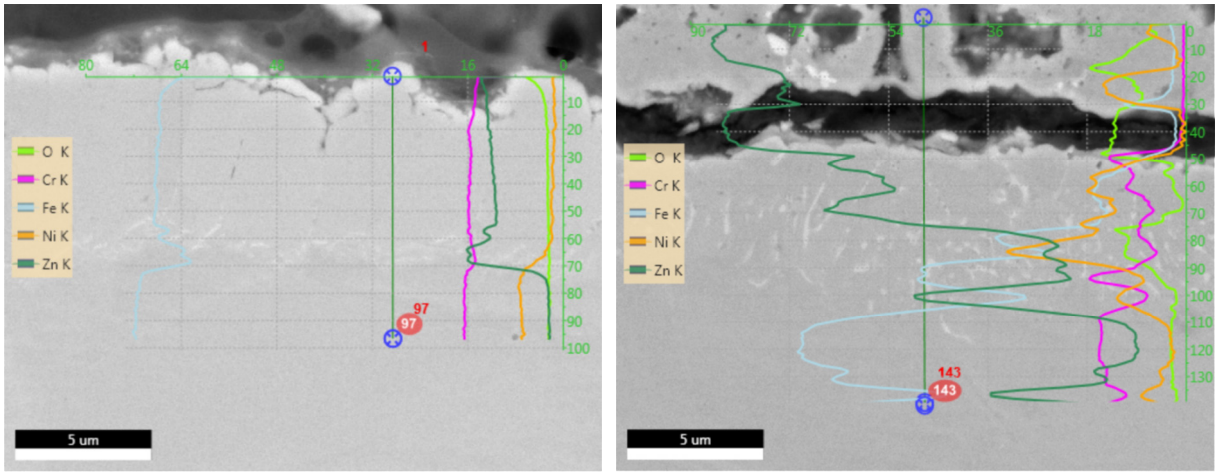

Figure 65: a) Coating layer of zinc painted sample tensile tested at 800°C with 1 mm/s strain rate b) Coating layer of zinc painted sample tensile tested at 800°C after 40 s pre-exposure time with 1mm/s strain rate

EDX spot scans were carried out in some specific areas. The highlighted area of Figure 66a) is displayed with higher magnification in b). There the locations of the spot scans are presented. The results of those spot scans are listed in Table 6.

The significant oxygen content found on all points is most likely based on an oxygen layer which developed after polishing and manipulated the results. Though, it can be stated that zinc is found in the whole area and especially in the brighter areas, such as EDX Punkt 2, the zinc and nickel content is significantly higher than in the rest.

a) b)

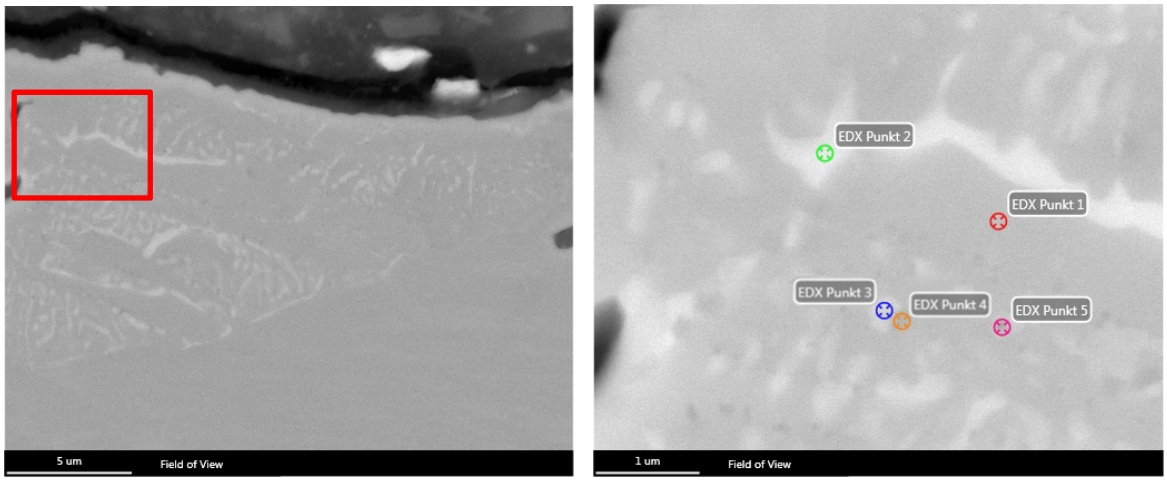

Figure 66: SEM image of zinc contaminated boarder area after tensile testing a zinc-painted sample at 800°C after 40 s holding time with 1 mm/s strain rate: a) overview b) higher magnification of area framed in a) showing the location of EDX point measurements

Table 6: Results of EDX point measurements of zinc painted sample after tensile testing at 800°C

	Weight%				
Element	EDX Punkt 1	EDX Punkt 2	EDX Punkt 3	EDX Punkt 4	EDX Punkt 5
OK	21.5	18.6	19.2	18.2	20.7
SiK	15.9	15.4	15.0	13.8	15.3
CrK	7.0	5.8	7.1	10.0	8.2
FeK	39.4	31.0	33.7	40.1	38.6
NiK	6.8	10.0	8.5	7.3	6.2
ZnK	9.6	19.2	16.5	10.6	11.0

4.4.4.2 Electro-galvanised sample

To evaluate a possible difference of the coating layer, an EDX analysis of a 10 µm electro-galvanised sample was carried out. A sample tensile tested at 800°C with 100 mm/s strain rate with a full recovery due to 20 s pre-exposure time is shown in Figure 67.

The line scan in a) exposes a high amount of iron within its first 10 µm - meaning the originally pure zinc layer. The shape of single element curves show some trends as the region of maximums and minimums of iron correlate to those of chromium and nickel shows a similar connection with zinc.

a) b)

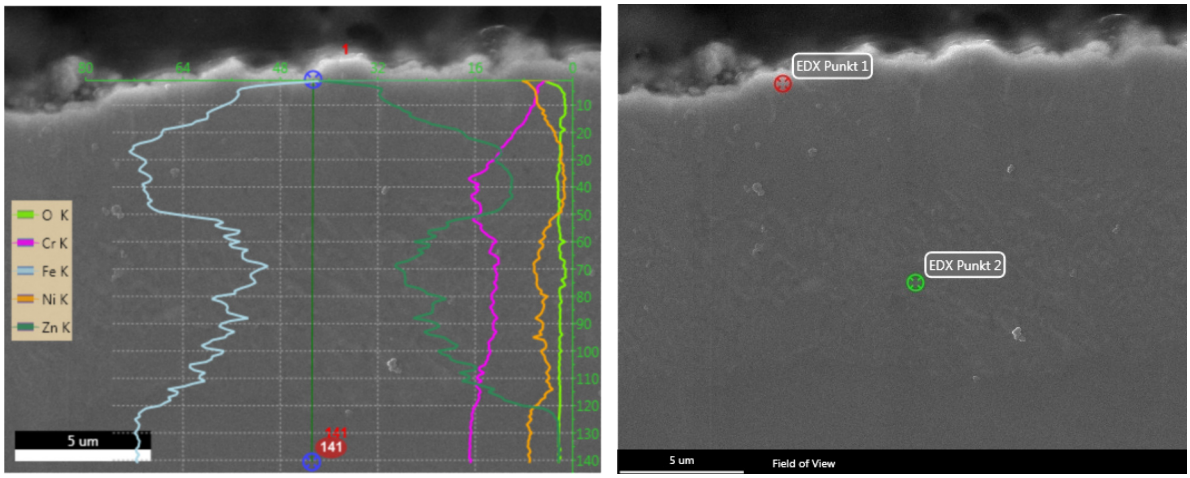

Figure 67: Coating layer of 10 µm electro-galvanised sample tensile tested at 800°C after 20 s holding time

The results of the EDX Spot scans of b) are listed in Table 7. The spot close to the edge of the sample (EDX Punkt 1) confirms a significantly high zinc content combined with mainly iron and nickel.

Around 9 µm into the sample which before testing was still the pure zinc layer, EDX Punkt 2 shows a remaining zinc content of around 24 wt%. This concludes that a significant amount of zinc has disappeared from its original location possibly due to vaporisation and diffusion.

Table 7: Results of spot scans of electro-galvanised sample tested at 800°C after 20 s holding time

	Weight%	
Element	EDX Punkt 1	EDX Punkt 2
OK	3.7	0.9
SiK	1.5	0.9
CrK	2.8	12.4
FeK	24.9	55.8
NiK	11.5	5.8
ZnK	55.6	24.3

4.4.4.3 Summary

Without pre-exposure time the ZP sample revealed a zone - fairly enriched by zinc in the fringe area, together with a depletion of nickel. Due to the tendency of zinc promoting ferritic structure

and the lack of nickel, which originally stabilised the austenite it is possible to find a change in structure to α-Fe(Zn) in this area.

After applying sufficient pre-exposure time at high temperature, zinc tends to concentrate close to the surface layer of the sample. This could be the reason for the high amount of short cracks in the fully recovered samples as discussed in chapter 4.4.1.4. Also a significant amount of zinc was found in some separated “islands” together with nickel and iron. This implies the formation of intermetallic compounds, also mentioned in the literature, leading to consumption of liquid zinc and thereby decreasing the available amount for α-Fe(Zn) formation.

Due to the lack of information about possible intermetallic compounds in the ternary system of Fe-Ni-Zn this has to be rated only as theory and needs further investigation. Additional EBSD measurements of the surface layer might help identifying α-Fe(Zn) grains.

4.4.5 SEM investigation of cracks

At first some EDX analysis of cracks with different depth are shown and later EBSD results are shown and discussed.

4.4.5.1 EDX analysis of cracks

In general two different types or stages of cracks were observed during this work. Firstly some opened cracks as shown in Figure 68. Secondly some closed cracks which were filled with a material that showed clear contrast to the base material when investigating with backscatter electron microscopy. This type is shown and discussed in the section of Figure 70

In Figure 68 a crack initiation site of an opened crack is shown after performing an EDX analysis. The surface layer shows a mixture of zinc, iron and nickel. It is clearly visible that zinc is present along the whole crack path. Interestingly, also a significant amount of nickel was found in the zinc enriched areas. Around those areas the resulting depletion of nickel is visible.

a) b)

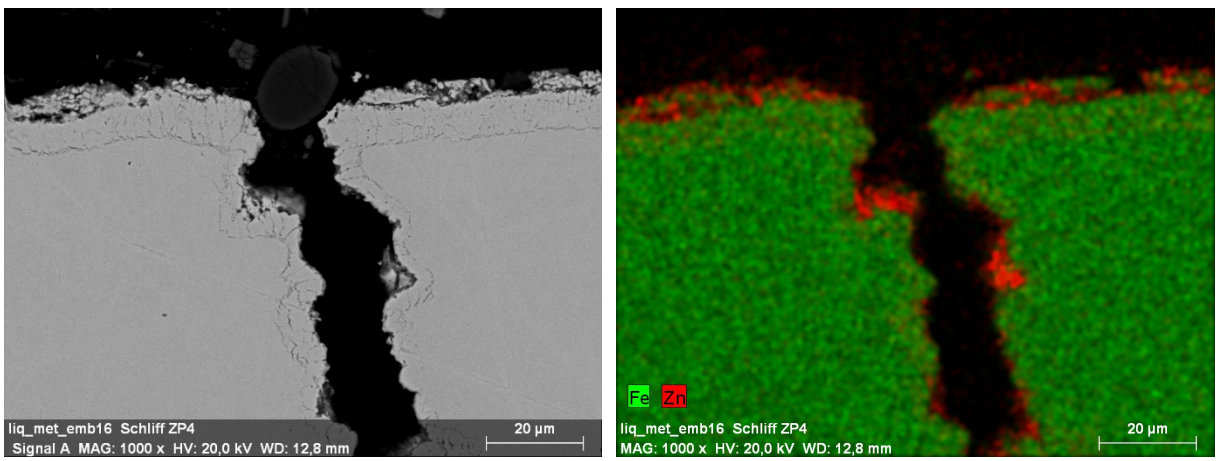

c) d)

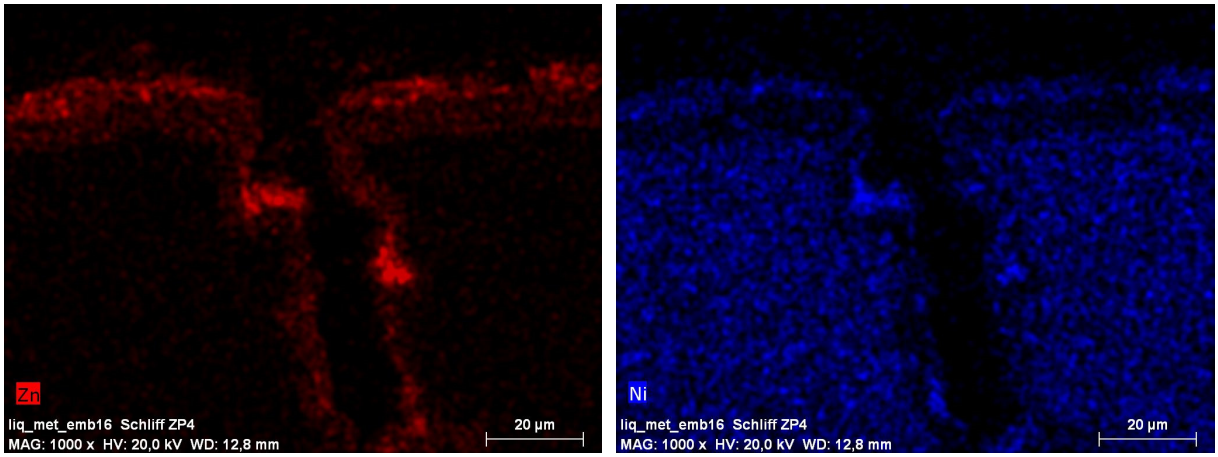

Figure 68: SEM image and EDX mapping of crack on zinc painted sample tested at 800°C: a) SEM image b) Fe-Zn distribution c) Zn distribution d) Ni distribution

The same crack shown in the images above went roughly 800 µm deep in the sample and therefore was picked for further EDX investigation to see how far the zinc penetration would go. At 3 different depths, line scans were performed and their results are shown in Figure 69. In a) an overview of the crack is given with the localisation of the performed line scans.

At a crack depth of around 30 µm, line scan b) shows a zinc layer around the crack and again an increased nickel content in this area. In the depth of approximately 380 µm, c), still zinc and nickel are found in the surrounding area. Finally in a depth of over 700 µm, d), no more zinc could be detected. Though, due to the small width of the crack of less than 2 µm this could be addressed to the not high enough resolution of the performed measurement.

a) b)

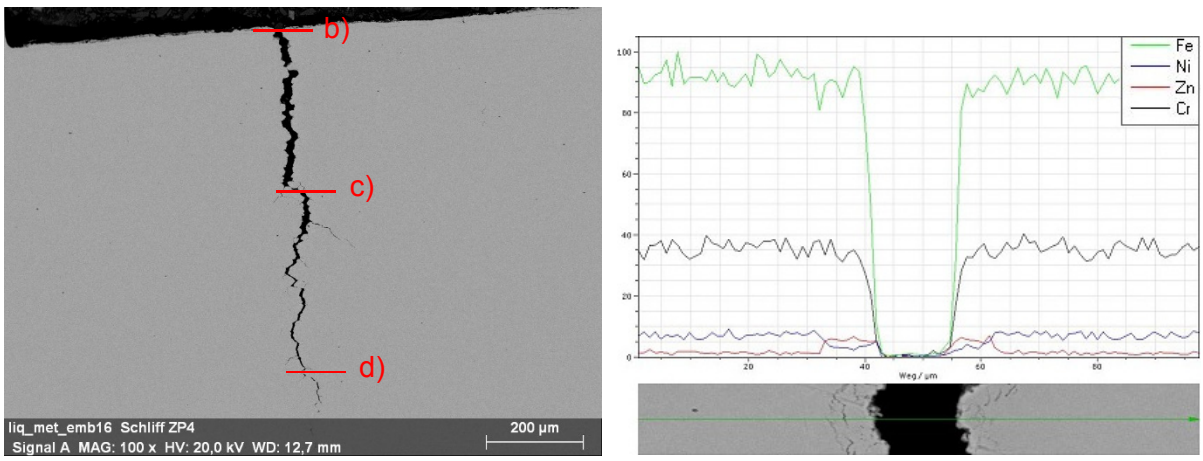

c) d)

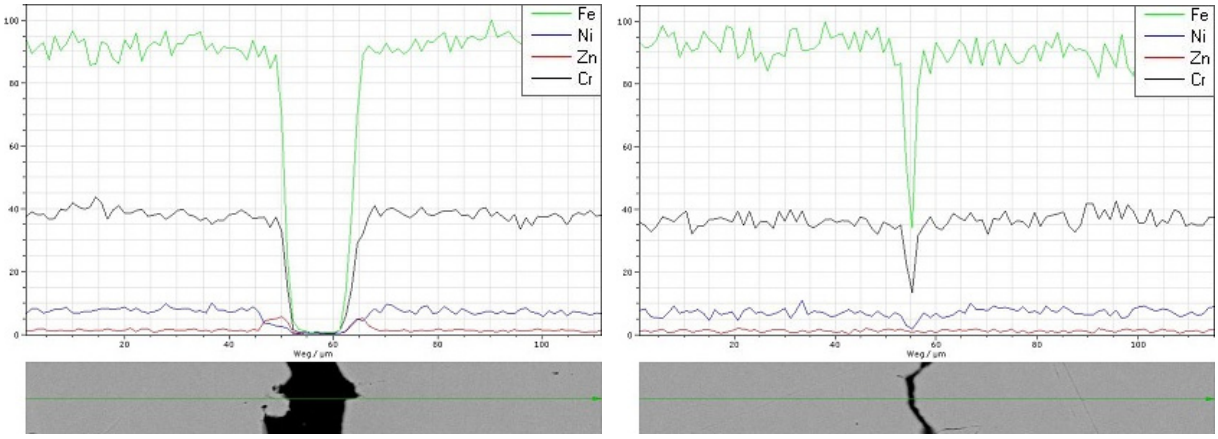

Figure 69: a) Image of deep crack in zinc painted sample showing the location of EDX line scans b) EDX line scan in 30 µm depth c) EDX line scan in 380 µm depth d) EDX line scan in 700 µm depth

Figure 70 shows a crack which is filled with a material different from the base material and therefore visible through different contrast using secondary electron (SE) microscopy. An EDX analysis of the filling material revealed a high content of zinc and nickel.

a) b)

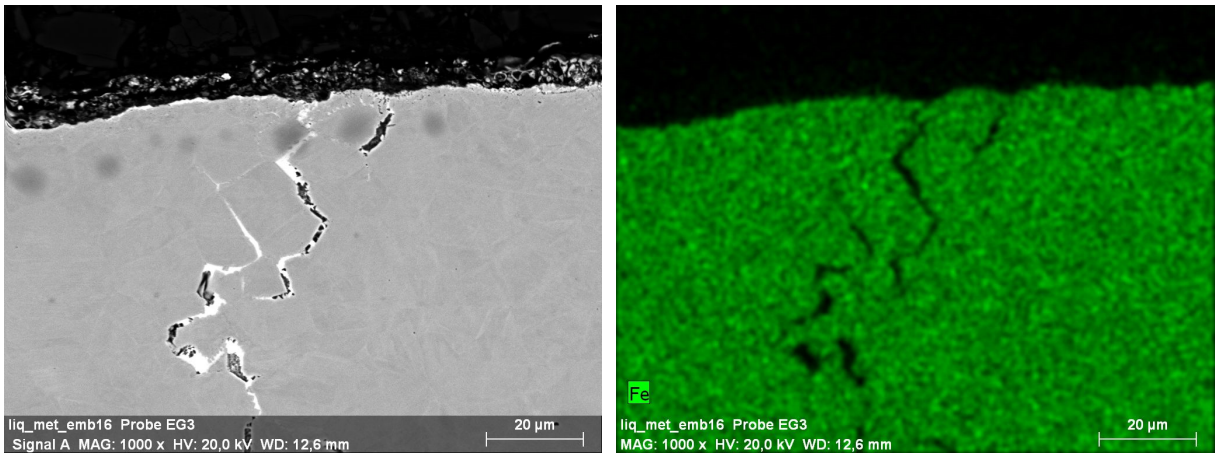

c) d)

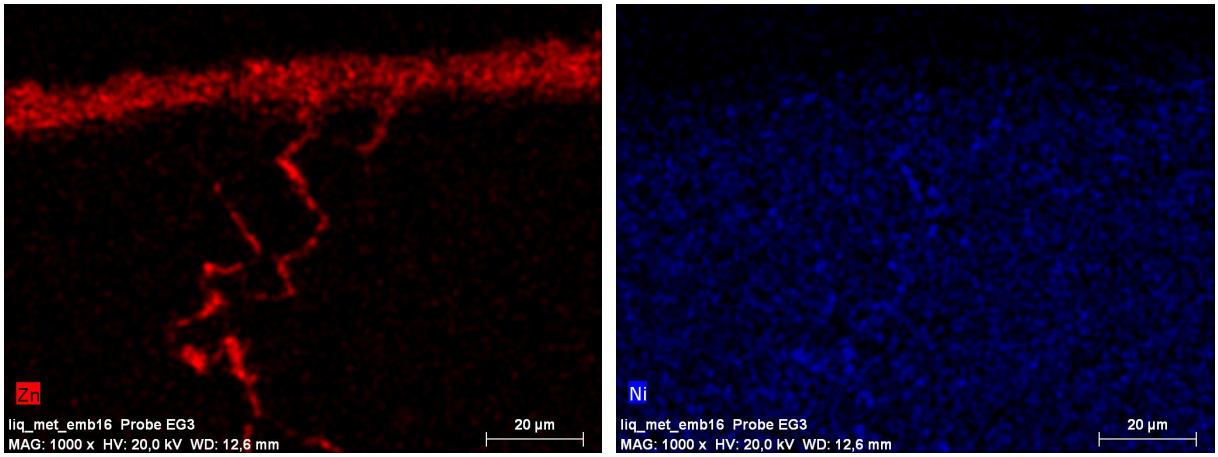

Figure 70: EDX mapping of 2.5 µm electro-galvanised sample tested at 800°C

Furthermore, a line scan with a higher resolution field emission gun scanning electron microscope (FEG-SEM) showed the evolution of composition through the crack (see Figure 71). Again, a high concentration of zinc together with nickel was found inside the crack with a depletion of nickel in the nearby area.

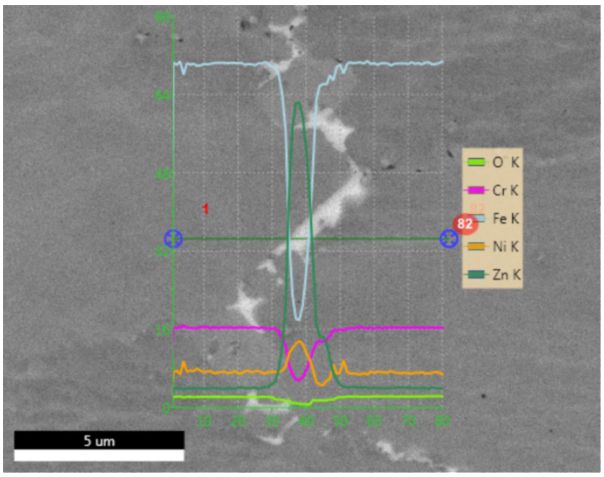

Figure 71: EDX line scan through crack within zinc-painted sample tested at 800°C

Finally some EDX spot scans showed the composition of the filling material. Figure 72 presents the location of those spot scans and Table 8 lists the results. For EDX Punkt 1 remarkable is the very high zinc content which comes close to the content of Γ (Fe_3Zn_{10}) (shown in chapter 2.1.4.1) and the significantly higher nickel content than in the base material. EDX Punkt 2 confirms those results but with lower zinc content exchanged by higher iron content.

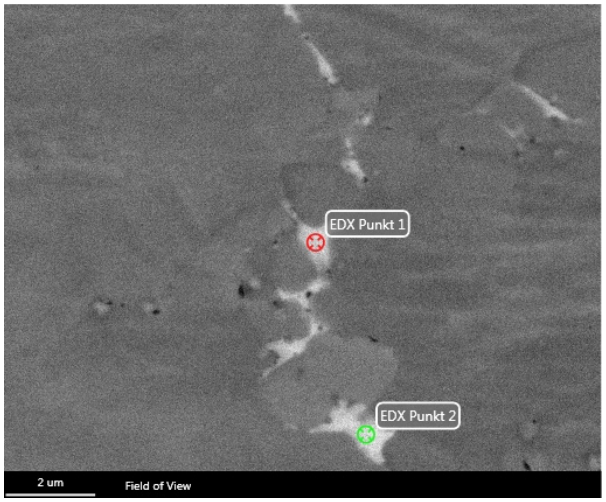

Figure 72: Filled crack of zinc-painted sample tested at 800°C showing the location of spot scans

Table 8 Chemical composition of spot scans of zinc painted sample tested at 800°C

	Weight%	
Element	EDX Punkt 1	EDX Punkt 2
CrK	3.88	6.95
FeK	14.44	28.09
NiK	14.81	12.77
ZnK	66.14	51.02

4.4.5.2 EBSD analysis of cracks

Figure 73 shows a SEM image of a deep crack found on an electro-galvanised sample tensile tested at 800°C with a strain rate of 100 mm/s. The highlighted box in a) marks the area picked for the EBSD investigation described below.

In b) a higher magnification of the area highlighted in Figure 74b) is shown. The arrows indicate small grains visible along the cracking path.

a) b)

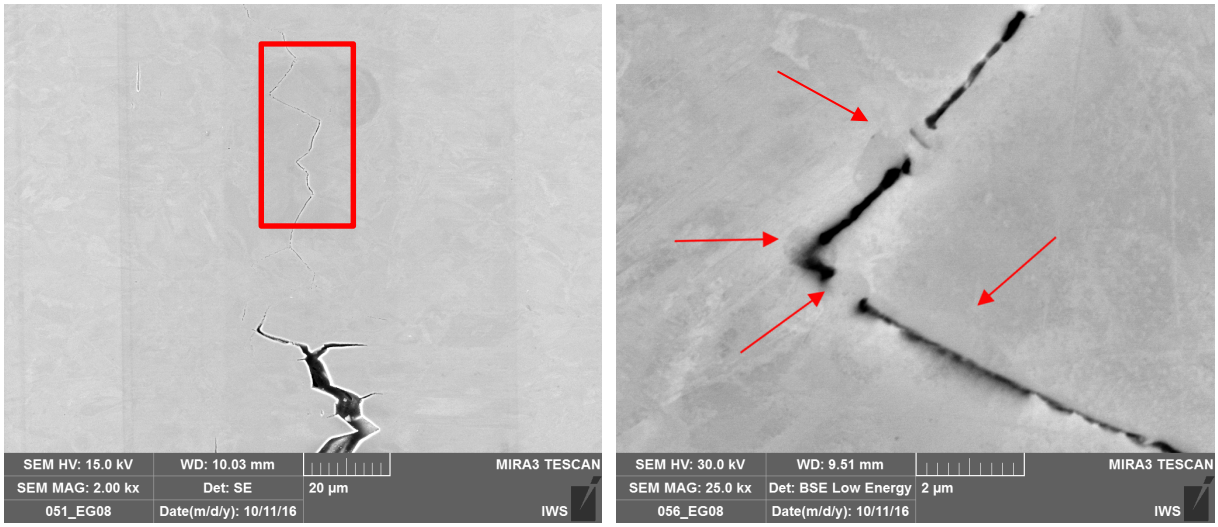

Figure 73: Deep crack of an electro-galvanised sample tensile tested at 800°C with a strain rate of 100 mm/s: a) SEM image highlighting the area picked for EBSD measurement b) higher magnification SEM image with arrows pointing at different grains along the cracking path

The EBSD maps displayed in Figure 74 shows the highlighted area of Figure 73a).
In a) austenitic and ferritic grains are shown whereas in b) only ferritic grains are visible. Due to the different orientation of the grains on either side of the crack it can be confirmed that cracks grow intergranular. Ferritic grains in the cracking zone possibly developed due to the depletion of nickel as austenite stabiliser in the vicinity of the crack which was displayed in several EDX analysis throughout this chapter. Zinc as a stabiliser of ferritic structure additionally supports this scenario.

a) b)

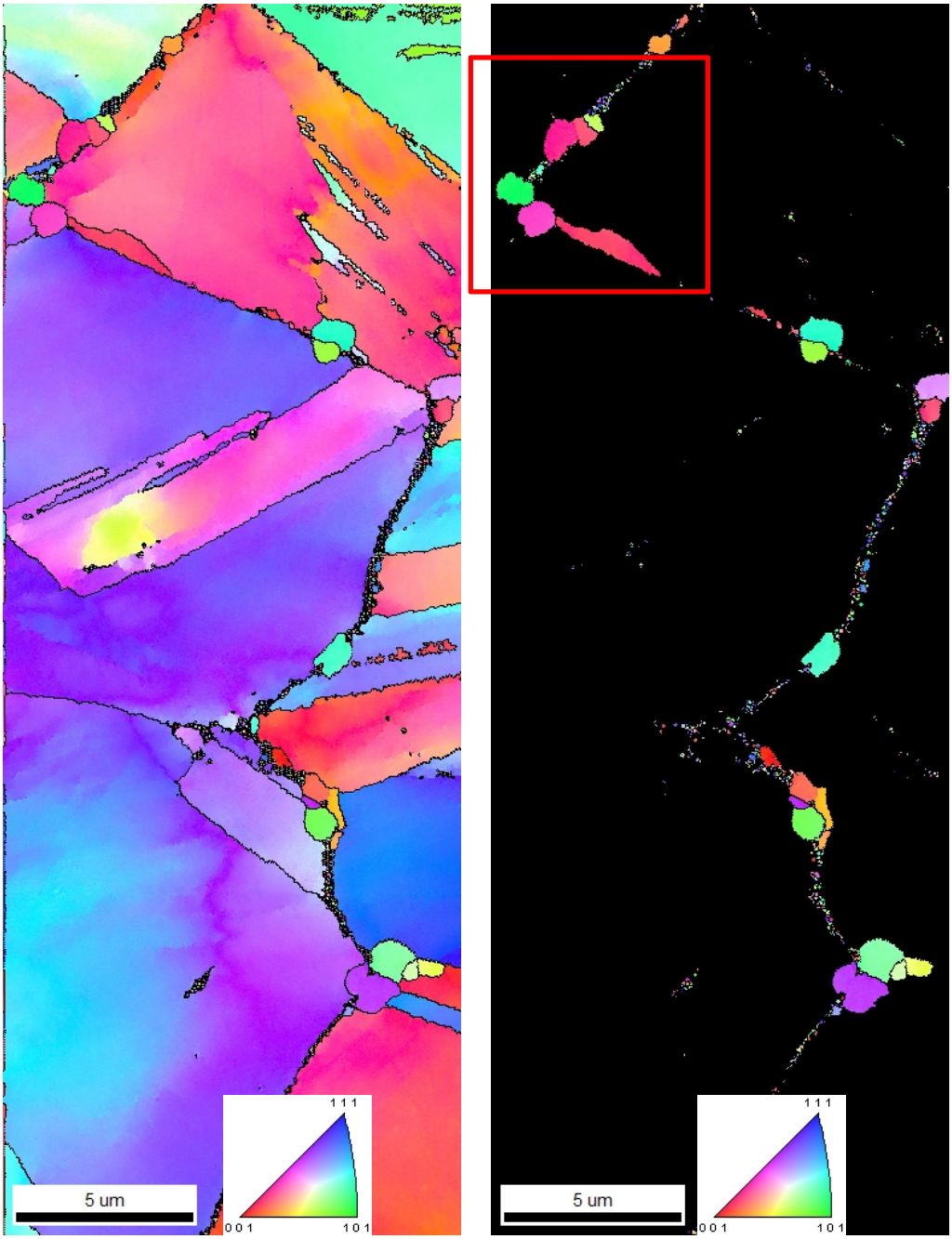

Figure 74: EBSD image of LME induced deep crack: a) inverse pole figure (IPF) coloured map showing all detected grains b) IPF coloured map showing only ferritic grains

4.4.6 Summary

EDX analysis of cracks showed the presence of zinc and nickel all along the cracking path, even in depths of several hundred micrometres. The zinc diffuses very fast from the zinc coating along grain boundaries. Nickel also diffuses into these zinc wetted grain boundaries leading to a depletion of nickel in the surrounding areas.
An EBSD investigation of a deep crack revealed that ferritic grains are present along the cracking path which can be explained by the enrichment of zinc (as ferrite promoter) and the depletion of nickel (being an austenite stabiliser) in the surrounding areas.
This phase change could lead to further crack propagation due to internal stresses and weaker strength of the ferritic phase.

Further investigations are necessary in order to deepen the understanding in this specific area.

5. Conclusions

The objective of this work was to investigate the influence of different parameters on the embrittlement of type 301 austenitic stainless by liquid zinc and to deepen the understanding of the involved mechanisms.

The sensitivity of the steel to LME was investigated using high temperature tensile tests performed on zinc coated samples with the help of a Gleeble® thermo-mechanical simulator. The influence of different parameters such as temperature, strain rate, time of contact between liquid and solid metal and others were analysed in various test series. Furthermore, interrupted hot tensile tests and additional tests to approximate resistance spot welding were performed.

The results have revealed that 301 steel is highly sensitive to liquid metal embrittlement by zinc when specific requirements are met. One requirement is a specific testing temperature in between an upper and a lower limit. The other one is an application of stress.

The temperature range where LME occurs is dependent on the strain rate but in all observed cases significantly higher than the melting point of zinc (419°C) and at maximum around 100°C higher than the boiling point of zinc (907°C). The lower limit not matching the melting point of the coating was observed also in previous studies [3] and could be explained by the testing conditions due to the sample not being immersed in liquid zinc but its contact due to melting of the coating layer. The upper limit being higher than the boiling point favours an explanation of vaporisation and thus a lack of liquid zinc.

Contradictory to results found in literature [3], [22] the influence of strain rate showed that a higher strain rate tends to narrow the temperature range where embrittlement is observed. Also the severity of embrittlement was decreased when testing at higher strain rate. Since only 2 different strain rates were tested and the higher one being 2 orders of magnitude higher than its reference this might be a result of the much shorter time to rupture implying a much shorter time for the embrittlement mechanism to take place.

Influence of pre-exposure time proved to drastically change the mechanical properties observed during tensile testing. A holding time of a few seconds proved to be enough for the mechanical properties to fully recover from the embrittlement process. This could be linked to the formation of FeNiZn intermetallic compounds of zinc and base material consuming all the available liquid zinc necessary for the embrittling of the material.

Furthermore, the impact of different coating techniques was studied which proved to have no noteworthy influence on the mechanical behaviour. The amount of liquid metal available influenced the necessary holding time at high temperature, required for a full recovery.

The questions behind the mechanism of the LME phenomenon could not be answered to full extent though but some conclusions could be drawn with the help of microscopy results. Further work focusing on the mechanism is necessary for finding the missing answers.

Outlook

Aiming for a better understanding of the cracking mechanism, additional thermo-mechanical tests, welding tests and microstructural investigations must be performed.

One way to go is to use faster heating rates together with shorter times at high temperature of the material and quench the sample in order to “freeze” the ongoing processes. With EDX and EBSD measurements on the coating layer of the sample further information about the diffusion mechanisms could be gathered.
Also a test series with the coating layer only on a small area in the centre of the samples so that only the homogeneous temperature zone is in contact with the embrittling liquid metal. This would lead to a more accurate determination of the temperature range and its severity of embrittlement.

Another path to follow is to carry out real welding tests to determine specifically for which parameters cracks appear. Together with the help of numerical simulation the stress and temperature situation within the samples during welding could be further investigated to make an even better link between the laboratory thermo-mechanical tests and the actual welding process.

Finally, the test cycle developed towards RSW simulation for thermo-mechanical simulation must be improved with higher heating rates in order to get closer to the welding process which might help on improving this process.

References

[1] (TU Graz/Aperam) C. Alvarez, “Study of the sensitivity of two austenitic stainless steel grades to Liquid Metal Embrittlement by Zinc,” 2015.

[2] B. Joseph, M. Picat, and F. Barbier, “Liquid metal embrittlement: A state-of-the-art appraisal,” *Eur. Phys. J. Appl. Phys.*, vol. 5, no. 1, pp. 19–31, Jan. 1999.

[3] C. Beal, “Mechanical behaviour of a new automotive high manganese TWIP steel in the presence of liquid zinc.” INSA de Lyon, 25-Mar-2011.

[4] W. H. Johnson, “On Some Remarkable Changes Produced in Iron and Steel by the Action of Hydrogen and Acids,” *Proc. R. Soc. London*, vol. 23, no. 156–163, pp. 168–179, Jan. 1874.

[5] L. Cho, H. Kang, C. Lee, and B. C. De Cooman, “Microstructure of liquid metal embrittlement cracks on Zn-coated 22MnB5 press-hardened steel,” *Scr. Mater.*, vol. 90–91, pp. 25–28, Nov. 2014.

[6] H. Kang, L. Cho, C. Lee, and B. C. de Cooman, “Zn Penetration in Liquid Metal Embrittled TWIP Steel,” *Metall. Mater. Trans. A Phys. Metall. Mater. Sci.*, vol. 47, no. 6, pp. 1–21, 2016.

[7] L. Mraz and J. Lesay, “Problems with reliability and safety of hot dip galvanized steel structures,” *Soldag. Inspeção*, vol. 14, no. 2, pp. 184–190, Jun. 2009.

[8] R. Ashiri, M. Shamanian, H. R. Salimijazi, M. A. Haque, C. W. Ji, and Y. Do Park, “Erratum: Supercritical area and critical nugget diameter for liquid metal embrittlement of Zn-coated twinning induced plasticity steels (Scripta Materialia (2015) 109 (6-10)),” *Scr. Mater.*, vol. 112, p. 156, 2016.

[9] C. Beal, X. Kleber, D. Fabregue, and M. Bouzekri, “Embrittlement of a High Manganese {TWIP} Steel in the Presence of Liquid Zinc,” *Mater. Sci. Forum*, vol. 706, pp. 2041–2046, 2012.

[10] D. R. Sigler, J. G. Schroth, W. Yang, X. Q. Gayden, C. Jiang, Y. Sang, and P. J. Morin, “Observations of Liquid Metal-Assisted Cracking in Resistance Spot Welds of Zinc-Coated Advanced High-Strength Steels,” *Sheet Met. Weld. Conf. XIII*, no. 6, pp. 1–17, 2008.

[11] R. BRUSCATO, “LIQUID-METAL EMBRITTLEMENT OF AUSTENITIC STAINLESS-STEEL WHEN WELDED TO GALVANIZED STEEL,” *Weld. J.*, vol. 71, no. 12, pp. 455–459, 1992.

[12] R. FRAPPIER, “Fragilisation des aciers par le zinc liquide à haute température et

conséquences," UNIVERSITÉ DE NANTES Ecole polytechnique de l'Université de Nantes, 2014.

[13] S. G. Keller and A. P. Gordon, "Experimental study of liquid metal embrittlement for the aluminum 7075–mercury couple," *Eng. Fract. Mech.*, vol. 84, pp. 146–160, 2012.

[14] X. Gong, P. Marmy, L. Qin, B. Verlinden, M. Wevers, and M. Seefeldt, "Temperature dependence of liquid metal embrittlement susceptibility of a modified 9Cr–1Mo steel under low cycle fatigue in lead–bismuth eutectic at 160–450 °C," *J. Nucl. Mater.*, vol. 468, pp. 289–298, Jan. 2016.

[15] S. P. Lynch, "18 – Failures of structures and components by metal-induced embrittlement," in *Stress Corrosion Cracking*, 2011, pp. 714–748.

[16] H.-S. Nam and D. J. Srolovitz, "Effect of material properties on liquid metal embrittlement in the Al–Ga system," *Acta Mater.*, vol. 57, no. 5, pp. 1546–1553, 2009.

[17] M. Rajagopalan, M. A. Bhatia, M. A. Tschopp, D. J. Srolovitz, and K. N. Solanki, "Atomic-scale analysis of liquid-gallium embrittlement of aluminum grain boundaries," *Acta Mater.*, vol. 73, pp. 312–325, 2014.

[18] E. Senel, J. C. Walmsley, S. Diplas, and K. Nisancioglu, "Liquid metal embrittlement of aluminium by segregation of trace element gallium," *Corros. Sci.*, vol. 85, pp. 167–173, 2014.

[19] M. . Malu and C. . Preece, "The role of solute additions to aluminum on its embrittlement by mercury," *Mater. Sci. Eng.*, vol. 11, no. 4, pp. 223–226, 1973.

[20] M. R. Chellali, L. Zheng, R. Schlesiger, B. Bakhti, A. Hamou, J. Janovec, and G. Schmitz, "Grain boundary segregation in binary nickel–bismuth alloy," *Acta Mater.*, vol. 103, pp. 754–760, 2016.

[21] N. Marié, K. Wolski, and M. Biscondi, "Intergranular penetration and embrittlement of solid nickel through bismuth vapour condensation at 700°C," *J. Nucl. Mater.*, vol. 296, no. 1, pp. 282–288, 2001.

[22] B. Joseph, F. Barbier, and M. Aucouturier, "Embrittlement of copper by liquid bismuth," *Scr. Mater.*, vol. 40, no. 8, pp. 893–897, 1999.

[23] V. N. Rozhanskii, N. V. Pertsov, E. D. Shchukin, and P. A. Rebinder, *No Title*, vol. 2. 1957.

[24] H. Glasbrenner, F. Gröschel, and T. Kirchner, "Tensile tests on MANET II steel in circulating Pb–Bi eutectic," *J. Nucl. Mater.*, vol. 318, pp. 333–338, May 2003.

[25] C. Beal, X. Kleber, D. Fabregue, and M. Bouzekri, "Liquid zinc embrittlement of twinning-

induced plasticity steel," *Scr. Mater.*, vol. 66, no. 12, pp. 1030–1033, Jun. 2012.

[26] P. J. L. Fernandes and D. R. H. Jones, "The effects of microstructure on crack initiation in liquid-metal environments," *Eng. Fail. Anal.*, vol. 4, no. 3, pp. 195–204, 1997.

[27] J. P. Hilditch, J. R. Hurley, P. Skeldon, and D. R. Tice, "The liquid metal embrittlement of iron and ferritic steels in sodium," *Corros. Sci.*, vol. 37, no. 3, pp. 445–454, 1995.

[28] A. Legris, G. Nicaise, J.-B. Vogt, and J. Foct, "Liquid metal embrittlement of the martensitic steel 91: influence of the chemical composition of the liquid metal.: Experiments and electronic structure calculations," *J. Nucl. Mater.*, vol. 301, no. 1, pp. 70–76, 2002.

[29] M. H. KAMDAR, "Liquid Metal Embrittlement," in *Treatise on Materials Science & Technology*, vol. 25, 1983, pp. 361–459.

[30] T. Sample and H. Kolbe, "Liquid metal embrittlement (LME) susceptibility of the 8–9% Cr martensitic steels F82H-mod., OPTIFER IVb and their simulated welded structures in liquid Pb–17Li," *J. Nucl. Mater.*, vol. 283, pp. 1336–1340, 2000.

[31] C. Beal, X. Kleber, D. Fabregue, and M. Bouzekri, "Embrittlement of a zinc coated high manganese TWIP steel," *Mater. Sci. Eng. A*, vol. 543, pp. 76–83, 2012.

[32] C. W. Lee, D. W. Fan, I. R. Sohn, S. J. Lee, and B. C. De Cooman, "Liquid-metal-induced embrittlement of Zn-coated hot stamping steel," *Metall. Mater. Trans. A Phys. Metall. Mater. Sci.*, vol. 43, no. 13, pp. 5122–5127, 2012.

[33] M. Ichinose, "No Title," *Trans. Jpn. Inst. Met.*, vol. 7, p. 57, 1966.

[34] R. Saluja and D. K. . Moeed, "Emphasis of Embrittlement Characteristics in 304L and 316L Austenitic Stainless Steel," *IOSR J. Mech. Civ. Eng.*, vol. 11, no. 6, pp. 04–10, 2014.

[35] J. Van den Bosch, R. W. Bosch, D. Sapundjiev, and A. Almazouzi, "Liquid metal embrittlement susceptibility of ferritic-martensitic steel in liquid lead alloys," *J. Nucl. Mater.*, vol. 376, no. 3, pp. 322–329, 2008.

[36] X. Gong, P. Marmy, L. Qin, B. Verlinden, M. Wevers, and M. Seefeldt, "Effect of liquid metal embrittlement on low cycle fatigue properties and fatigue crack propagation behavior of a modified 9Cr–1Mo ferritic–martensitic steel in an oxygen-controlled lead–bismuth eutectic environment at 350°C," *Mater. Sci. Eng. A*, vol. 618, pp. 406–415, 2014.

[37] S. Hémery, T. Auger, J. L. Courouau, and F. Balbaud-Célérier, "Liquid metal embrittlement of an austenitic stainless steel in liquid sodium," *Corros. Sci.*, vol. 83, pp. 1–5, Jun. 2014.

[38] K. Pańcikiewicz, L. Tuz, and A. Zielińska-Lipiec, “Zinc contamination cracking in stainless steel after welding,” *Eng. Fail. Anal.*, vol. 39, pp. 149–154, 2014.

[39] M. Vural and A. Akkus, “On the resistance spot weldability of galvanized interstitial free steel sheets with austenitic stainless steel sheets,” *J. Mater. Process. Technol.*, vol. 153–154, pp. 1–6, Nov. 2004.

[40] S. Kodama, Y. Ishida, K. Asai, M. Mizumoto, T. Namekata, and H. Nagasaki, “Development of Stainless Steel Welding Wire for Galvanized Steel Sheets,” *Weld. World*, vol. 54, no. 1–2, pp. R42–R48, Jan. 2013.

[41] O. K. von Goldbeck, *IRON—Binary Phase Diagrams*. Berlin, Heidelberg: Springer Berlin Heidelberg, 1982.

[42] V. Raghavan, “Fe-Zn (Iron-Zinc),” *J. Phase Equilibria*, vol. 24, no. 6, pp. 544–545, Dec. 2003.

[43] A. Luithle and M. Pohl, “On the influence of cold deformation on liquid metal embrittlement of a steel in a liquid zinc bath,” *Mater. Corros.*, vol. 66, no. 12, pp. 1491–1497, 2015.

[44] C. W. Lee, W. S. Choi, Y. R. Cho, and B. C. De Cooman, “Microstructure evolution of a 55wt.% Al–Zn coating on press hardening steel during rapid heating,” *Surf. Coatings Technol.*, vol. 281, pp. 35–43, 2015.

[45] C. W. Lee, W. S. Choi, L. Cho, Y. R. Cho, and B. C. De Cooman, “Liquid-Metal-Induced Embrittlement Related Microcrack Propagation on Zn-coated Press Hardening Steel,” *ISIJ Int.*, vol. 55, no. 1, pp. 264–271, 2015.

[46] “Werkstoffkunde.pdf.” .

[47] D. Kopeliovich, “Effect of alloying elements on steel properties [SubsTech],” *SubsTech*. .

[48] P. Marshall, *Austenitic stainless steels : microstructure and mechanical properties*. Elsevier Applied Science, 1984.

[49] M. L. Wayman, “Metallography of Archaeological Alloys,” *ASM Handb. V9*, vol. 9, pp. 468–478, 2004.

[50] M. Steels, “Metallography and Microstructures of Stainless steels Maraging steels,” *ASM Handb. V9*, vol. 9, no. c, pp. 1–27, 2004.

[51] C. B. S. Cramer S.D., “Corrosion of Wrought Stainless Steels,” in *ASM Handbook - Corrosion : Materials*, vol. 13B, 2005, pp. 54–77.

[52] “Austenitic stainless steel 200 and 300 series | Stainless steel types | More stainless |

Products & properties | Global | Outokumpu.” [Online]. Available: http://www.outokumpu.com/en/products-properties/more-stainless/stainless-steel-types/austenitic/pages/default.aspx.

[53] “The effects of alloying elements | More stainless | Products & properties | Global | Outokumpu,” *Outokumpu*. [Online]. Available: http://www.outokumpu.com/en/products-properties/more-stainless/the-effects-of-alloying-elements/Pages/default.aspx. [Accessed: 12-Oct-2016].

[54] “Chrome Carbides in Austenitic Steel Immagine121.png (PNG-Grafik, 345 × 273 Pixel).” [Online]. Available: http://www.nitty-gritty.it/wp-content/uploads/2016/05/Immagine121.png.

[55] “APERAM 301 M_ ENG.pdf.” [Online]. Available: http://www.aperam.com/uploads/stainlesseurope/TechnicalDataSheet/FT aust%25C3%25A9nitiques/Anglais/APERAM 301 M_ ENG.pdf. [Accessed: 02-Mar-2016].

[56] “Zinc Coatings and Applications Chart | American Galvanizers Association.” [Online]. Available: http://www.galvanizeit.org/knowledgebase/article/zinc-coatings-and-applications-chart.

[57] “Zinc_Coatings.jpg (JPEG-Grafik, 500 × 273 Pixel),” 2016. [Online]. Available: http://www.galvanizeit.org/uploads/default/_500/Zinc_Coatings.jpg.

[58] “What is ZINGA? | Zingametall,” 2016. [Online]. Available: http://www.zinga.eu/what-is-zinga/.

[59] “Electroplating of a metal (Me) with copper in a copper sulfate bath.” [Online]. Available: https://en.wikipedia.org/wiki/Electroplating. [Accessed: 18-Nov-2016].

[60] M. . Lewis and B. Hattersley, “Precipitation of M23C6 in austenitic steels,” *Acta Metall.*, vol. 13, no. 11, pp. 1159–1168, 1965.